506946

CCMS-91-19
VPI-E-91-19

VIRGINIA TECH

CENTER FOR COMPOSITE MATERIALS AND STRUCTURES

LANGLEY
GRANT
IN-24-CR

53186

(NASA-CR-189485) COMPRESSION FAILURE OF ANGLE-PLY LAMINATES Interim Report No. 87 (Virginia Polytechnic Inst. and State Univ.) 174 p CSCL 11D
N92-13285
Unclas
G3/24 0053186

Compression Failure of Angle-Ply Laminates

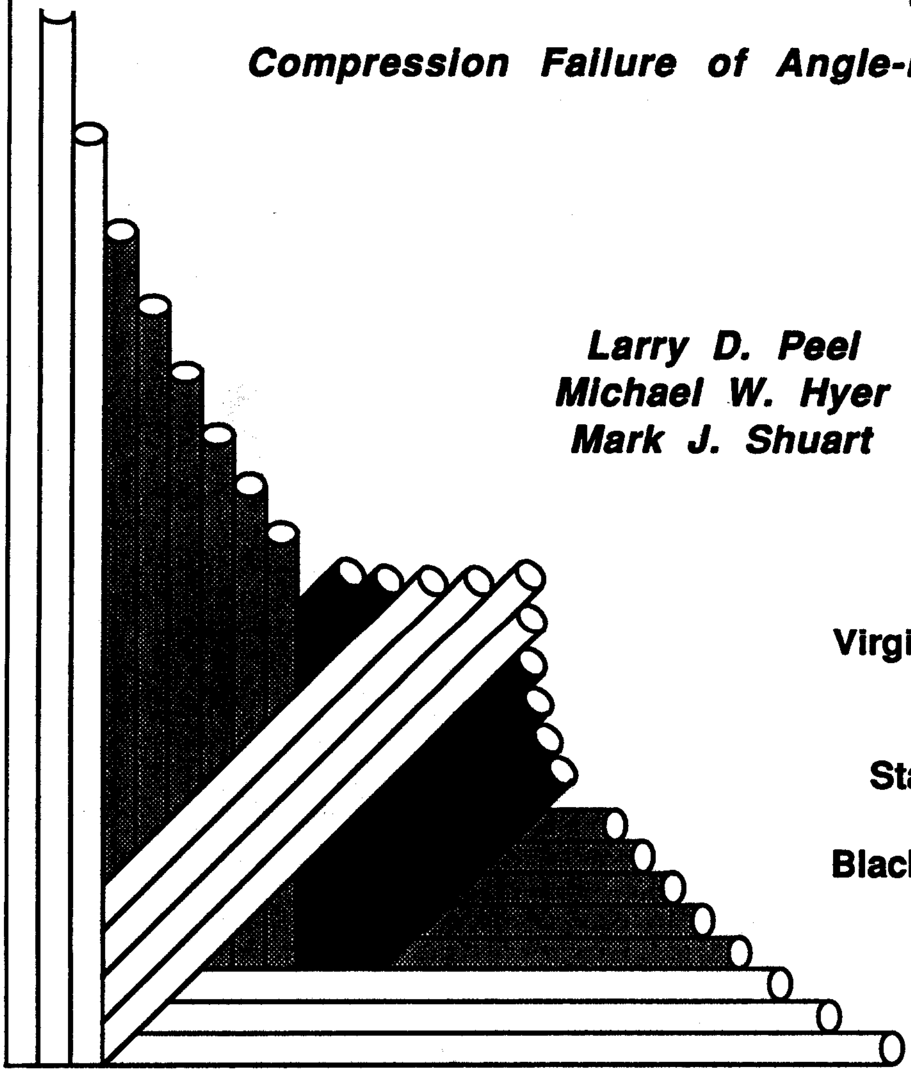

Larry D. Peel
Michael W. Hyer
Mark J. Shuart

Virginia Polytechnic
Institute
and
State University

Blacksburg, Virginia
24061

September 1991

College of Engineering
Virginia Polytechnic Institute and State University
Blacksburg, Virginia 24061

September 1991

VPI-E-91-19
CCMS-91-19

Compression Failure of Angle-Ply Laminates

Larry D. Peel[1]
Michael W. Hyer[2]
Mark J. Shuart[3]

Department of Engineering Science and Mechanics

NASA Grant NAG-1-343

Interim Report 87

The NASA-Virginia Tech Composites Program

Prepared for: Aircraft Structures Branch
National Aeronautics and Space Administration
Langley Research Center
Hampton, Virginia 23665-5225

---

[1] Graduate Student, Department of Engineering Science and Mechanics, Virginia Polytechnic Institute and State University

[2] Professor, Department of Engineering Science and Mechanics, Virginia Polytechnic Institute and State University

[3] Assistant Branch Head, Aircraft Structures Branch, NASA Langley Research Center

TABLE OF CONTENTS

LIST OF FIGURES

LIST OF TABLES

1.0 INTRODUCTION, LITERATURE REVIEW, AND OBJECTIVES

1.1 Introduction

The biggest aerospace structures revolution of the past 30 years has been in the area of composites materials. Composite materials in their most general interpretation consist of a reinforcing phase in a second, usually softer phase. For the present work, composites will be assumed to consist of a continuous fiber reinforcement embedded in a polymeric matrix. Fiber-reinforced polymer composites have gained great popularity because of their high specific strength and the ability to manufacture composite structures with curved surfaces as easily as structures with flat surfaces.

One of the major concerns when designing composites structures is the prediction of compressive strength. The compressive strength of a composite component includes the structural buckling strength, post-buckling strength, and also the actual compressive strength of the material from which the component is made. The present work will primarily discuss the compressive failure modes and mechanisms of the material, specifically angle-ply laminates.

Laminated composites consist of multiple layers, or plies, of fibers. In each layer the fibers are embedded in a matrix. The matrix is usually assumed to be isotropic, although some anisotropy can be inferred from data. The fibers are usually assumed to be orthotropic in nature, however, that may not be true if they are not circular, or do not have constant cross-sectional composition. Also, although a perfect laminate can be hypothesized and subsequently analyzed, it is difficult to actually find a perfect laminate in practice. There are always some misaligned or broken fibers, and some variation in the matrix. Between fiber layers there may be small matrix-rich zones. These matrix-rich zones may not be of uniform thickness, nor would they occur the same way in all layers. In this context then, a composite laminate can be considered to consist of a number of layers of slightly misaligned fibers, the layers not necessarily being a uniform distance apart, joined together by thin layers of matrix. The lack of uniformity within the laminate is thought to control compressive strength, and to contribute to the difficulty in analyzing composites for their compressive response. This is a particularly vexing concern because it is impossible to design composite structures without accurately knowing the compressive strength of the material. Hence, the understanding of compressive failure of composite laminates is of major concern as regards to the future use of composite materials.

In the following section some of the more recent research on the subject of compression of laminates will be discussed, including work dealing with analysis, modes and mechanisms of failure, and compression testing. By no means will this review be exhaustive. Rather, it is intended to provide a flavor of past efforts. The section following that will present the scope and objectives of the present work. Some of the overlying concerns, assumptions, and decisions involving this work will be discussed. This chapter ends with a preview of the chapters which follow.

1.2 Literature Review

Because laminate compressive failure is a major concern, researchers have studied it quite intensely for the last 20 years. Reviewing some of the important papers: Dow and Grundfest[1] suggested that compressive failure might be the result of fibers buckling within the matrix. Rosen[2] developed a model for orthotropic laminates that concentrated on ply-level instability and predicted compressive strength due to fiber buckling. The values predicted by Rosen, however, are considerably higher than experimental values. Greszczuk[3,4] investigated the role that the constituents of a laminate have in determining compressive strength. Evans and Adler[5], Maewal[6], and Hahn and Williams[7] examined fiber kinking mechanisms for compression-loaded laminates. Suarez, Whiteside and Hadcock[8], in an excellent report, discuss outer-ply instability for compression-loaded anisotropic laminates, initial waviness of outer plies, and shearing failure mechanisms of angle-ply laminates. In other work, Hawthorne and Teghtsoonian[9] suggest that fiber compression failure changes from a shear to a microbuckling or kinking mode with increasing fiber anisotropy. Piggot[10] postulates that a number of mechanisms may cause laminate compressive failure. The operative failure mechanism in a particular situation is the one that gives the lowest failure stress. Piggot also gave suggestions on how to obtain good laminate compressive modulus and strength. Sinclair and Chamis[11] suggest that the failure mode for unidirectional AS/PR288 graphite-epoxy specimens is delamination controlled by interlaminar shear, and the failure modes for unidirectional T300/5208 specimens are fiber compression, flexure or delamination, and Euler buckling for low, medium, and high strength specimens, respectively. Yeh and Teply[12] suggest that predicting compressive strength based on fiber microbuckling is suitable for composites with a very high axial shear modulus, but for composites with fibers that have very low axial shear modulus the compressive behavior is dominated by local shear failure. They also suggest that for more accurate results the nonlinear shear deformation of the matrix should be considered, and that local fiber misalignment plays a very important role in determining compressive strength. Gurdal and Haftka[13] assume laminate compressive failure is due to a strength failure rather than the microbuckling instability of fibers. In their theory high bending stresses are developed at the restrained ends of a misaligned fiber due to side loads. As a result, these high stresses cause fiber breakage. Reifsnider and Mirzadeh[14], in their tests of Celion 3000/PMR15 woven composite panels, identify the mode of compressive failure as fiber kinking, with strength affected by matrix cracking, weave geometry, and specimen surface. Gurdal and Starbuck[15] suggest that some problems in compressive failure experiments may be resolved by a better compression test fixture. They developed and used an end-loaded fixture which is claimed to allow for longer test specimens, ease specimen alignment problems, and reduce stress concentrations. Odom and Adams[16] postulate that the occurrence of a particular failure mode may depend heavily on test fixture geometry, type of loading, tabbing, etc. Highsmith, Davis, and Helms[17] conducted an analysis of T650-42/Radel C. They measured wavy fibers with wavelengths between 0.075 to 0.090 in. and amplitudes between 0.00207 to 0.0037 in. A single imperfection ratio was used to describe the amount of waviness in a laminate. Their model included nonlinear matrix behavior but appeared to over-predict compressive strength. Kumar and Helminiak[18] state that for higher strength carbon and glass fibers, their full compressive strength is not being realized and that factors such as matrix, interface, fiber modulus, and fiber geometry affect laminate strength. In the case of lower compressive strength carbon fibers and all polymeric fibers, the composite compressive strength is limited by the fibers themselves. Schoeppner and Sierakowski[19] reviewed about 17 different compression test fixtures and methods and found that some gave widely varying results. However, Adams and Odom[20] conducted a comparison of three different shear-loaded compression test fixtures and found that if proper procedures were followed, equivalent results for strength and modulus could be obtained.

Shuart[21,22] conducted an analytical and experimental investigation of angle-ply composite laminates, the analysis focusing on the ply level. A generalized theory was derived that would predict a laminate's compressive strength and failure mode. A composite specimen was modeled as an array of parallel fiber-reinforced plates connected through elastic foundations. Compression loads were applied through end shortening of the array of plates. Critical buckling loads and wavelengths were determined from a linear short-wavelength buckling analysis. A geometrically nonlinear analysis was then developed which used the critical short-wavelength to model initial out-of-plane waviness of the fiber-reinforced plates. An out-of-plane waviness amplitude of one-half ply thickness was assumed. Failure modes included fiber scissoring, interlaminar shearing, matrix compression, and inplane matrix shearing. A short-block compression test fixture was used to test $[(\pm\theta)/(\mp\theta)]_{6s}$ angle-ply specimens made of AS4/3502 graphite-epoxy. Shuart tested 28 specimens with θ ranging from 0° to 90°. The theory showed good correlation with test results for θ less than 45° and excellent correlation for θ greater than 45°. Shuart discussed the need for additional experimental verification of the theory and exploration of the effects of the compression test method on compressive strength and failure modes.

In summary: Compression failure analyses have primarily concentrated on short-wavelength or micro-buckling theories for unidirectional laminates, and on failures due to both inplane and interlaminar shear. Before Shuart's study short-wavelength buckling for multidirectional laminates had received little attention. The importance of including initial imperfections and quantifying them has been recognized. Also, it has been recognized that compression test methods and fixturing may play a significant role in compressive failure mechanisms.

1.3 Objectives and Scope of Work

Since angle-ply laminates constitute an important and practical class of laminates, the present work will focus on the compression failure of angle-ply laminates. The primary objectives of this work were to:

1. Study through experiments and through analysis the compression failure of angle-ply IM7/8551-7a laminates;
2. Enlarge upon the linear and nonlinear theories of Shuart[21,22] to develop more comprehensive methods for predicting compressive strength;
3. Compare the results obtained for IM7/8551-7a with the results for AS4/3502 as recorded in reference 22.

The first and third objectives were aimed at contributing to the overall understanding of compression failure mechanisms, and also adding to the data-base on a contemporary toughened-matrix material. In particular, 42 IM7/8551-7a specimens with a lay-up of $[(\pm\theta)/(\mp\theta)]_{6s}$, $0° \leq \theta \leq 90°$, were tested to failure using a short-block compression fixture similar to that used in reference 22. Recorded were the failure stresses, the failure strains, the elastic properties, and the failure modes. These results were studied within their own context, and also in comparison with Shuart's work with AS4/3502. Comparisons between AS4/3502 and IM7/8551-7a are of value in understanding the modes and mechanisms of failure, and how they depend on material system.

The second objective was aimed at extending the interpretation and capabilities of the analytical work. In particular, the influence of imperfection wavelengths not associated with the short-wavelength buckling modes of the layers, as well as those that are associated with short-wavelength buckling of layers, were studied. An example of layer waviness not associated with short-wavelength buckling of layers is that associated with manufacturing processes. Additional failure modes such as fiber compression and inplane transverse tension were also considered. The nonlinear theory and the associated computer program were modified to allow the imperfection amplitude to vary on a layer by layer basis, rather than every layer having the same imperfection amplitude. Other performance enhancements to the computer programs associated with the previous work were also pursued.

The next chapter begins by reviewing and discussing several types of compression test fixtures. This discussion will possibly provide insight as to why discrepancies exist between test results from various test fixtures. After that discussion the results from testing the angle-ply IM7/8551-7a specimens will be presented. Details of the failure modes as a function of off-axis angle θ, elastic properties, failure stresses, failure strains, and other information relevant to failure will be presented. A comparison between the observed failure strengths and the prediction of classical lamination theory coupled with the maximum stress failure criterion then follows. It is shown that there are large discrepancies, particularly at low off-axis angles, between the classical predictions and the experimental results. Several reasons for the discrepancies are postulated, with layer waviness being considered as having the most effect. As the work of references 21 and 22 resulted in the implementation of a nonlinear theory that considered the influence of wavy layers, that theory is chosen as a basis for explaining the discrepancies between observed results and classical theory. As implied above, that theory is used as it was in reference 21 and 22, but the theory is also enlarged upon and re-interpreted in the present study.

Chapter 3 provides an overview of the theory underlying the linear and nonlinear analyses. Chapter 4 explains the modifications and additions to the theory and computer programs, and discusses the post-processors written to extract more information from the analytical results.

Chapter 5 is a rather lengthy chapter in that the modified analysis is used to comprehensively explore the influence of layer waviness on compressive strength. Critical half-wavelengths, in the sense of short-wavelength ply-buckling and half-wavelengths associated with manufacturing anomalies, are considered as wave lengths, along with a variety of wave amplitudes. The maximum strength criterion, in conjunction with the nonlinear theory, is used to predict compressive strength as a function of off-axis angle, wave length, and wave amplitude. In addition to examining the inplane stresses in the context of that criterion, interlaminar shear strains induced because of waviness are compared with allowable values. Hence the modes of failure observed in the experiments can be compared with the modes of failure predicted by the nonlinear theory. To add another dimension, predictions and experimental results for AS4/3502 laminates are discussed in parallel with the results of IM7/8551-7a laminates. Differences and similarities in the predictions due to the material systems are examined. Finally, in chapter 5 the influence of just some of the layers being wavy is examined. This provides an informative extension to the preceding work. Chapter 5 ends with a summary which describes the influence of waviness in terms of strength retention, that is, compressive strengths predicted by the nonlinear theory compared to strengths predicted by classical lamination theory.

Chapter 6 summarizes the work, and presents conclusions and recommendations for future work.

2.0 TESTING OF IM7/8551-7a SPECIMENS

2.1 Discussion of Compression Test Methods and Fixtures

Three basic types of compression-test fixtures are currently popular. As noted in the previous literature review, there can be large differences between experimental results when testing similar specimens in each of the three types of fixtures. For completeness and to aid in later discussions, the three approaches to compression testing are briefly discussed.

2.1.1 Shear-Loaded Fixtures

Shear-loaded compression test fixtures are the most widely used type. A representation of the essential components of such a fixture is shown in figure 2.1. Figure 2.1 is based on the well-known IITRI test fixture[23]. The specimen to be tested is tabbed as shown and then gripped between two sets of jaws. The jaws apply a compressive load to the specimen by shear, through the tabbing. The specimen region between the tabbing is called the test section. Depending on the type of test and thickness of the specimen, the test section can vary from 0.1 to 1 in. in length. If the test section is shorter than or close to the critical half-wavelength of the specimen material, the fixture will restrain the specimen from failing in the short-wavelength buckling mode. If there is waviness in the specimen, then the influence of such imperfections may also be restrained by the fixture, the fixture causing the material to behave differently than it would in a structural component.

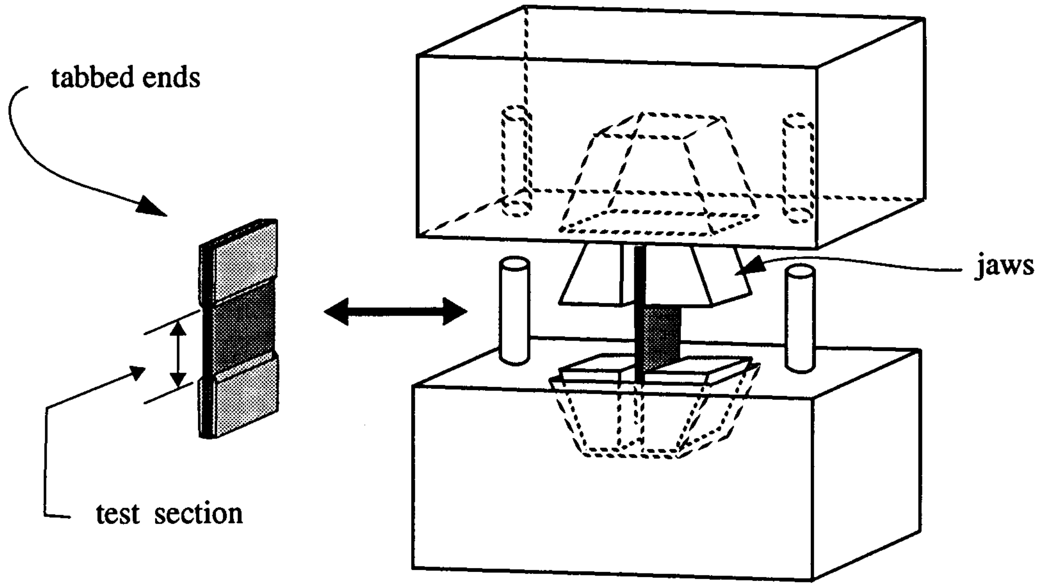

Figure 2.1 Shear-loaded compression test fixture.

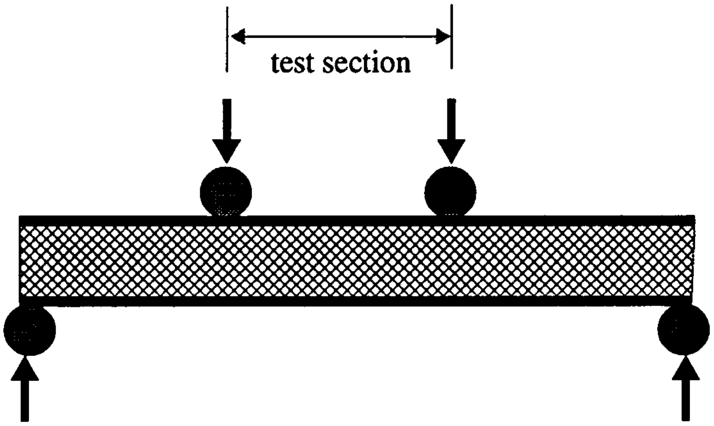

Figure 2.2 Sandwich-beam compression test.

2.1.2 Sandwich-Beam Test Fixtures

Sandwich-beam tests[24] are probably the most controversial, and also give the highest strength measurements. A representation of a sandwich specimen loaded in four-point bending is shown in figure 2.2. Ideally the region indicated in figure 2.2 as the test section should be in pure compression. One side of the laminate to be tested is bonded to the sandwich core material, most likely honeycomb. Unfortunately this sandwich material also acts like an elastic foundation, providing support to the laminate and reducing the effects of short-wavelength buckling and initial imperfections. This is why sandwich-beam tests give extremely high results.

2.1.3 End-loaded Test Fixtures

A typical end-loaded fixture is shown in figure 2.3. Here the compressive load is applied through the two parallel plates at the ends of the specimen. Great care must be taken to ensure that the ends of the specimen are machined flat and parallel, or premature failure at the end will result. If the specimen is not thick enough or short enough global (Euler) buckling may occur. Certain end-loaded fixtures lightly clamp the ends of the specimen in place to prevent end brooming, although some researchers feel the clamping action causes premature failure due to other end effects. Because this type of fixture does not seem to restrain the specimen from short-wavelength buckling types of failures, it was chosen for the present work.

2.2 Compression Test Results

Forty-two angle-ply IM7/8551-7a specimens with a lay-up of $[(\pm\theta)/(\mp\theta)]_{6s}$ were tested in compression. The range of θ that was tested included: 0°, 5°, 10°, 15°, 20°, 30°,

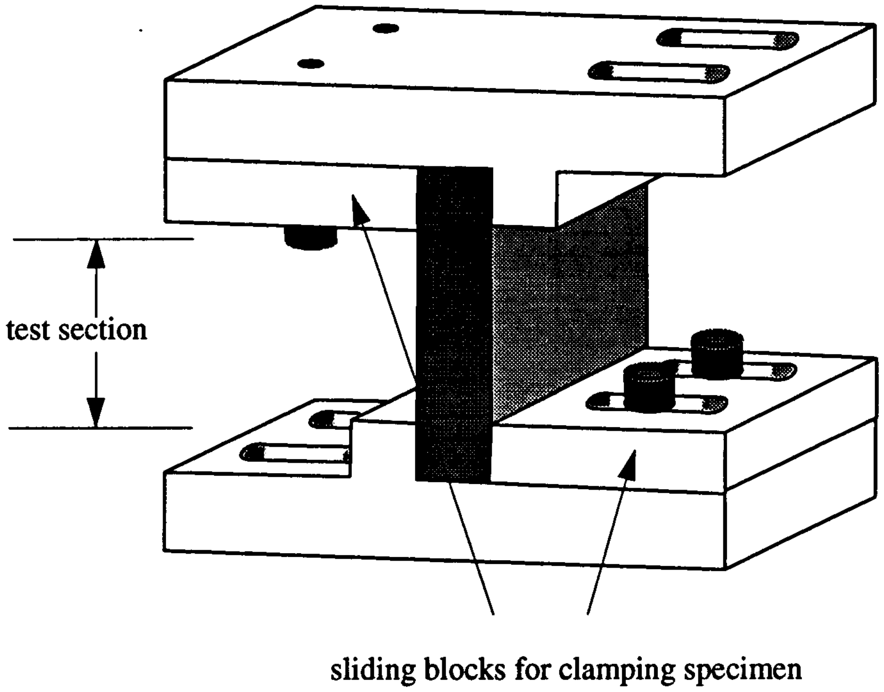

Figure 2.3 End-loaded compression test fixture.

45°, 60°, 70°, 75°, 80°, 85°, and 90°. The following sections describe the specimens and testing set-up in more detail.

2.2.1 Specimen Geometry and Strain Gage Set-up

Seven 6 in. by 7 in. panels with lay-ups of 0°, 5°, 10°, 15°, 20°, 30°, 45° were fabricated and cured at the NASA Langley Research Center. Six specimens were cut from each panel. A sketch of a typical panel is shown in figure 2.4. For example, if a panel had a lay-up of $[(\pm 5)/(\mp 5)]_{6s}$, then three specimens (such as 1, 2, 3 in figure 2.4) would be cut parallel to the 0° direction and three specimens (such as 4, 5, 6) would be cut parallel to the 90° direction. Therefore the lay-up for the second three specimens would be $[(\mp 85)/(\pm 85)]_{6s}$. For convenience, all laminates will be referred to as $[(\pm\theta)/(\mp\theta)]_{6s}$ laminates. As can be inferred, there are three replicate specimens for a given θ, except for $\theta = 45°$, for which there are six. More will be said of these six specimens later.

Through use of an acid digestion test the average fiber volume fraction of the panels was determined to be 53.9%. The acid digestion test may have consumed a small amount of fiber also, so a nominal fiber volume fraction of 55% will be assumed.

The test specimens were nominally 1.75 in. long, 1.5 in. wide, and 48 plies thick. A micrometer was used to accurately measure specimen dimensions. The average length, width, and thickness, respectively, were 1.754 in., 1.505 in., and 0.275 in. The average thickness of each ply was thus taken to be 0.00573 in. Each specimen had five strain gages attached to it, with two pairs of the gages affixed to the front and back of the specimen as shown in figure 2.5. These gages measured axial strains. The four gages could also be used to monitor side-to-side and through-the-thickness bending of the specimen. The fifth strain gage

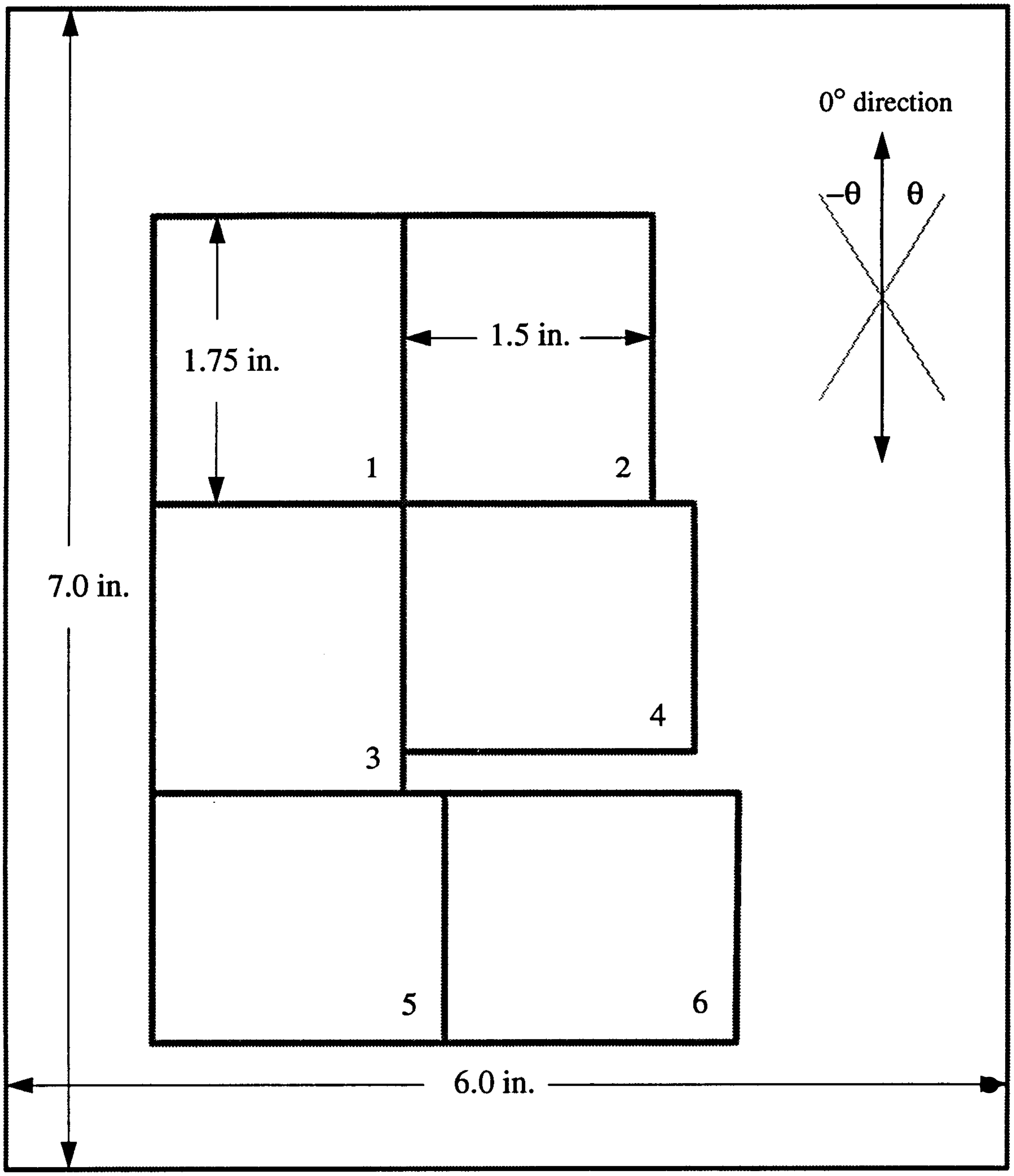

Figure 2.4 Panel configuration that specimens were cut from.

ORIGINAL PAGE
BLACK AND WHITE PHOTOGRAPH

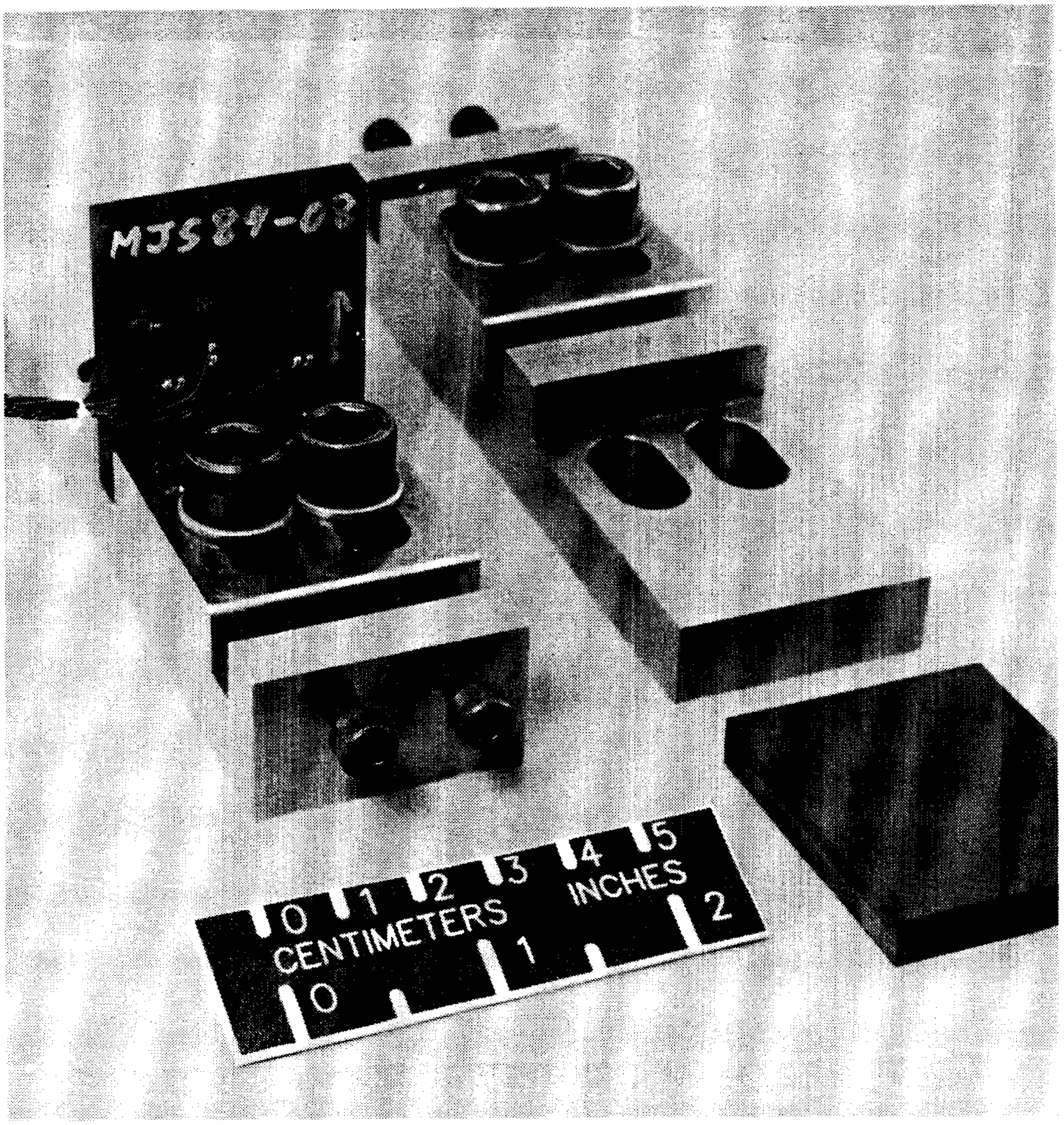

Figure 2.5 Short-block compression test fixture.

was mounted in the transverse direction of the load. A DCDT (direct current displacement transducer) was also used to measure the change in length of the specimen.

2.2.2 Test Fixture

The short-block compression test fixture used is shown in figure 2.5. This fixture is similar to the one used in reference 22 except that here the specimen ends are held in place, in the thickness direction of the specimen, with plates that can be secured with Allen screws. In addition, another smaller set of Allen screws were used to position these plates. A 10° specimen had a faulty strain gage and was tested at a later date. At the later time the fixture of figure 2.5 was not available so a slightly different[22] fixture was used. These two fixtures are simple to use and have been used successfully for previous material characterization studies.

2.2.3 Test Data

The output from the four strain gages in the load direction were combined to give an average strain. Normalized load vs. average axial strain, as measured by the strain gages, transverse strain as measured by the strain gage, and the axial strain as measured by the DCDT are plotted for each specimen tested. The specimen numbers in each of the following figures correspond to the order of the specimen's results listed in the table to follow. Figures 2.6 through 2.9 are for off-axis angles of 0° to 15°. In this range of θ the axial strains to failure are close to being linear. The axial strains as measured by the DCDT show the same slope as the strains measured with gages, but are offset by varying amounts at low loads. The axial strains as measured by the DCDT show this same trend throughout all of the tests. However, this trend is not as noticeable in the softer specimens. Note that for convenience the negative of the transverse strain has been plotted.

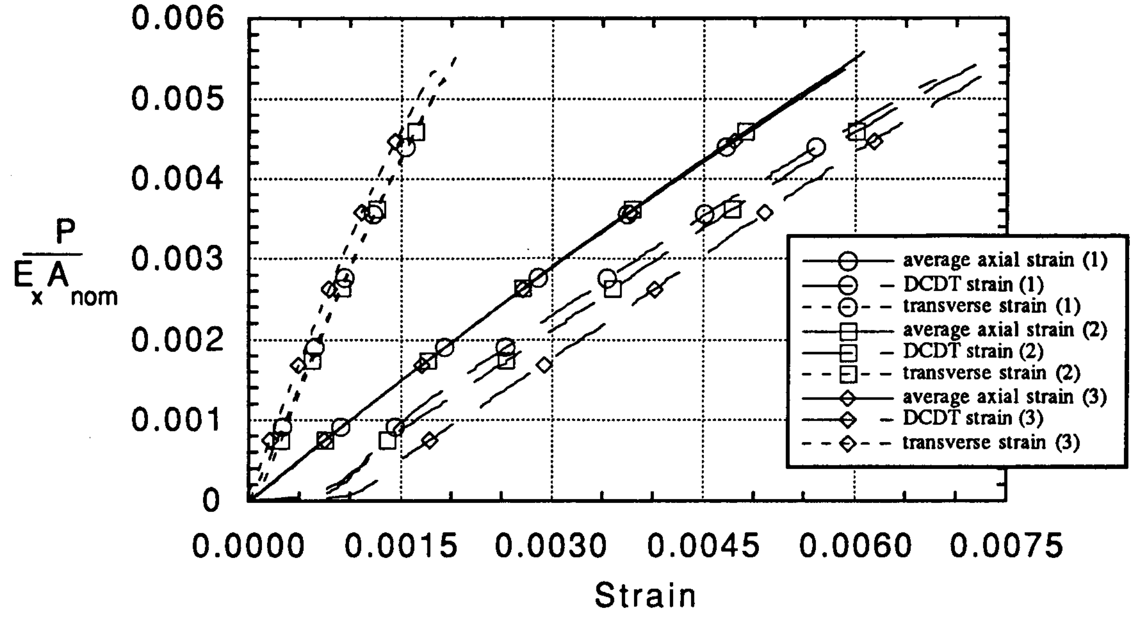

Figure 2.6 Experimental results for the 0° specimens.

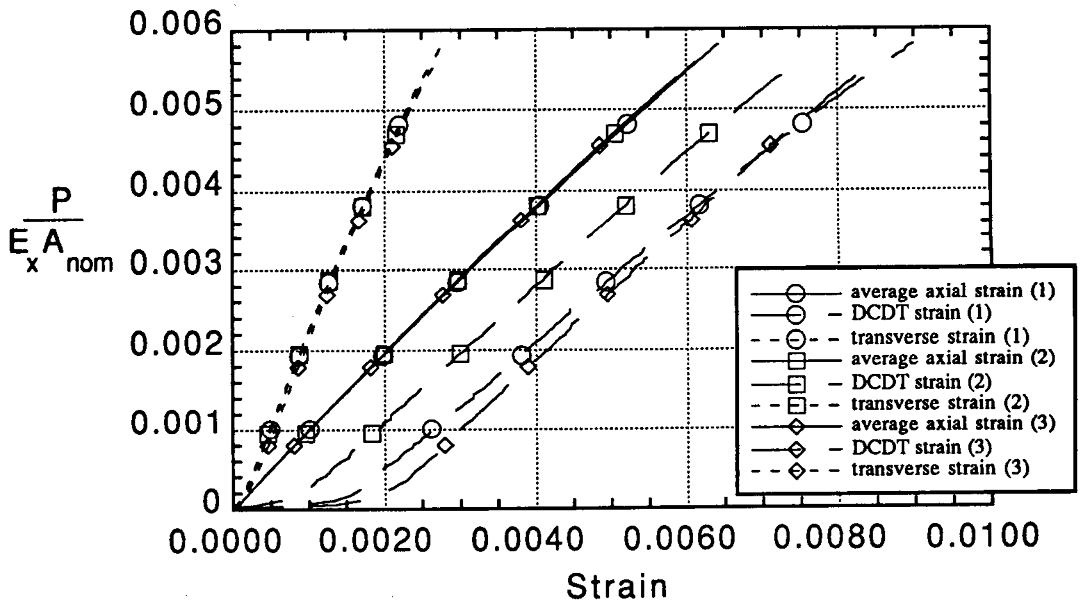

Figure 2.7 Experimental results for the 5° specimens.

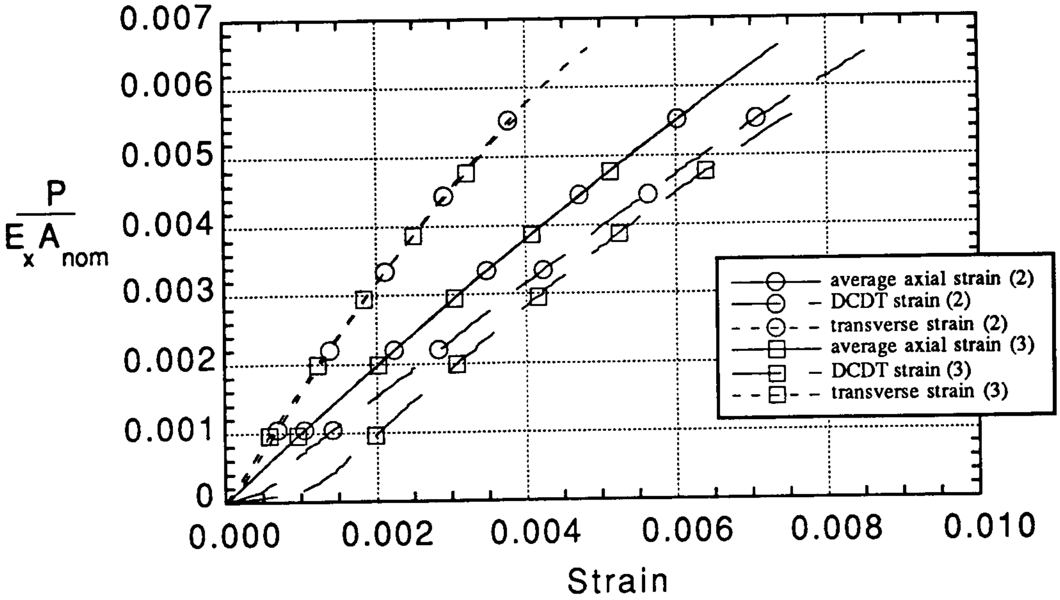

Figure 2.8 Experimental results for the 10° specimens.

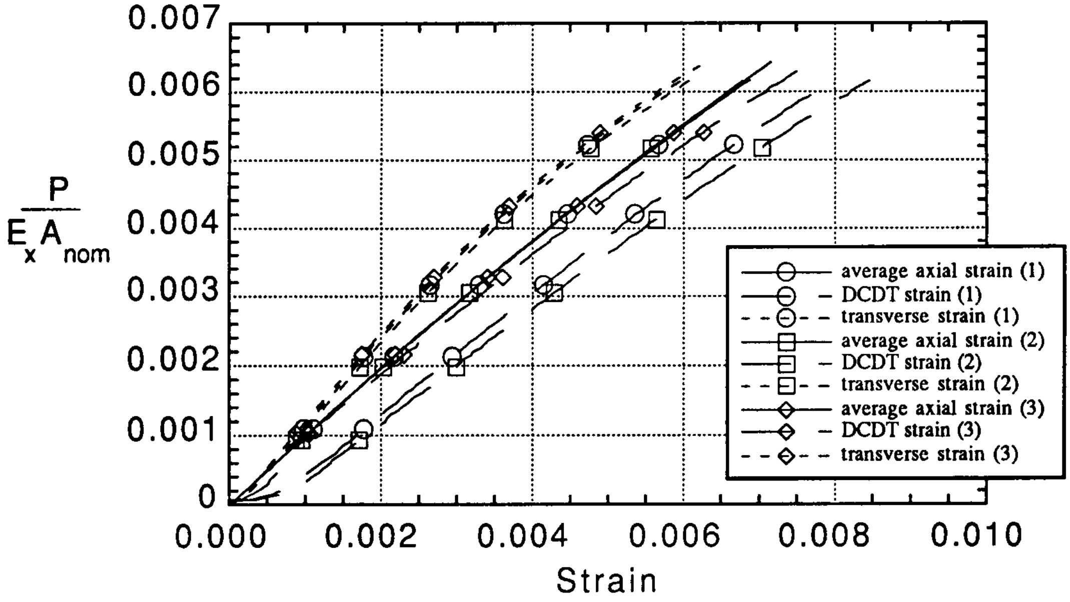

Figure 2.9 Experimental results for the 15° specimens.

Figures 2.10 and 2.11 are for the 20° and 30° specimens. Here the axial and DCDT-measured strains are, for the most part, linear to failure. However the transverse strains are beginning to become nonlinear, especially at higher loads. Figures 2.12 through 2.14 are for the 45° and 60° specimens. Here all strains are nonlinear to failure. For the 45° specimens a definite 'knee' can be seen in all the strains, before and after which, the strains are quite linear. In these figures it can be seen that the strain gages reached their maximum capability at about 0.037 in./in., as indicated by vertical lines in the plots. The specimens in this range showed extremely high strains to failure, probably due to irreversible stiffness changes in the specimens. Figures 2.15 through 2.19 are for 70° to 90° specimens. The transverse strains are quite small, and show nonlinearity at loads close to failure. The slightly nonlinear axial strains as measured by the gages and as measured by the DCDT closely correspond to each other. Some of the strain gages have reached their maximum limits, indicating high strains.

Table 2.1 tabulates failure stresses, failure strains, Young's modulus, and Poisson's ratio for each specimen. Stresses are tabulated as load divided by the nominal area, A_{nom}. As discussed above, the load-strain relations for some specimens with larger off-axis angles are quite nonlinear. Hence a least-squares fit over the first one-fifth of the data for each specimen is used to obtain the Young's modulus for that specimen. Because of erratic transverse strain gage readings at very low loads and at loads close to failure, Poisson's ratio is calculated at a point near 40% of the failure load for each specimen. Figures 2.20, 2.21, 2.22, and 2.23 display some of the data in Table 2.1 graphically. Figure 2.20 shows the relationship between compression strength and off-axis angle. The average of the three replicate tests, as well as the individual data, are shown. As can be seen in figure 2.20, the strength is a monotonically decreasing function of off-axis angle. Between $\theta = 0^\circ$ and $\theta =$

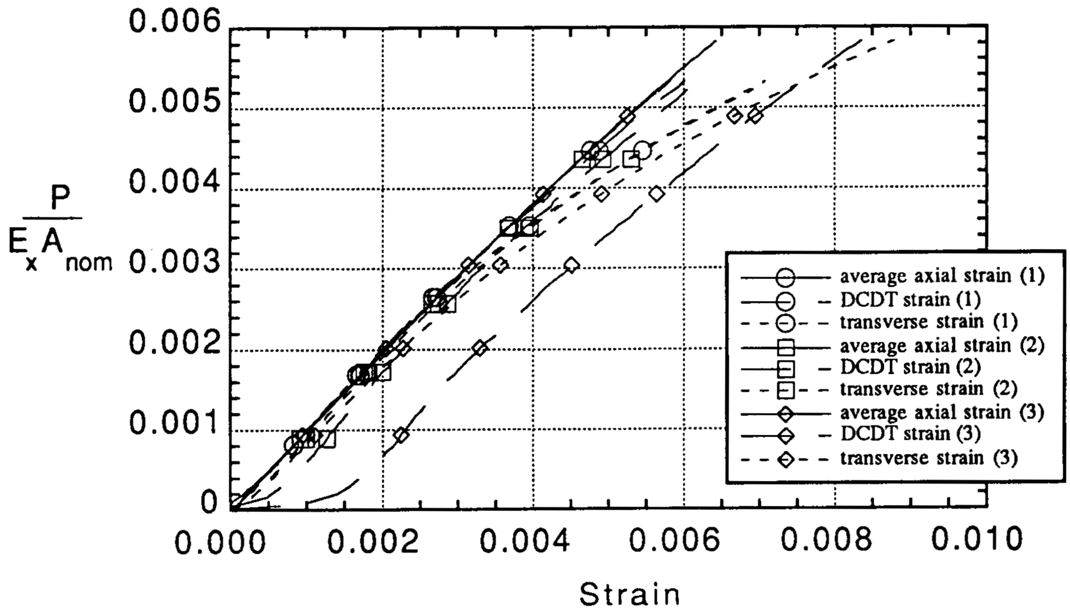

Figure 2.10 Experimental results for the 20° specimens.

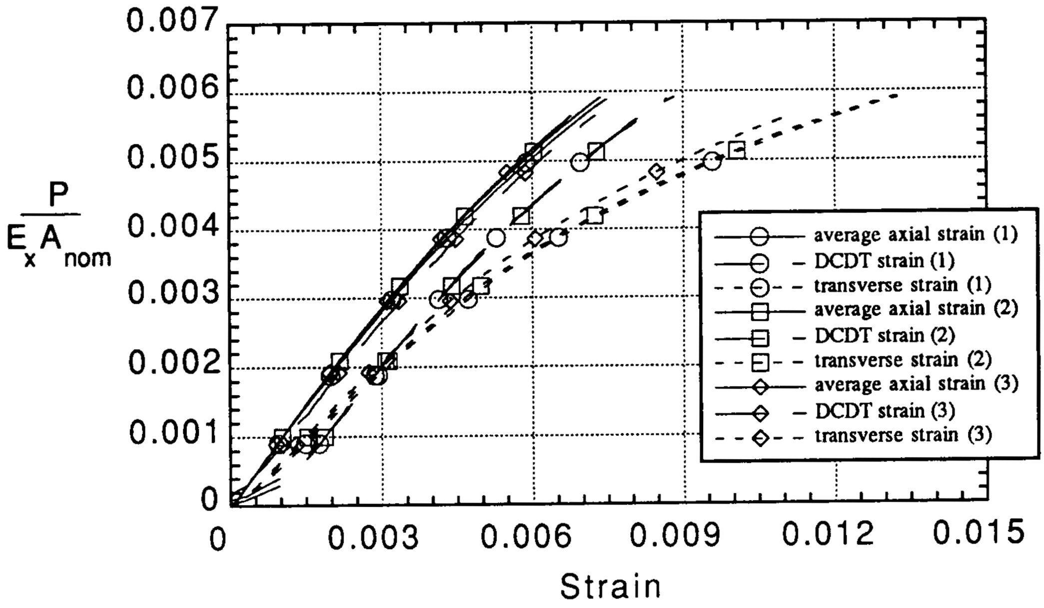

Figure 2.11 Experimental results for the 30° specimens.

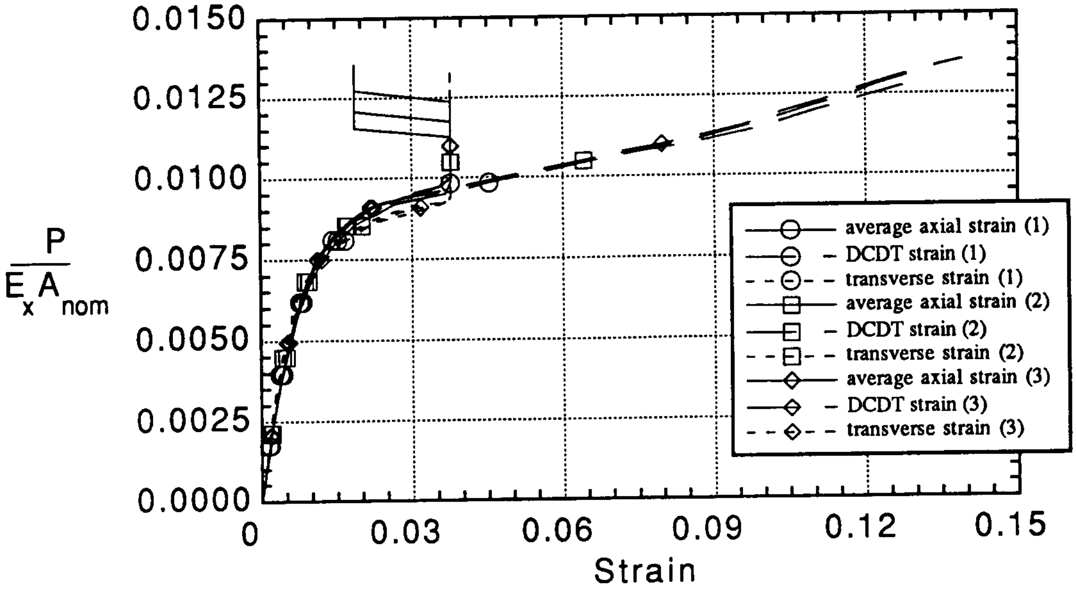

Figure 2.12 Experimental results for the first three 45° specimens.

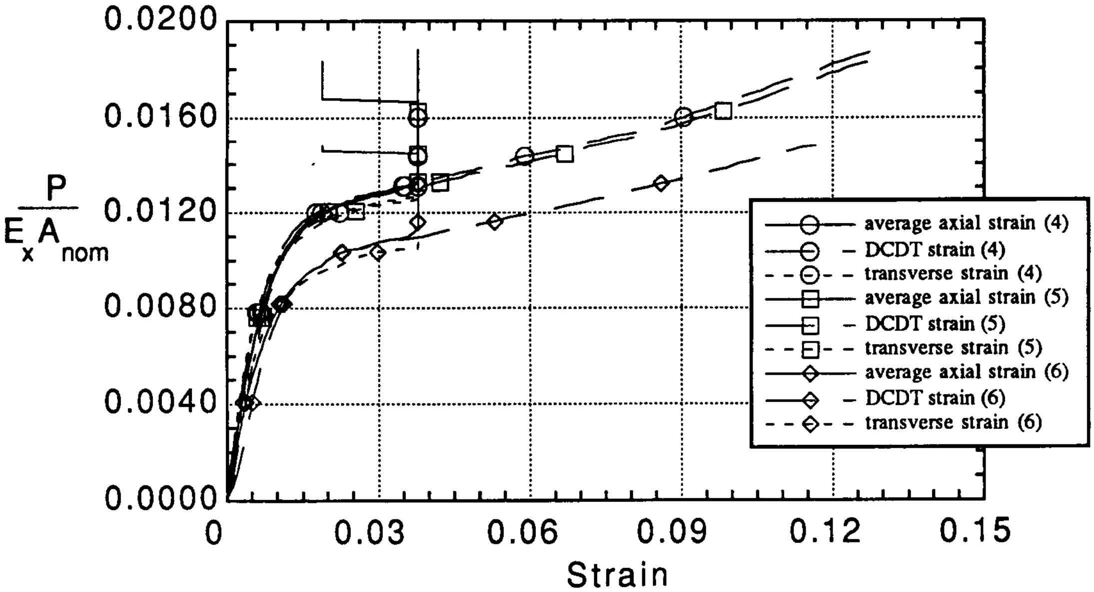

Figure 2.13 Experimental results for the last three 45° specimens.

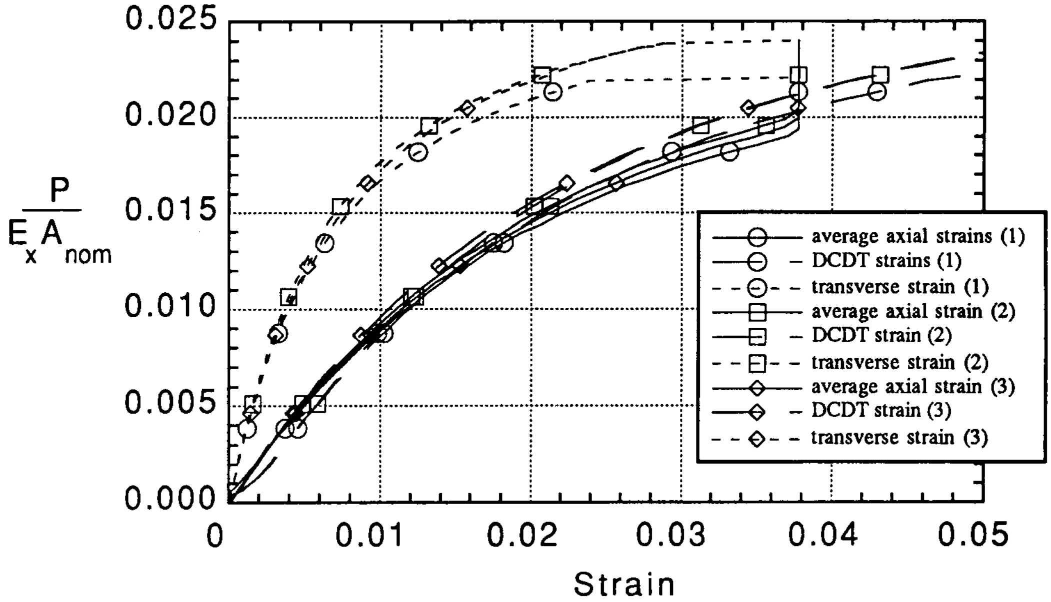

Figure 2.14 Experimental results for the 60° specimens.

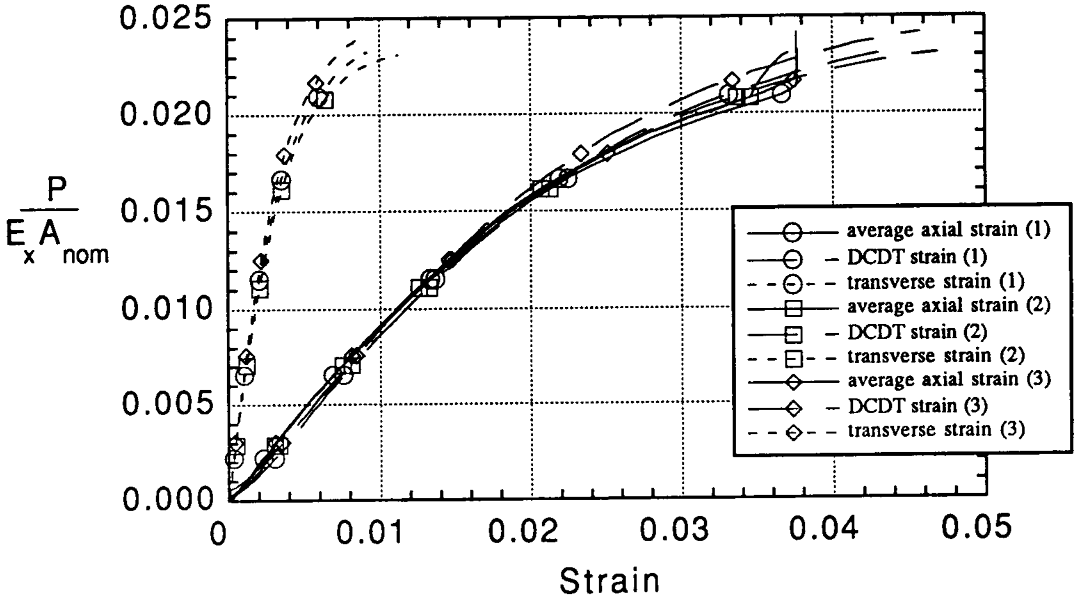

Figure 2.15 Experimental results for the 70° specimens.

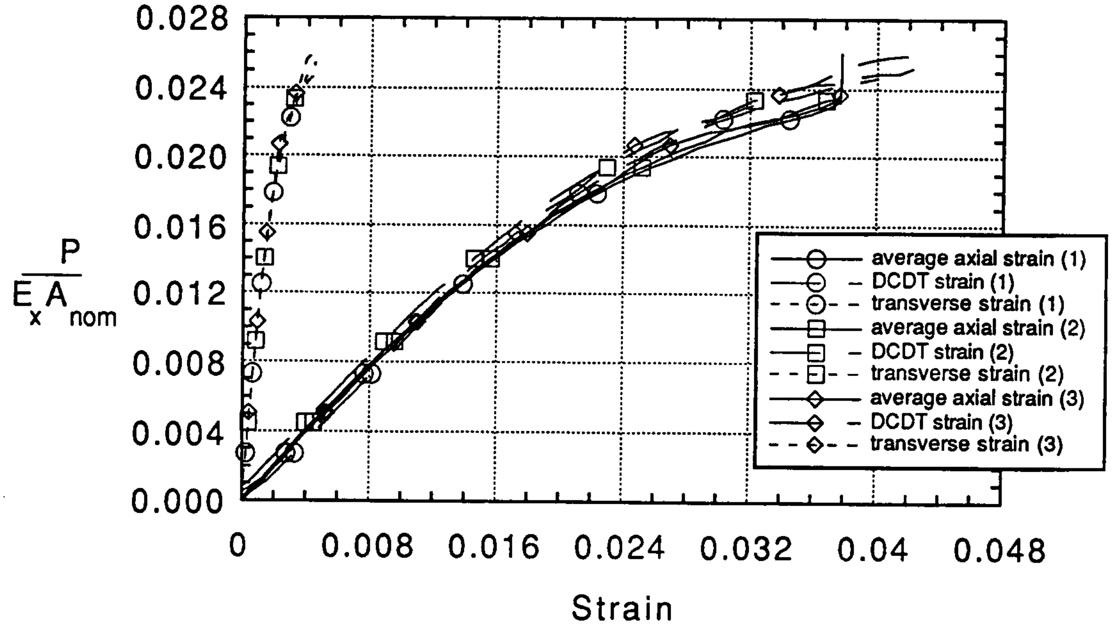

Figure 2.16 Experimental results for the 75° specimens.

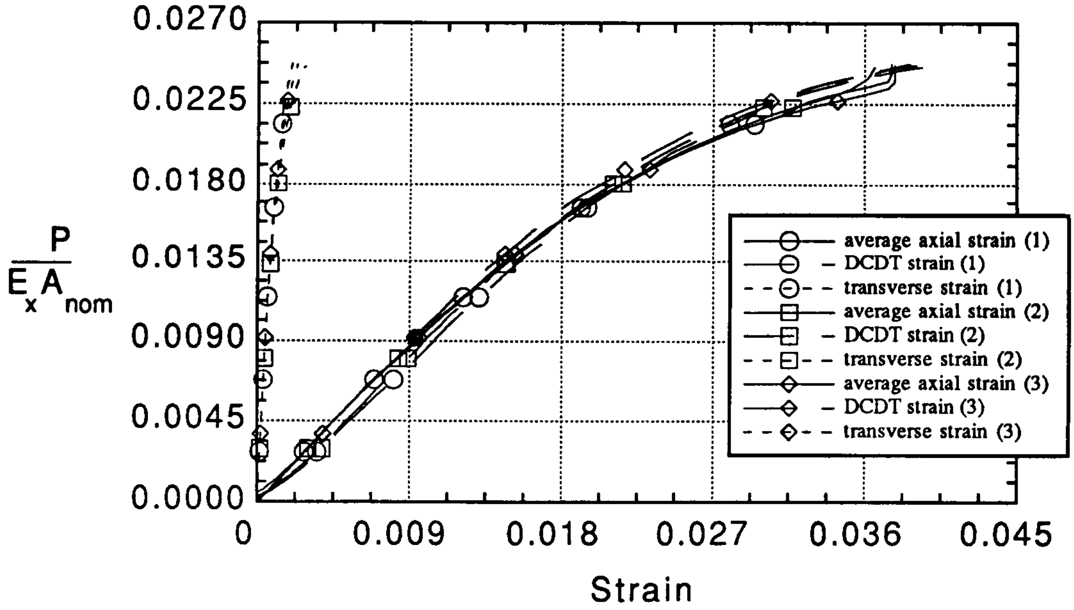

Figure 2.17 Experimental results for the 80° specimens.

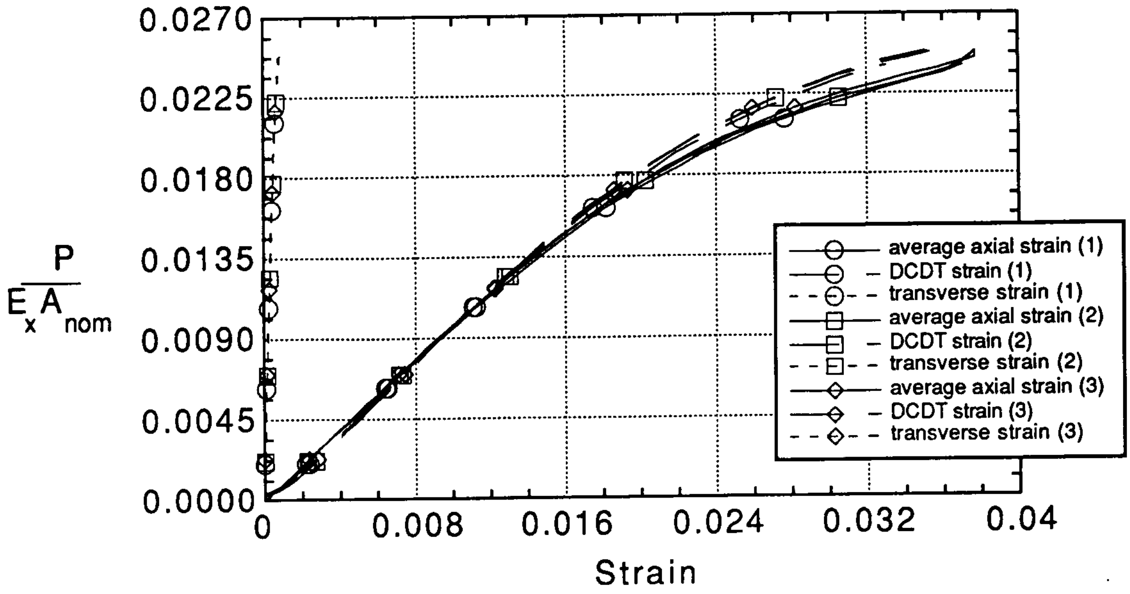

Figure 2.18 Experimental results for the 85° specimens.

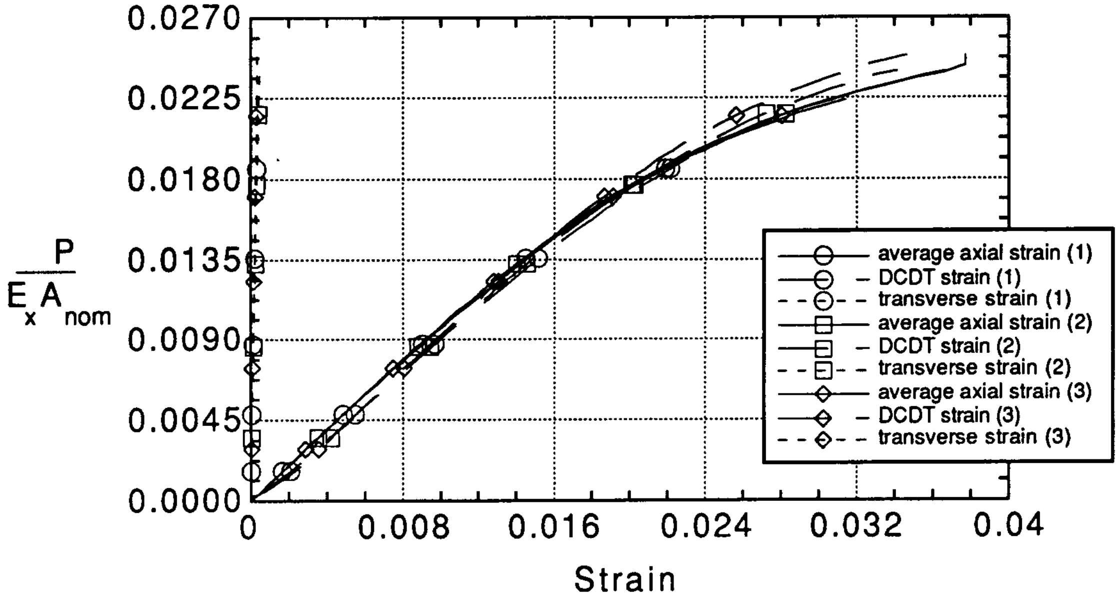

Figure 2.19 Experimental results for the 90° specimens.

Table 2.1 IM7/8551-7a Experimental Results

Angle	$\sigma_{x,\text{failure}}$ (ksi)^a		$\varepsilon_{x\,\max}$ (x 10^{-3})				E_x (Msi)		ν_{xy} (@ 40% max. load)	
			gage strain		DCDT strain					
0	111		5.74		6.79		21.1		0.335	
0	117	114^b	6.09	5.91^b	7.42	7.20^b	20.8	21.0^b	0.346	0.323^b
0	114		5.90		7.39		21.8		0.288	
5	119		6.43		9.00		20.5		0.439	
5	112	113	6.13	6.16	7.53	8.26	20.1	20.2	0.436	0.446
5	108		5.88		8.24		20.0		0.462	
10	103		-----				-----		-------	
10	122	111	7.37	6.82	8.71	8.21	18.6	18.8	0.615	0.609
10	107		6.26		7.71		19.0		0.603	
15	104		7.17		7.70		16.1		0.793	
15	101	102	6.80	6.95	8.46	8.06	16.4	16.3	0.838	0.813
15	101		6.88		8.01		16.4		0.807	
20	69.2		5.82		6.01		12.9		0.975	
20	66.8	70.7	5.67	5.97	6.04	6.8	12.7	12.8	1.025	1.037
20	76.0		6.43		8.35		12.9		1.111	
30	44.7		7.49		8.68		7.41		1.468	
30	44.8	44.0	7.37	7.21	8.83	8.26	7.56	7.49	1.453	1.439
30	42.4		6.78		7.27		7.51		1.396	
45	33.9		-----^{c}		127		2.67		0.867	
45	34.9	34.2	-----		129	132	2.71	2.71	0.851	0.886
45	33.9		-----		139		2.74		0.940	
45	34.8		-----		129		2.07		0.857	
45	34.6	34.5	-----		129	125	2.10	2.22	0.862	0.865
45	34.2		-----		117		2.48		0.875	
60	33.1		-----		58.2		1.50		0.336	
60	33.8	33.2	-----		55.9	56.2	1.43	1.47	0.331	0.334
60	33.8		-----		54.5		1.49		0.334	
70	33.0		-----		44.9		1.38		0.152	
70	33.6	33.2	-----		46.9	45.9	1.43	1.39	0.163	0.154
70	33.0		-----		45.8		1.37		0.146	
75	32.1		-----		40.1		1.32		0.0837	
75	33.4	33.3	-----		42.8	42.0	1.32	1.32	0.0860	0.0844
75	34.5		-----		43.1		1.33		0.0835	
80	32.5		-----		38.6		1.31		0.0503	
80	32.4	32.5	36.6		39.4	39.0	1.31	1.32	0.0499	0.0502
80	32.4		-----^{c}		39.0		1.34		0.0504	
85	31.6		37.1		33.0		1.29		0.0244	
85	32.0	32.0	-----^{c}	37.3	35.4	34.5	1.28	1.29	0.0259	0.0249
85	32.3		37.4		35.2		1.29		0.0245	
90	30.9		31.4		30.6		1.30		0.0164	
90	31.4	31.4	36.8	35.3	34.1	33.1	1.29	1.28	0.0173	0.0160
90	32.0		37.7		34.6		1.26		0.0144	

a - P/A_{nom} b - average values in this column c - strain gage reached upper limit

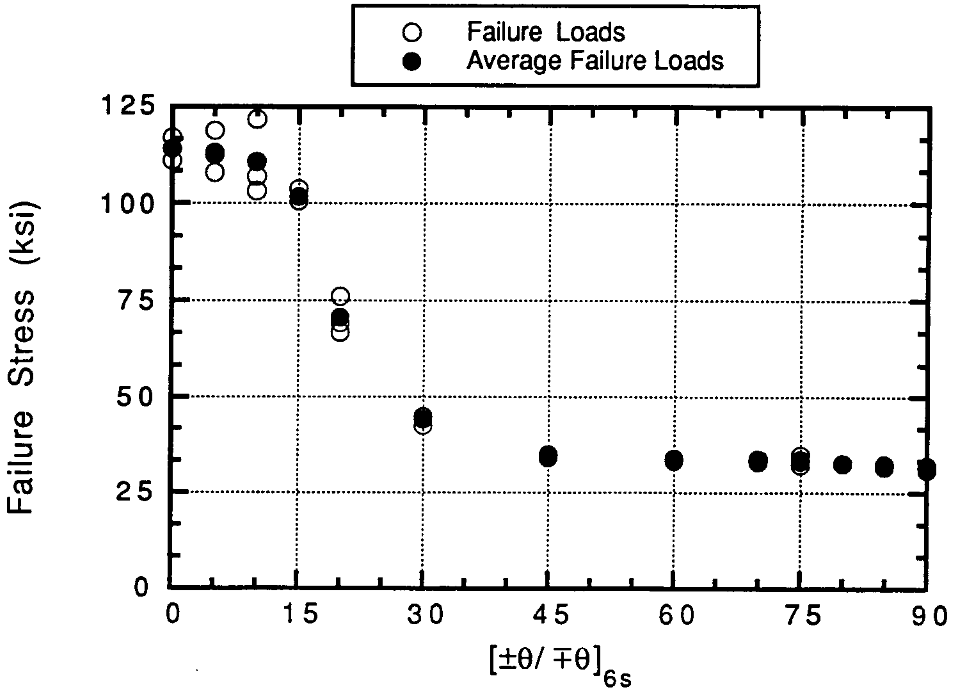

Figure 2.20 Failure loads as a function of off-axis angle.

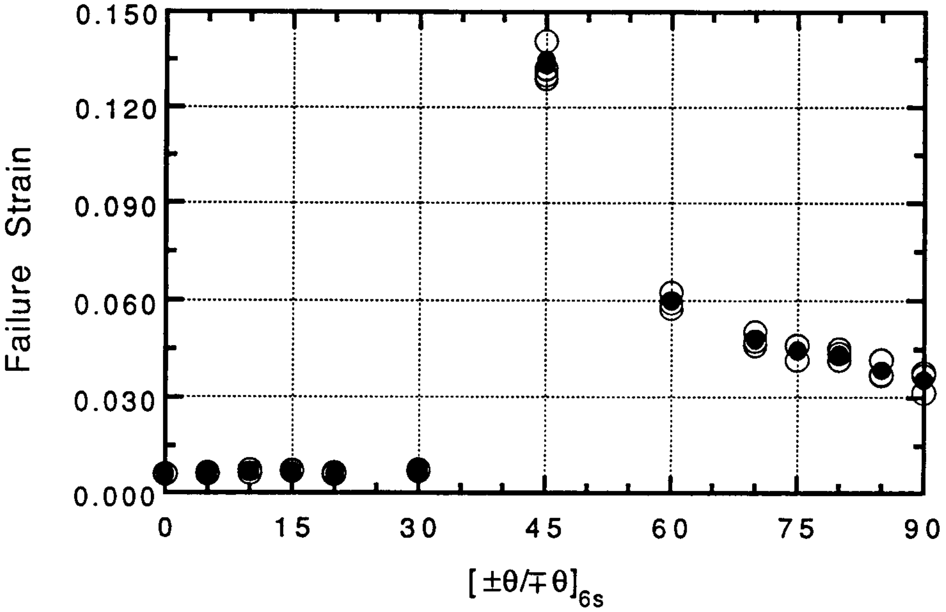

Figure 2.21 Failure strains as a function of off-axis angle.

15° the strength decreases about 15%. Between $\theta = 15°$ and $\theta = 45°$ the strength decrease is more rapid. For $\theta > 45°$ strength is essentially independent of θ. Figure 2.21 illustrates the relationship between the axial strain at failure and off-axis angle. The failure strains were so large in the range $45° \leq \theta \leq 75°$ that the strain gages stopped functioning. This was discussed earlier when the experimental strain vs. load data were illustrated. As a result, the DCDT data were used to compute failure strains for the higher off-axis angles. These data points are adjusted to account for the fact that the DCDT did not measure the change of length of the specimen directly, rather it measured the change in distance between the heads of the load frame within which the test fixture was situated. Elastic effects of the fixture on the DCDT were accounted for by calculating the amount the fixture compressed. Quite a wide range in failure strains is shown in figure 2.21. For $\theta \geq 45°$, and particularly at $\theta = 45°$, the failure mechanisms were such that large axial strains occurred just prior to failure. This large increase in the strain to failure at $\theta = 45°$ indicates the failure mode for this angle is quite different or perhaps more complex than the failure mode for, say, $\theta = 30°$.

The character of Young's modulus with off-axis angle, as shown in figure 2.22, is similar to that of strength. The modulus decreases as θ increases from 0° to 45°. For $\theta > 60°$ the modulus is basically constant. The Poisson's ratios illustrated in figure 2.23 indicate large expansions in the transverse direction.

2.2.4 Failure Modes

Several distinct modes can be observed in the failed specimens. Failure modes for off-axis angles of 0°, 5, and 10° include kink bands, brooming, interlaminar shearing, inplane transverse tensile splitting, and some inplane shearing. A failed 0° specimen with brooming, kink bands, and splitting is shown in figure 2.24, a failed 5° specimen with brooming

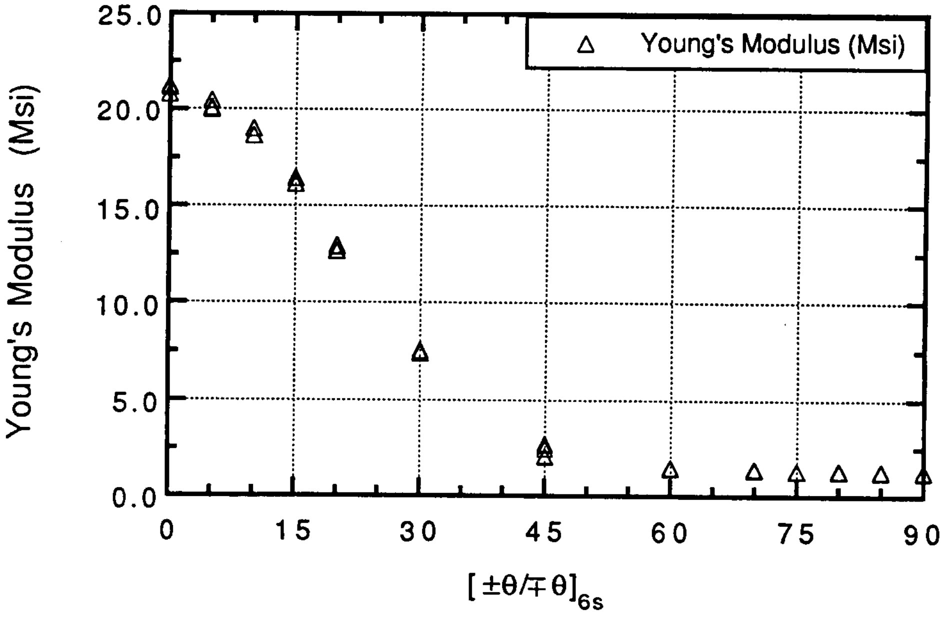

Figure 2.22 Young's modulus as a function of off-axis angle.

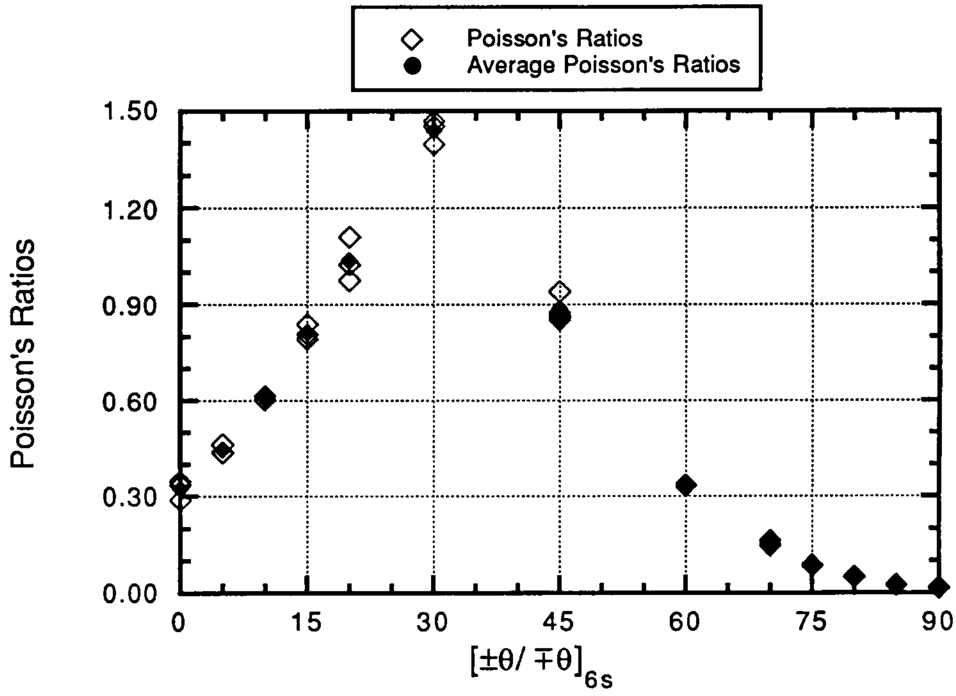

Figure 2.23 Poisson's ratios as a function of off-axis angle.

and kink bands is shown in figure 2.25, and a failed 10° specimen with brooming and inplane transverse tension or inplane shear failure is shown in figure 2.26.

The failure mode changes dramatically for angles of 15°, 20° and 30°. The predominate mode is inplane transverse tension failure or inplane shear, or a combination of the two. As shown with a failed 15° specimen in figure 2.27, and a failed 20° specimen in figure 2.28, the transverse tension or inplane shear types of failure occurs on planes parallel to the fibers. Failure due to either inplane transverse tension or due to inplane shear results in a clean break parallel to the fibers. All the specimens in this category show exactly the same type of failure.

Although the specimens in the 45° to 70° range are not the softest in the direction of loading, nor do they have the largest Poisson's ratios, they do exhibit the largest transverse and axial strains near the failure loads. In addition, they exhibit considerable inelastic deformation. For example, on the ends of the 45° specimen shown in figure 2.29, i.e., the surfaces bearing on the fixture, faint vertical lines are visible near the left and right edges. The lines represent impressions left by the fixture, the distance between the lines representing the width of the fixture. That there is material outside these lines means the compressed specimen extended beyond the width of the fixture. This is presumably due to Poisson's effects. However, upon failure the specimens remained permanently deformed. Similar faint markings on the surface with white writing indicate high through-the-thickness strains also. Comparable but faint markings are also found in figure 2.30, a 60° specimen. The failure modes for this range are inplane matrix shearing and matrix softening due to the nonlinear stress-strain behavior of the matrix. Failure strains are also highest for this group.

Edge views of 45° and 60° failed specimens are shown in figures 2.31 and 2.32. Through-the-thickness kink bands and delamination are evident, and the kink band angle

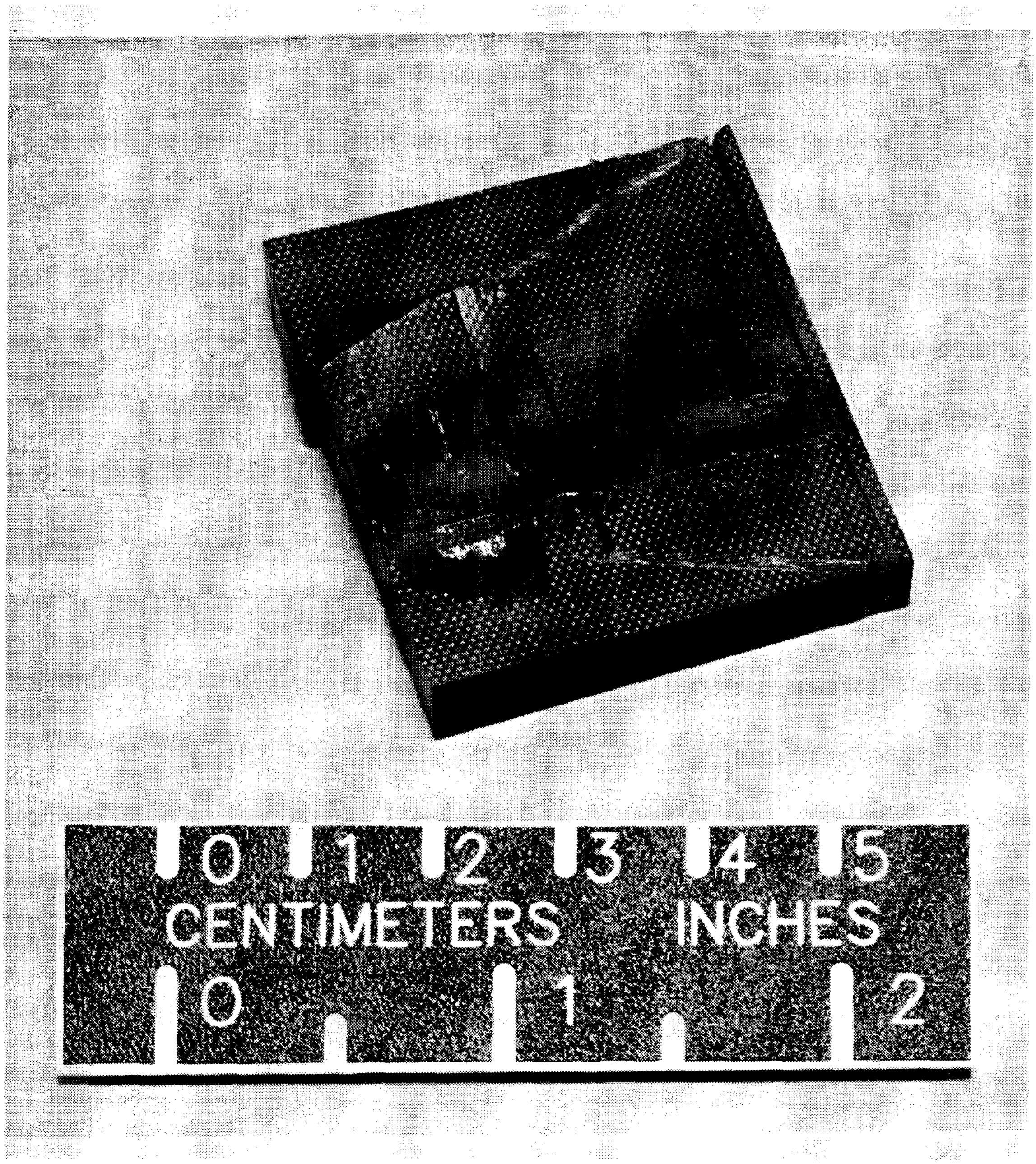

Figure 2.24 Failed 0° specimen with kink bands, splitting, and brooming.

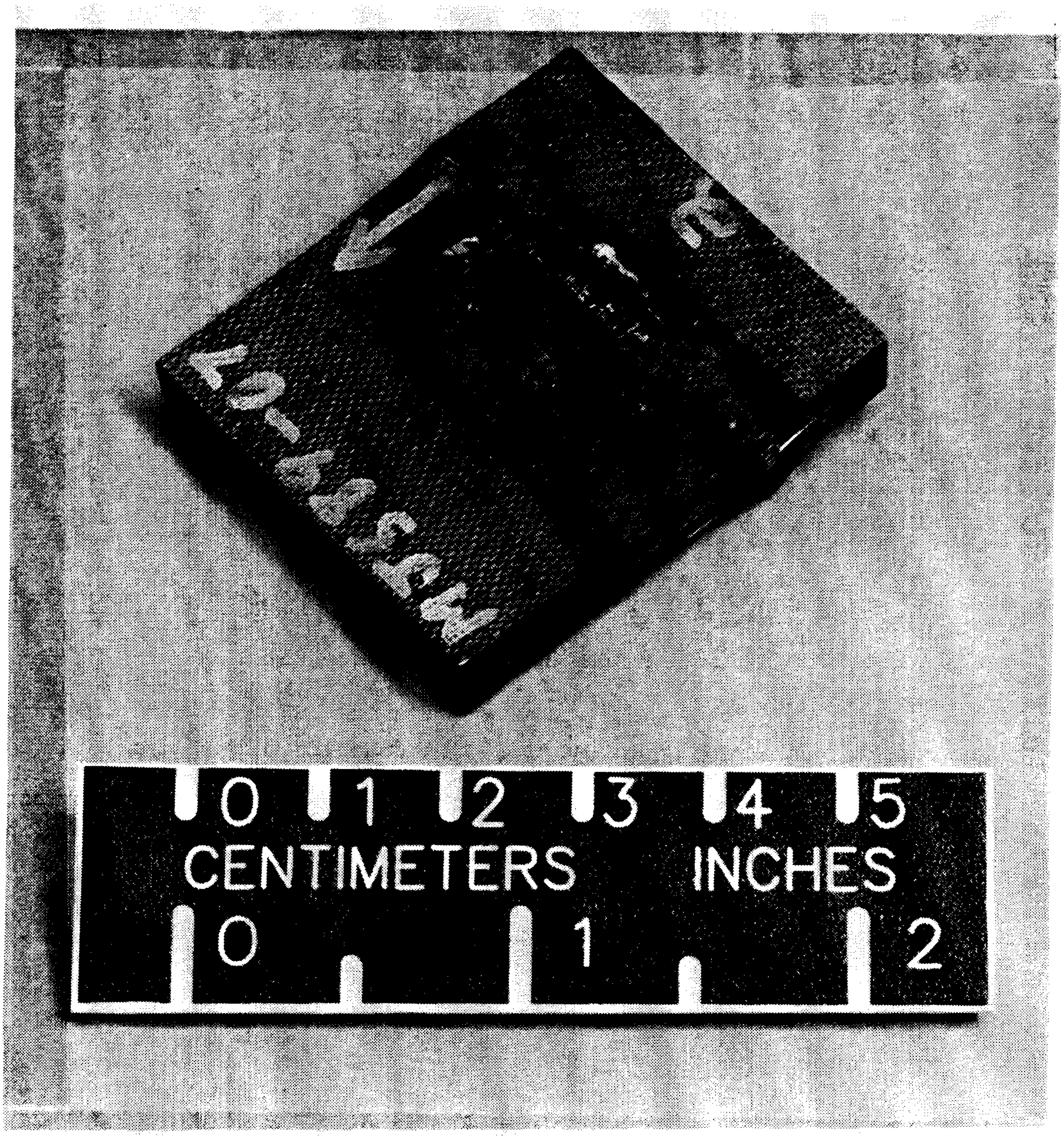

Figure 2.25 Failed 5° specimen with kink bands and brooming.

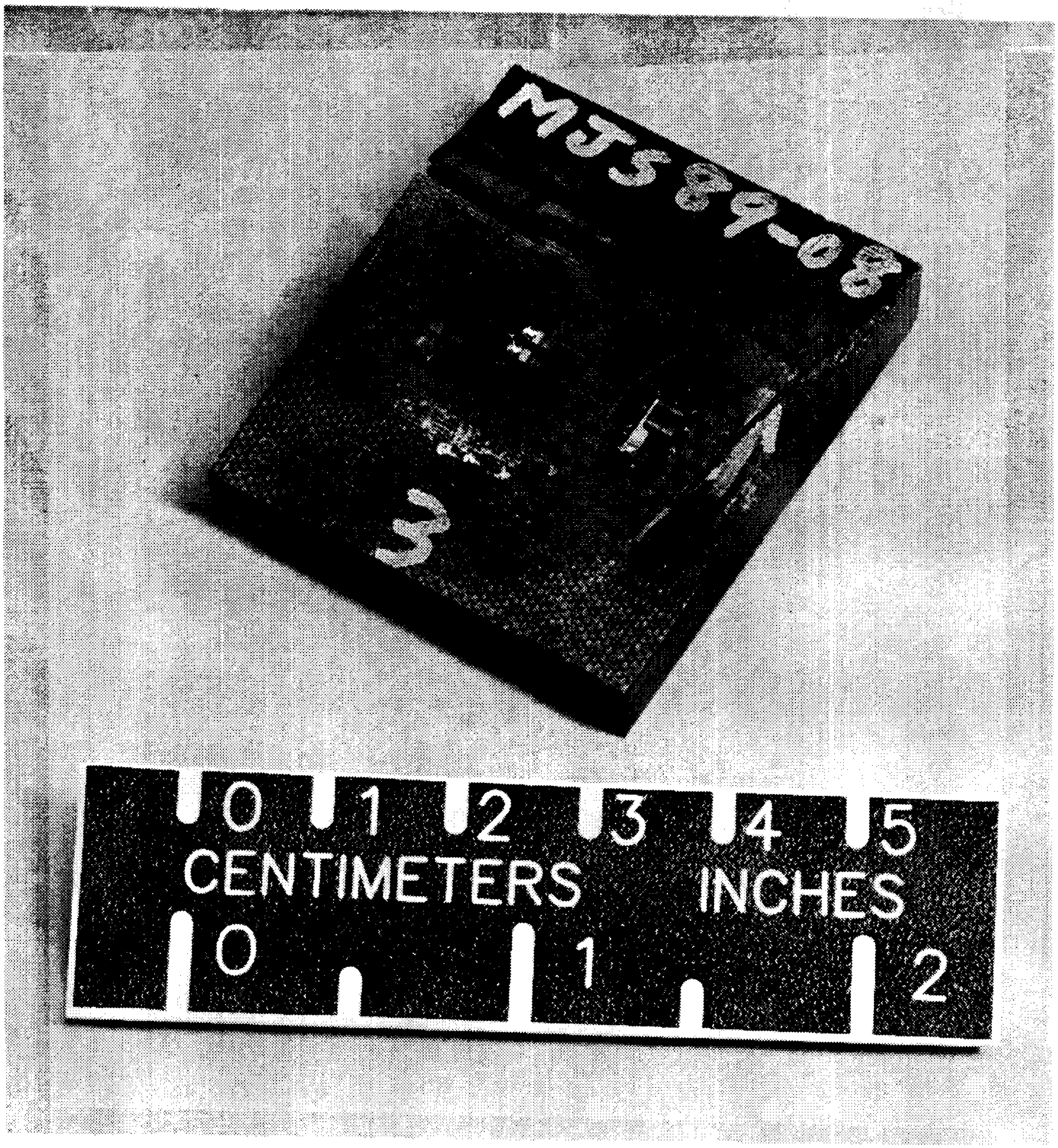

Figure 2.26 Failed 10° specimen with brooming, inplane shear, and transverse tension.

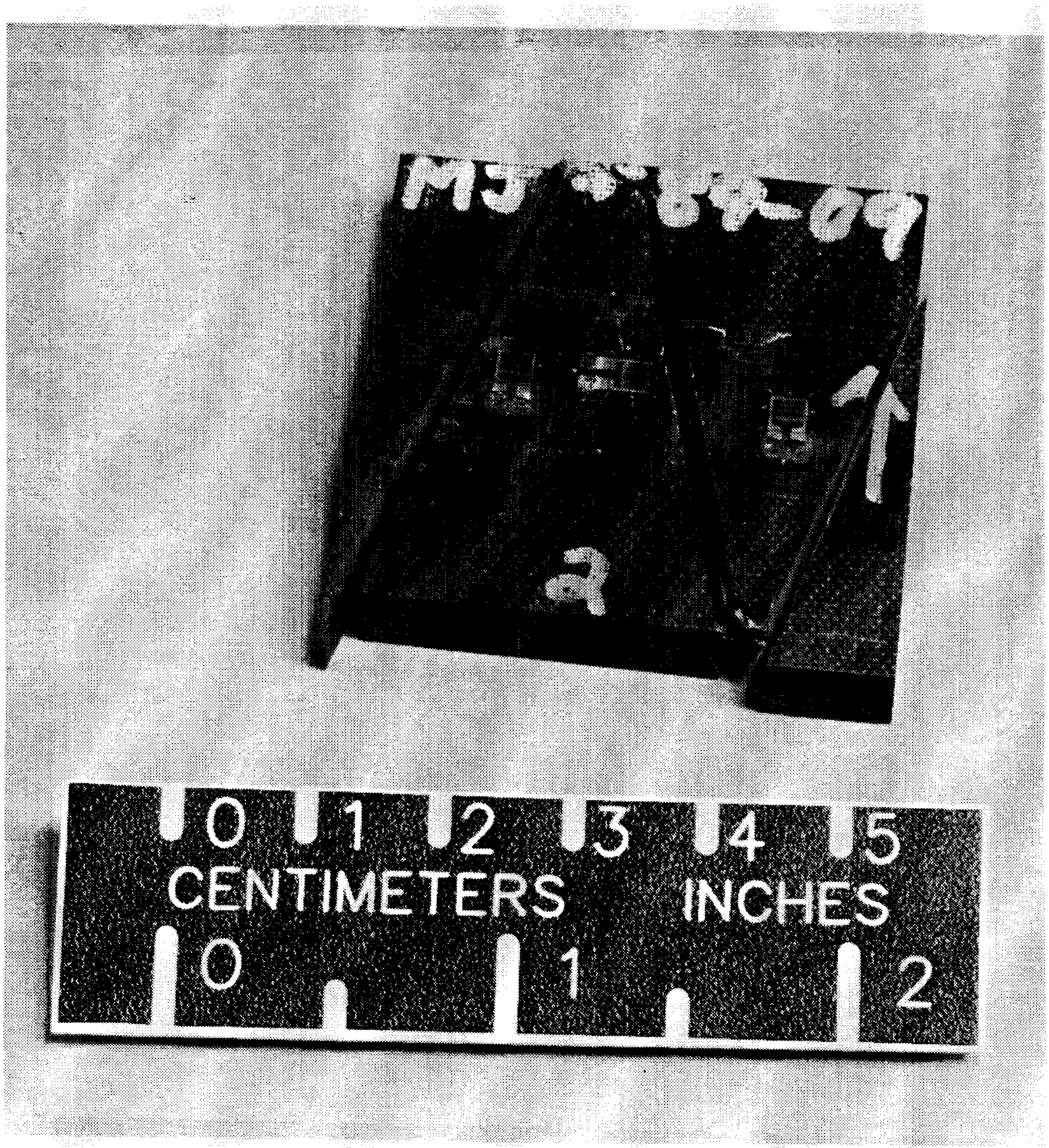

Figure 2.27 Failed 15° specimen with inplane transverse tension.

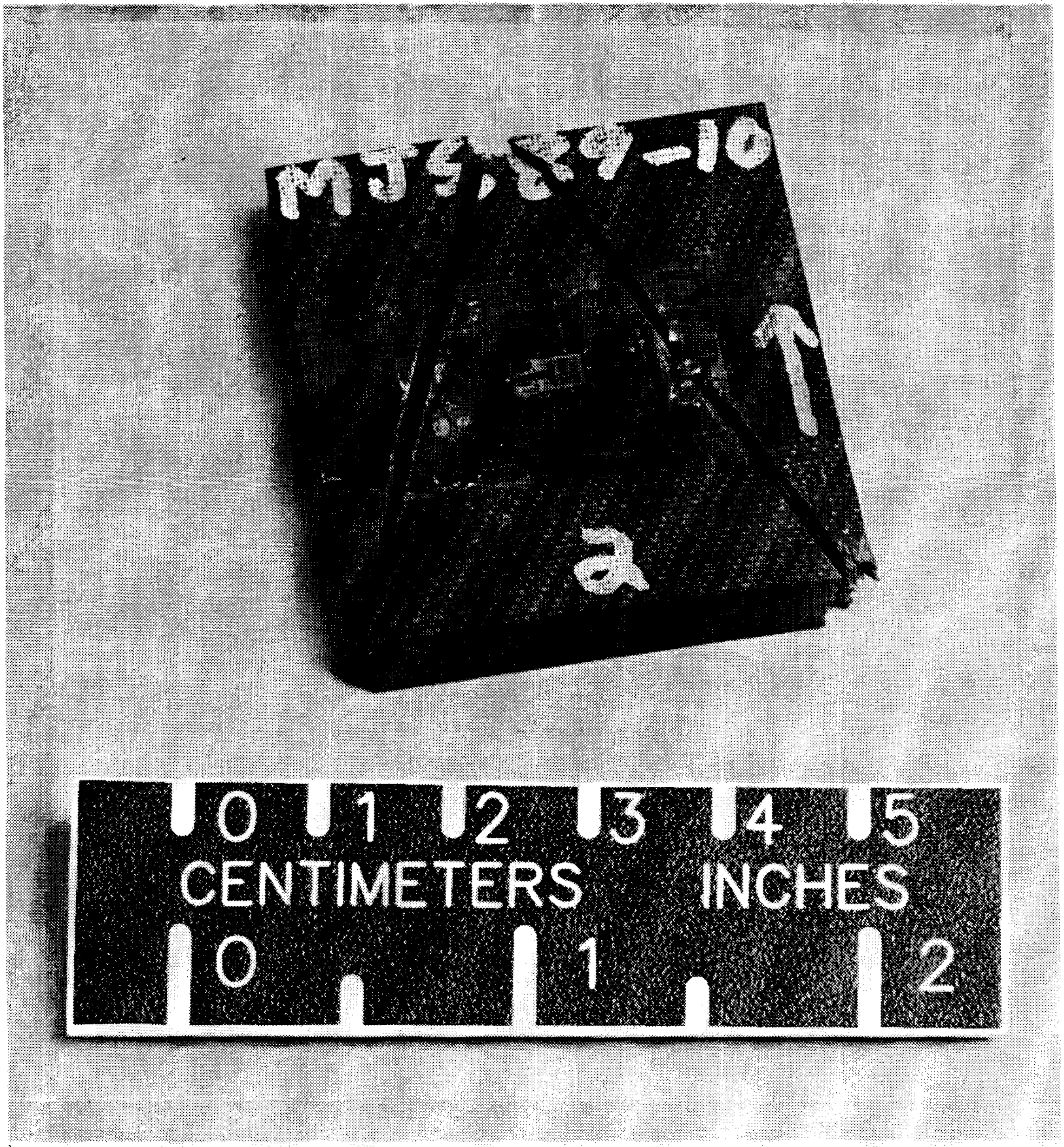

Figure 2.28 Failed 20° specimen with inplane transverse tension.

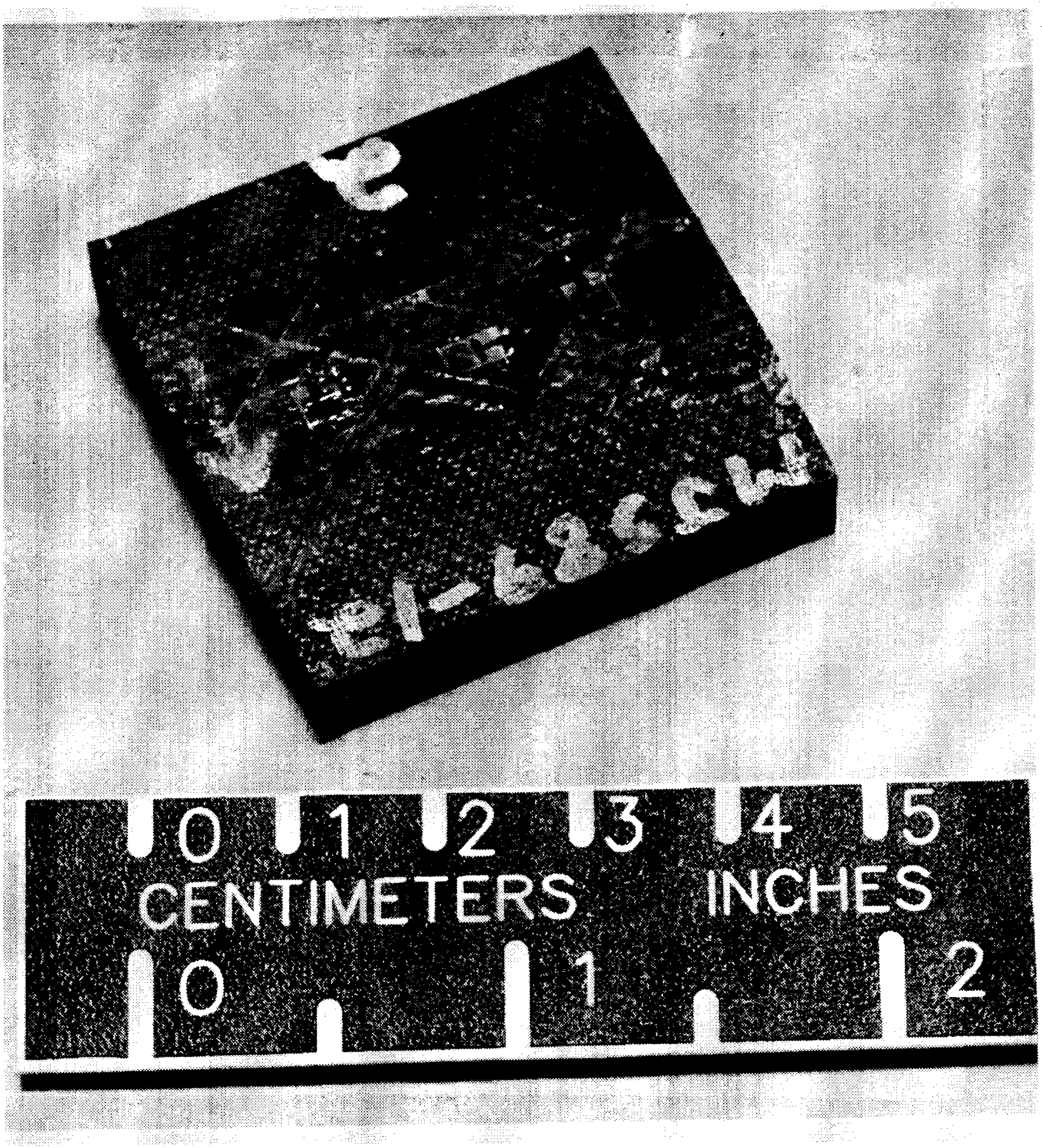

Figure 2.29 Failed 45° specimen with matrix softening.

Figure 2.30 Failed 60° specimen with matrix softening.

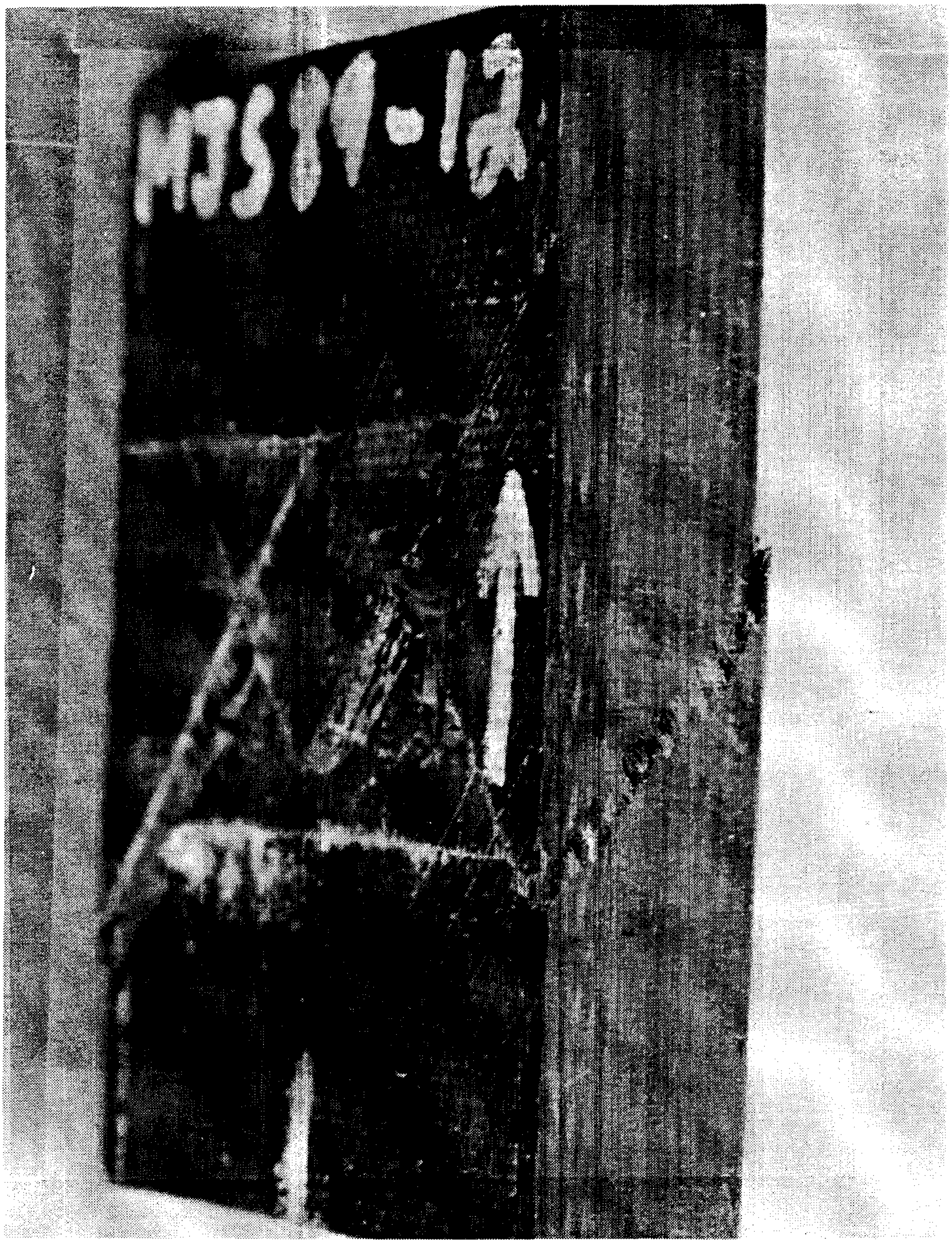

Figure 2.31 Edge view of failed 45° angle-ply specimen.

Figure 2.32 Edge view of failed 60° angle-ply specimen.

appears to be close to 45°. In figure 2.33 the typical matrix compression failure for the 75° to 90° range is shown. The failure surfaces indicate classical though somewhat brittle compressive failure. The failure surface for the 90° specimen is parallel to the fibers and begins at 45° to the laminate surface.

2.2.5 Laminate Imperfections

Several large pieces of scrap material were left over from each 6 in. by 7 in. panel after the specimens were cut. Edges of representative pieces of scrap were polished and inspected under a microscope to determine if any out-of-plane waviness could be found. Waviness measurable by the naked eye was observed in the 0° and 20° laminates. The waviness appeared to have been caused by a rough weave of bleeder cloth placed next to one surface of the laminates. The waviness seemed to disappear after approximately 8 plies and was not apparent through the remainder of the thickness of the specimens that were examined. The maximum amplitudes for these imperfections were between 0.2 and 0.5 ply thicknesses. Maximum imperfection half-wavelengths were between 9 and 17 ply thicknesses. Other smaller lamina irregularities in all of the specimens, and a void in one of the specimens was also observed. These lamina irregularities included matrix-rich and matrix-starved regions between layers, misplaced fibers, and broken fibers. Although measurable waviness was not found in every specimen, it was observed that some type of imperfection exists in each specimen and that these imperfections may vary from specimen to specimen, even when cut from the same panel. Additionally, an indication of fiber or ply misalignment is found in Table 2.1. Six 45° specimens were tested. All of these were cut from the same panel. However three specimens were cut at 90° to the other three.The first three 45° specimens in Table 2.1 resulted in consistently higher values for Young's modulus than the second

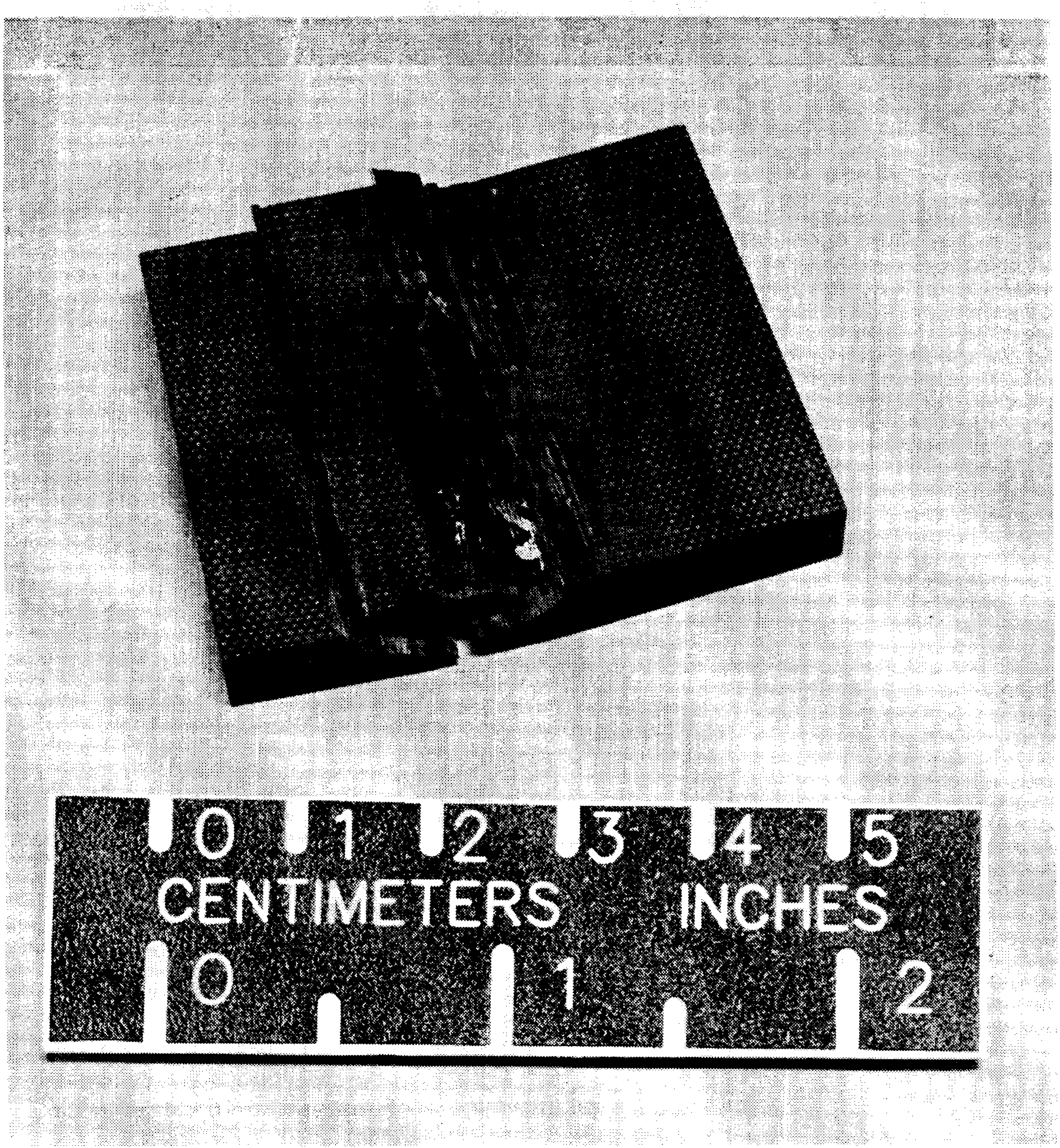

Figure 2.33 Failed $[90]_{48}$ specimen with transverse compression failure.

group of three. This indicates that the panel might not actually be a true $[(\pm 45)/(\mp 45)]_{6s}$ laminate, but rather the ply angles deviate from 45° by a small but noticeable amount.

2.3 Comparison With AS4/3502 Results

A comparison of IM7/8551-7a with AS4/3502 is useful, and also illustrative of the similar failure modes. In figures 2.34 and 2.35 the compression strengths of both AS4/3502 and IM7/8551-7a are plotted as a function of off-axis angle. Figure 2.34 indicates average IM7/8551-7a test values in solid dots and the average AS4/3502 values in open squares. Figure 2.35 illustrates actual test values for both material systems. The IM7/8551-7a material does not have it's lowest strength near 45°, as the AS4/3502 material does. Another intriguing point is that nearly the same strengths were obtained for IM7/8551-7a for 0° to 10°, as opposed to the decrease in strength of AS4/3502 for the same angles. Two reasons for this difference are proposed. One explanation considers the particular combination of matrix and fiber properties and fiber geometry in the IM7/8551-7a material system as affecting the stability of the fibers at low off-axis angle laminates. Another explanation is that initial imperfections have relatively greater impact on IM7/8551-7a than on AS4/3502. Both explanations are probably a factor, however the analysis in the ensuing chapters will prove enlightening when initial imperfections are considered. Failure modes for the IM7/8551-7a deduced from the experimental work are quite similar to those discussed in reference 22 for AS4/3502.

2.4 Failure Predictions Based on Classical Theory and the Maximum Stress Failure Criterion

As mentioned earlier, one of the objectives of the present work is to develop more ac-

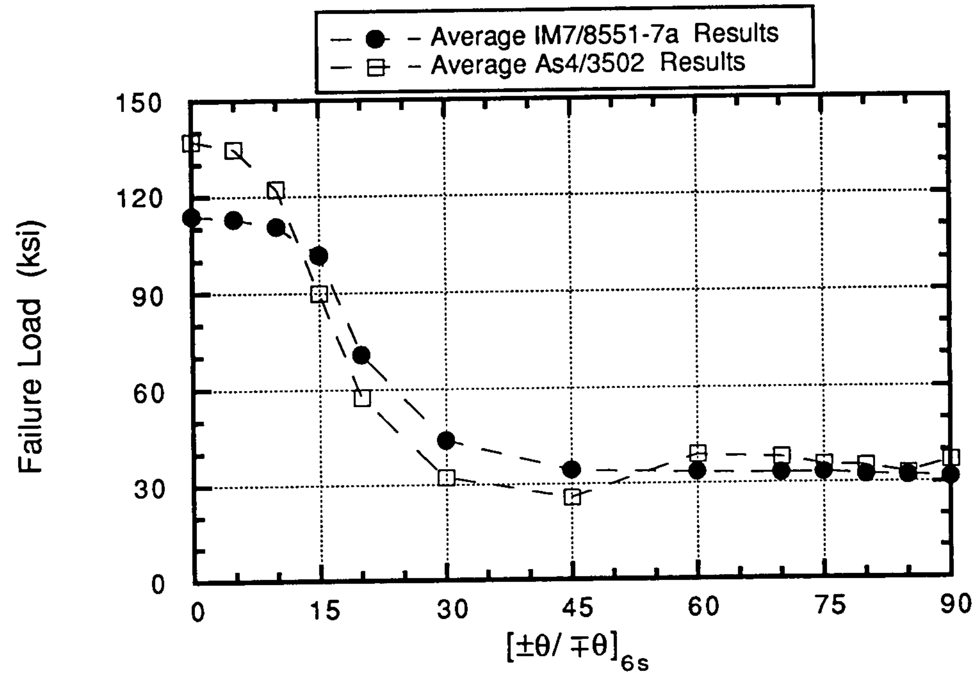

Figure 2.34 Average IM7/8551-7a and AS4/3502 compression test values.

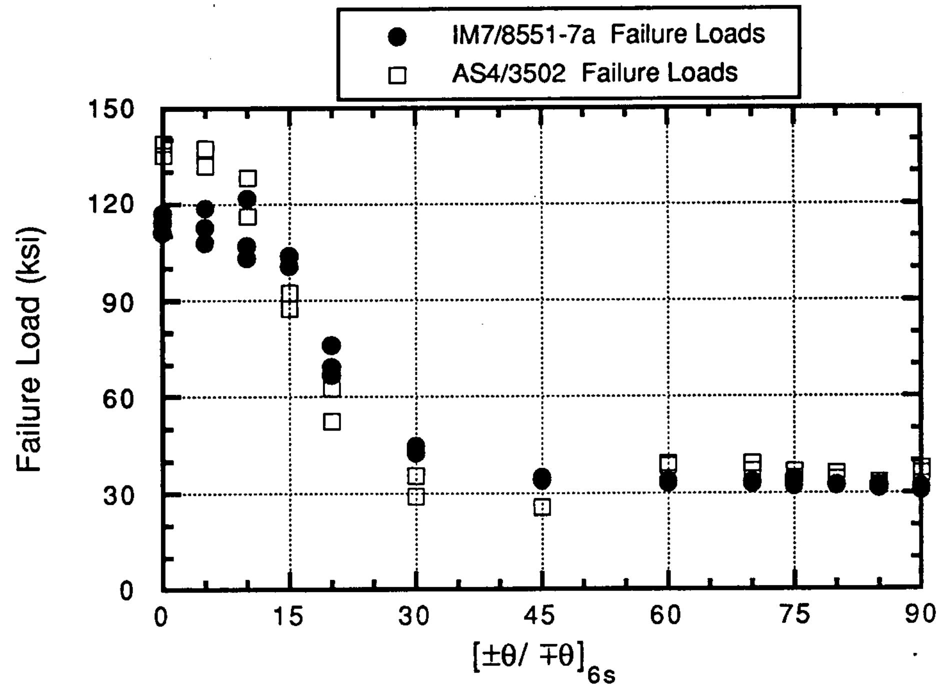

Figure 2.35 Actual IM7/8551-7a and AS4/3502 compression test values.

curate methods for predicting the compressive strength of composites. The simplest form of analysis of composites in compression is the use of classical lamination theory.[25,26] Elastic properties needed for such an analysis can be obtained from the experimental results. The shear modulus G_{12} can be calculated from the 45° specimens by a method derived by Rosen.[27] The two Young's moduli and Poisson's ratio can be determined directly from the 0° and 90° specimens. Elastic material properties for IM7/8551-7a as determined from the data in Table 2.1 are given in Table 2.2. Because of discrepancies in the transverse strain gage data, a published value was used for Poisson's ratio. The strengths are also given. They will be discussed next.

Table 2.2 IM7/8551-7a Elastic Properties and Strengths

Compression Elastic Properties			Strengths		
E_{11}	(Msi)	21.0*	$S_1{}^c$	(ksi)	240.0[28]
E_{22}	(Msi)	1.28*	$S_2{}^c$	(ksi)	31.4*
G_{12}	(Msi)	0.707*	$S_2{}^t$	(ksi)	7.70[28]
ν_{12}		0.360[28]	S_{12}	(ksi)	17.2*

* from present experiments

2.4.1 Failure Predictions

Using the experimentally-derived elastic properties, the maximum stress failure criterion can be used to predict the failure loads obtained. In order to do this, strengths for the IM7/8551-7a material system at the proper fiber volume fraction are needed. It can be assumed that for angle-ply laminates with angles greater than about 40° the laminates are not imperfection-sensitive, nor will the fixture used influence the results. Accordingly, shear and 90° compression strengths are obtained directly from the present experiments. However, for a failure analysis the compression strength for a 'perfect' 0° specimen is needed. For lack of a better number the strength given by Hercules is used.[28] From the observations of failure it was determined that the laminates might also fail due to transverse tension. Accordingly, this strength is also obtained from the Hercules report.[28] These four key strengths are given in Table 2.2, the superscript 'c' denoting compressive failure strength and the 't' denoting tensile failure strength. The comparison between experimental results and the maximum stress criterion used with classical lamination theory are displayed in figure 2.36. The various modes as predicted by the maximum stress failure criterion are indicated by the solid triangles, squares, and diamonds, whereas the solid circles represent experimental data. The solid squares for $\theta < 45^\circ$ represent inplane transverse tensile failure, whereas for $\theta > 45^\circ$ the solid squares represent inplane transverse compression failure. Obviously, as these angles are used to compute failure strengths, there is perfect correlation at 45° and 90°. However there are significant discrepancies for $\theta < 45^\circ$. For $0 \leq \theta \leq 10^\circ$ or 15° there are large differences between the experiment and the predicted fiber compression mode, the portion of the prediction given by the triangles. For $15^\circ \leq \theta \leq 30^\circ$ the inplane transverse tensile failure mode, the portion of the prediction given by the squares, does not match experimental data. For $\theta > 45^\circ$ correlation between the predictions and the experiments are good. However, in order to be useful as a design tool over the entire range of θ, classical lamination theory using the maximum stress failure criterion should predict the same or slightly lower failure stresses compared to those obtained experimentally. Unfortunately the maximum stress failure criterion using classical theory does not give accurate predictions for the fiber compression failure mode and the transverse tension failure mode. In the following section suggestions are given as to why classical lamination theory, used in conjunction with the maximum stress failure criterion is not completely accurate.

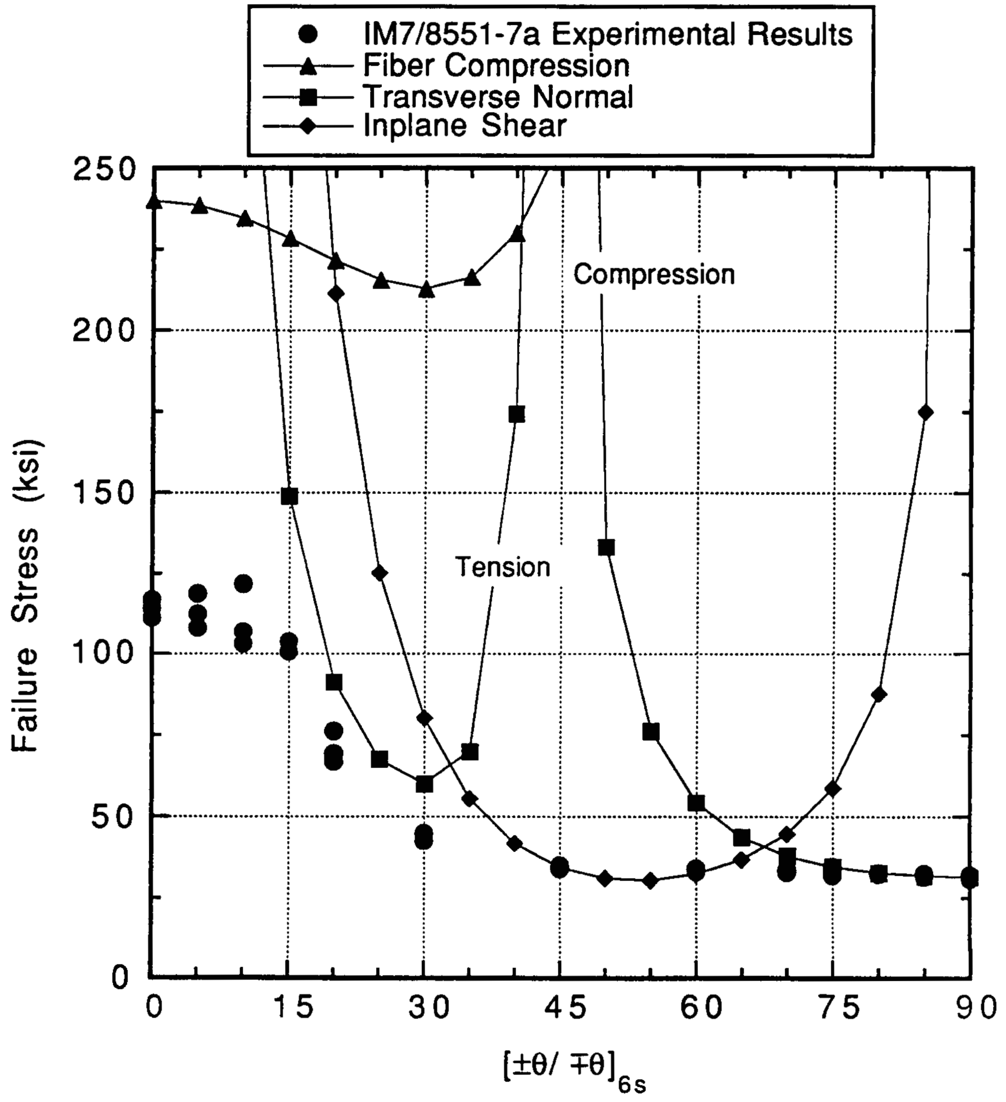

Figure 2.36 Comparison between experimental results and classical predictions using the maximum stress failure criterion.

2.4.2 Possible Reasons Why The Classical Model Doesn't Work

Before possible reasons as to why the classical model doesn't work are suggested, it is important to point out that here the emphasis is on predicting the mechanisms that affect laminate failure, as well as predicting the magnitudes of the failure stresses. With that in mind, some of the deficiencies in the classical model include:

a. *Interlaminar effects*: Classical lamination theory assumes thin plate theory, that is, there are no significant interlaminar stresses. The test specimens are bordering on what could be called 'thick composites.' Thin-plate theory may not be totally valid. Figure 2.30, with its out-of-plane delamination of the outer plies, for example, indicates there may be significant through-the-thickness stresses. For low off-axis angle laminates Shuart[21,22] indicates the primary failure mode of the AS4/3502 specimens to be interlaminar shear. That mode may be a factor with IM7/8551-7a too.

b. *Fixture-induced effects*: It has been suggested that due to the highly unstable nature of 0° laminates (you can't push with a rope theory), it is extremely difficult to obtain accurate strengths for low off-axis angle laminates. An appropriate fixture must hold the specimen securely and correctly, yet not impede valid failure modes. It is possible there is some degradation of strength of the very low off-axis angle specimens ($\theta < 10°$) because the fixture does not adequately allow the specimen to expand in the thickness direction. This fixture restraint causes stress concentrations at the ends of the specimens where they are held in place.

c. *Buckling of initially flat layers:* Rosen[1], in that classic derivation, and others have suggested that a predominate laminate compressive failure mode is microbuckling of initially flat layers. However, the critical buckling strengths are considerably higher than the published 0° compression strengths given by Hercules. There is no doubt, though, that fiber or ply instability plays an important role in the compressive failure of composites. This effect is not accounted for in the classical theory.

d. *Initial imperfections*: It is likely that the initial imperfections in a laminate are a large source of strength degradation for angle-ply laminates for $\theta < 45^\circ$. Imperfections can trigger or amplify the effects of short-wavelength (ply-level) instability. In the present work the specimens with $\theta \leq 20^\circ$ showed evidence of large waviness. As shown in figure 2.36, it is within this range of θ that the greatest difference between the predictions from the classical theory and experimental results occurs. It is well known in the buckling analysis of isotropic columns that an eccentricity or initial waviness can significantly effect the strength and out-of-plane deflection of such a column. Likewise, fiber eccentricities, initial ply waviness, or other imperfections that act like ply waviness can have significant impact on the compressive strength of a laminate. These influences are not accounted for in the classical theory.

The remainder of the present work will focus on resolving the discrepancies between the experimental results and the predictions of the classical theory. Attention will be on the influence of initial imperfections. The imperfections will be in the form of a wavy layer. This type of imperfection can aggravate the inplane stresses, e.g., fiber direction compression, and also produce interlaminar effects. Hence the wavy layer type imperfection should be considered as a serious candidate for contributing to the degradation of compression strength. The next two chapters will discuss the linear and nonlinear theories that will be used in the analysis of laminates with wavy layers.

2.5 Summary of Conclusions

Experimental results for angle-ply laminates made of the IM7/8551-7a material system have been discussed. When experimental results were compared to the published 0° compression strength, and other appropriate strengths, using classical lamination theory and the maximum stress failure criterion, there was found to be discrepancies between predictions and actual values for off-axis angles less than 45°, especially for $\theta < 25°$. Several reasons were cited for these discrepancies.

3.0 OVERVIEW OF PREVIOUSLY DEVELOPED THEORY

The theory discussed in this chapter was developed in detail in reference 21. The purpose of this chapter is to acquaint the reader with a basic understanding of the theory so that extensions and modifications of the theory can be put into context, and so that results based on the theory can be understood properly. The kinematics of deformation, the boundary conditions, and loading of the model are discussed briefly here. For a complete description of the theory the reader is referred to reference 21.

3.1 Description of Model

The physical model for this analysis is a series of laminated plates connected through elastic foundations. This model was alluded to in the introductory chapter. A representation of this model is found in figure 3.1. The basic element for the analysis consists of an idealized lamina, as seen in the exploded view of figure 3.1. Each lamina, layer, or ply consists of a plate, representing the fibers and referred to as a 'fiber-plate', and an elastic foundation, representative of the matrix and referred to as a 'matrix-foundation'. The layer has a total thickness t, the fiber plate has thickness t_f and the matrix-foundation has thickness t_m. These quantities are related through

$$t_f = V_f t \tag{3.1}$$

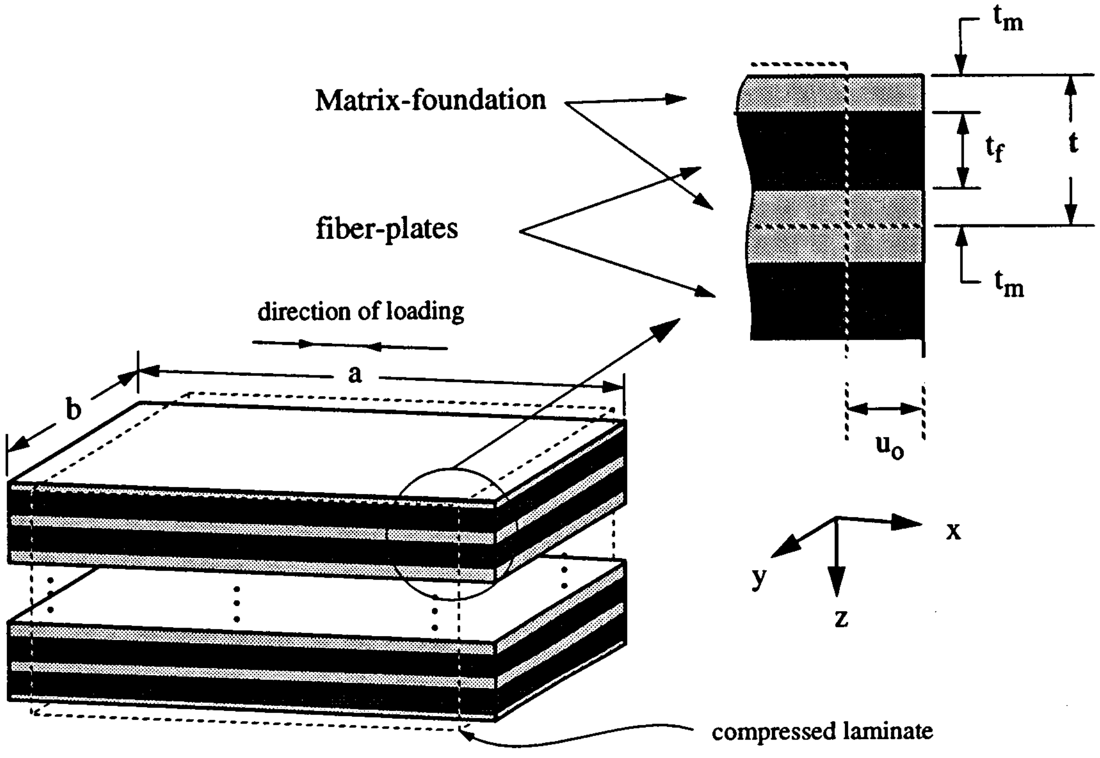

Figure 3.1 Representation of model used in analysis.

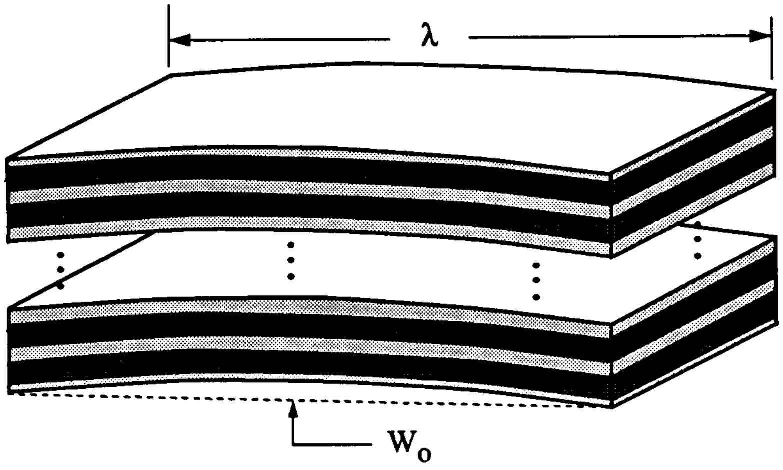

Figure 3.2 Model with wavy layers.

$$t_m = \frac{1}{2}(1 - V_f)\,t, \tag{3.2}$$

where V_f is the fiber volume fraction of the laminate. Combining equations 3.1 and 3.2 give

$$t = t_f + 2t_m \tag{3.3}$$

By combining the basic elements or layers, the model of the laminate is formed. The effects of the matrix-foundation on the outside of the outer-most layers are neglected. A maximum of eight layers can be considered. The compression loading is assumed to be in the x direction. The array of plates is of length ‘a’ in the x direction and width ‘b’ in the y direction. The origin of the coordinate system is placed at one corner of the plate in the x and y direction and at the midplane of the laminate in the z direction.

According to calculations in reference 21 (see figure 3.1 in that reference), the results of a buckling analysis with a limited number of layers asymptotically approaches the computed buckling solution for a laminate with many layers as the number of layers analyzed increases. When size and computational constraints were taken into account, eight layers was considered to give reasonable accuracy.

The basic model of the laminate includes initial imperfections in the form of wavy layers. Each layer in the model has the same imperfection. Originally in reference 21 only initial imperfections of the length of the critical buckling half-wavelength and an amplitude of one-half a ply thickness were considered. In the present work additional wavelengths and amplitudes are considered. The additional wavelengths and amplitudes will be discussed in chapter 5. An illustration of ply waviness or imperfection is found in figure 3.2. The quantity W_0 defines the amplitude of the initial out-of-plane waviness.

3.2 Nonlinear Governing Equations

Given linear elastic properties, the total potential energy for the parallel array of fiber-plates and matrix-foundations is obtained. From the resulting expression the governing nonlinear equilibrium equations for the model can be derived. The equations are nonlinear due to the inclusion of geometric nonlinearities. Here these equations are derived using the principle of stationary total potential energy and variational calculus. The governing nonlinear partial differential equations are:

for i = 1,2,.....N (where i is the layer number)

$$\frac{\partial N_x^{(i)}}{\partial x} + \frac{\partial N_{xy}^{(i)}}{\partial y} = 0 \qquad (3.4)$$

$$\frac{\partial N_{xy}^{(i)}}{\partial x} + \frac{\partial N_y^{(i)}}{\partial y} = 0. \qquad (3.5)$$

In terms of displacements:

for i = 1

$$D^{(1)}\,[w_1^{(1)}] - N_x^{(1)}\left(\frac{\partial^2 w_1^{(1)}}{\partial x^2} + \frac{\partial^2 w_o^{(1)}}{\partial x^2}\right) -$$

$$N_y^{(1)}\left(\frac{\partial^2 w_1^{(1)}}{\partial y^2} + \frac{\partial^2 w_o^{(1)}}{\partial y^2}\right) - 2N_{xy}^{(1)}\left(\frac{\partial^2 w_1^{(1)}}{\partial x \partial y} + \frac{\partial^2 w_o^{(1)}}{\partial x \partial y}\right) +$$

$$E^{\alpha}\,(w_1^{(1)} - w_1^{(2)}) - G^{\alpha}\left(\frac{\partial^2 w_1^{(1)}}{\partial y^2} + \frac{\partial^2 w_1^{(1)}}{\partial x^2}\right) -$$

$$G^{\beta}\left(\frac{\partial^2 w_1^{(2)}}{\partial y^2} + \frac{\partial^2 w_1^{(2)}}{\partial x^2}\right) = 0, \qquad (3.6)$$

for i = 2,3, ..., N-1

$$D^{(i)}\,[w_1^{(i)}] - N_x{}^{(i)}\left(\frac{\partial^2 w_1^{(i)}}{\partial x^2} + \frac{\partial^2 w_o^{(i)}}{\partial x^2}\right) -$$

$$N_y^{(i)}\left(\frac{\partial^2 w_1^{(i)}}{\partial y^2} + \frac{\partial^2 w_o^{(i)}}{\partial y^2}\right) - 2N_{xy}^{(i)}\left(\frac{\partial^2 w_1^{(i)}}{\partial x \partial y} + \frac{\partial^2 w_o^{(i)}}{\partial x \partial y}\right) +$$

$$E^{\alpha}\,(2w_1^{(i)} - w_1^{(i-1)} - w_1^{(i+1)}) - 2G^{\alpha}\left(\frac{\partial^2 w_1^{(i)}}{\partial y^2} + \frac{\partial^2 w_1^{(i)}}{\partial x^2}\right) -$$

$$G^{\beta}\left(\frac{\partial^2 w_1^{(i-1)}}{\partial y^2} + \frac{\partial^2 w_1^{(i-1)}}{\partial x^2} + \frac{\partial^2 w_1^{(i+1)}}{\partial y^2} + \frac{\partial^2 w_1^{(i+1)}}{\partial x^2}\right) = 0; \qquad (3.7)$$

for i = N

$$D^{(N)}\,[w_1^{(N)}] - N_x{}^{(N)}\left(\frac{\partial^2 w_1^{(N)}}{\partial x^2} + \frac{\partial^2 w_o^{(N)}}{\partial x^2}\right) -$$

$$V_y^{(1)}\left(\frac{\partial^2 w_1^{(N)}}{\partial y^2} + \frac{\partial^2 w_o^{(N)}}{\partial y^2}\right) - 2N_{xy}^{(N)}\left(\frac{\partial^2 w_1^{(N)}}{\partial x \partial y} + \frac{\partial^2 w_o^{(N)}}{\partial x \partial y}\right) +$$

$$E^{\alpha}\,(w_1^{(N)} - w_1^{(N-1)}) - G^{\alpha}\left(\frac{\partial^2 w_1^{(N)}}{\partial y^2} + \frac{\partial^2 w_1^{(N)}}{\partial x^2}\right) -$$

$$G^{\beta}\left(\frac{\partial^2 w_1^{(N)}}{\partial y^2} + \frac{\partial^2 w_1^{(N)}}{\partial x^2}\right) = 0. \qquad (3.8)$$

The equations for the boundary condition integrals are obtained from the energy formulation. The equations for the boundary conditions are taken from the boundary condition integrals and are:

for i = 1, 2, ... N

$$N_x^{(i)}\,\delta u^{\circ\,(i)}\Big|_0^a = 0 \qquad\qquad N_{xy}^{(i)}\,\delta u^{\circ\,(i)}\Big|_0^b = 0$$

$$N_y^{(i)}\,\delta v^{\circ(i)}\Big|_0^b = 0 \qquad\qquad N_{xy}^{(i)}\,\delta v^{\circ(i)}\Big|_0^a = 0$$

$$M_x^{(i)}\frac{\partial}{\partial x}(\delta w_1^{(i)})\Big|_0^a = 0 \qquad\qquad M_y^{(i)}\frac{\partial}{\partial y}(\delta w_1^{(i)})\Big|_0^b = 0$$

$$2M_{xy}^{(i)}\,\delta w_1^{(i)}\Big|_0^a\Big|_0^b = 0; \tag{3.9}$$

for i = 1

$$\left[\frac{\partial M_x^{(1)}}{\partial x} + 2\frac{\partial}{\partial y}(M_{xy}^{(1)}) + N_x^{(1)}\left(\frac{\partial w_1^{(1)}}{\partial x} + \frac{\partial w_o^{(1)}}{\partial x}\right) + \right.$$

$$\left. N_{xy}^{(1)}\left(\frac{\partial w_1^{(1)}}{\partial y} + \frac{\partial w_o^{(1)}}{\partial y}\right) + G^{\alpha}\frac{\partial w_1^{(1)}}{\partial x} + G^{\beta}\frac{\partial w_1^{(2)}}{\partial x}\right]\delta w_1^{(1)}\Big|_0^a = 0$$

$$\left[\frac{\partial M_y^{(1)}}{\partial y} + 2\frac{\partial}{\partial x}(M_{xy}^{(1)}) + N_y^{(1)}\left(\frac{\partial w_1^{(1)}}{\partial y} + \frac{\partial w_o^{(1)}}{\partial y}\right) + \right.$$

$$\left. N_{xy}^{(1)}\left(\frac{\partial w_1^{(1)}}{\partial x} + \frac{\partial w_o^{(1)}}{\partial x}\right) + G^{\alpha}\frac{\partial w_1^{(1)}}{\partial y} + G^{\beta}\frac{\partial w_1^{(2)}}{\partial y}\right]\delta w_1^{(1)}\Big|_0^b = 0; \tag{3.10}$$

for i = 2, 3, ..., N-1

$$\left[\frac{\partial M_x^{(i)}}{\partial x} + 2\frac{\partial}{\partial y}(M_{xy}^{(i)}) + N_x^{(i)}\left(\frac{\partial w_1^{(i)}}{\partial x} + \frac{\partial w_o^{(i)}}{\partial x}\right) + N_{xy}^{(i)}\left(\frac{\partial w_1^{(i)}}{\partial y} + \frac{\partial w_o^{(i)}}{\partial y}\right) + \right.$$

$$\left. 2G^{\alpha}\frac{\partial w_1^{(i)}}{\partial x} + G^{\beta}\left(\frac{\partial w_1^{(i+1)}}{\partial x} + \frac{\partial w_1^{(i-1)}}{\partial x}\right)\right]\delta w_1^{(1)}\Big|_0^a = 0$$

$$\left[\frac{\partial M_y^{(i)}}{\partial y} + 2\frac{\partial}{\partial x}(M_{xy}^{(i)}) + N_y^{(i)}\left(\frac{\partial w_1^{(i)}}{\partial y} + \frac{\partial w_o^{(i)}}{\partial y}\right) + N_{xy}^{(i)}\left(\frac{\partial w_1^{(i)}}{\partial x} + \frac{\partial w_o^{(i)}}{\partial x}\right) + \right.$$

$$\left. 2G^{\alpha}\frac{\partial w_1^{(i)}}{\partial y} + G^{\beta}\left(\frac{\partial w_1^{(i+1)}}{\partial y} + \frac{\partial w_1^{(i-1)}}{\partial y}\right)\right]\delta w_1^{(1)}\Big|_0^b = 0; \tag{3.11}$$

for i = N

$$\left[\frac{\partial M_x^{(N)}}{\partial x} + 2\frac{\partial}{\partial y}(M_{xy}^{(N)}) + N_x^{(N)}\left(\frac{\partial w_1^{(N)}}{\partial x} + \frac{\partial w_o^{(N)}}{\partial x}\right) + \right.$$

$$\left. N_{xy}^{(N)}\left(\frac{\partial w_1^{(N)}}{\partial y} + \frac{\partial w_o^{(N)}}{\partial y}\right) + G^{\alpha}\frac{\partial w_1^{(N)}}{\partial x} + G^{\beta}\frac{\partial w_1^{(N-1)}}{\partial x}\right]\delta w_1^{(N)}\Big|_0^a = 0$$

$$\left[\frac{\partial M_y^{(N)}}{\partial y} + 2\frac{\partial}{\partial x}(M_{xy}^{(N)}) + N_y^{(N)}\left(\frac{\partial w_1^{(N)}}{\partial y} + \frac{\partial w_o^{(N)}}{\partial y}\right) + \right.$$

$$\left. N_{xy}^{(N)}\left(\frac{\partial w_1^{(N)}}{\partial x} + \frac{\partial w_o^{(N)}}{\partial x}\right) + G^{\alpha}\frac{\partial w_1^{(N)}}{\partial y} + G^{\beta}\frac{\partial w_1^{(N-1)}}{\partial y}\right]\delta w_1^{(N)}\Big|_0^b = 0. \qquad (3.12)$$

3.2.1 Definition of Terms in Previous Equations

For some of the terms defined a complete description will be given. For other terms only a brief description will be given since it will be assumed the reader is familiar with them. For further details the reader should consult a text on classical lamination theory.[25,26]

$D^{(i)}[*]$ is an operator defined by

$$D^{(i)}[w] = D_{11}^{(i)}\frac{\partial^4 w}{\partial x^4} + 2\left(D_{12}^{(i)} + 2D_{66}^{(i)}\right)\frac{\partial^4 w}{\partial x^2 \partial y^2} +$$

$$D_{22}^{(i)}\frac{\partial^4 w}{\partial y^4} + 4D_{16}^{(i)}\frac{\partial^4 w}{\partial x^3 \partial y} + 4D_{26}^{(i)}\frac{\partial^4 w}{\partial x \partial y^3}, \qquad (3.13)$$

and the constants are defined by

$$E^{\alpha} = \frac{E_m}{2t_m(1-\upsilon_m^2)}$$

$$G^{\alpha} = \frac{G_m}{4t_m}\left(\frac{t_f^2}{2} + 2t_f t_m + \frac{8t_m^2}{3}\right)$$

$$G^{\beta} = \frac{G_m}{4t_m}\left(\frac{t_f^2}{2} + 2t_f t_m + \frac{4t_m^2}{3}\right). \qquad (3.14)$$

The quantities N_x, N_y, and N_{xy} are inplane stress resultants. The definitions for them are the standard. Likewise with the D_{ij}, which are fiber-plate bending stiffnesses.

The i-th fiber-plate has displacements $u^{(i)}$, $v^{(i)}$, and $w^{(i)}$ in the x, y, and z directions, respectively. The theory for the fiber-plates is derived using the Kirchhoff assumptions. The expressions for the fiber-plate displacements are

$$u^{(i)}(x, y, \bar{z}) = u^{\circ(i)}(x, y) - \bar{z}\frac{\partial}{\partial x}w^{\circ(i)}(x, y), \tag{3.15}$$

$$v^{(i)}(x, y, \bar{z}) = v^{\circ(i)}(x, y) - \bar{z}\frac{\partial}{\partial y}w^{\circ(i)}(x, y), \tag{3.16}$$

$$w^{(i)}(x, y, \bar{z}) = w_o^{(i)}(x, y) + w_1^{(i)}(x, y) = w^{\circ(i)}(x, y), \tag{3.17}$$

where $u^{\circ(i)}$, $v^{\circ(i)}$, and $w^{\circ(i)}$ are displacements in the x, y, and z directions, respectively, of the midplane of the i-th fiber-plate.The local through-the-thickness coordinate, $\bar{z}$, is defined such that

$$\frac{-t_f}{2} \leq \bar{z} \leq \frac{t_t}{2}. \tag{3.18}$$

The $w^{\circ(i)}$ displacement contains the contributions of the imperfection of the fiber-plate $w_o^{(i)}$ and the additional displacement due to loading, $w_1^{(i)}$. The expressions for the normal and shear strains in the i-th fiber-plate are

$$\varepsilon_x^{(i)} = \varepsilon_x^{\circ(i)} + \bar{z}\kappa_x^{\circ(i)},$$

$$\varepsilon_y^{(i)} = \varepsilon_y^{\circ(i)} + \bar{z}\kappa_y^{\circ(i)},$$

$$\gamma_{xy}^{(i)} = \gamma_{xy}^{\circ(i)} + \bar{z}\kappa_{xy}^{\circ(i)} . \tag{3.19}$$

Where $\varepsilon_x^{\circ(i)}$, $\varepsilon_y^{\circ(i)}$, and $\gamma_{xy}^{\circ(i)}$ are the normal and shearing strains for the midplane of the i-th fiber-plate and $\kappa_x^{\circ(i)}$, $\kappa_y^{\circ(i)}$, and $\kappa_{xy}^{\circ(i)}$ are the curvatures of the i-th fiber-plate. The midplane strains are developed using the von Karman nonlinear strain-displacement relations and include the initial imperfections of the fiber-plate. These strain-displacement relations assume that strains are small, that rotations about to the x and y axes are moderately small, and that rotations about to the $\bar{z}$ axis are negligible. Accordingly, the strain-displacement relations for the i-th fiber-plate are

$$\begin{aligned}
\varepsilon_x^{\circ(i)} &= \frac{\partial u^{\circ(i)}}{\partial x} + \frac{1}{2}\left(\frac{\partial w_1^{\circ(i)}}{\partial x}\right)^2 + \frac{\partial w_o^{\circ(i)}}{\partial x}\frac{\partial w_1^{\circ(i)}}{\partial x} , \\
\varepsilon_y^{\circ(i)} &= \frac{\partial v^{\circ(i)}}{\partial y} + \frac{1}{2}\left(\frac{\partial w_1^{\circ(i)}}{\partial y}\right)^2 + \frac{\partial w_o^{\circ(i)}}{\partial y}\frac{\partial w_1^{\circ(i)}}{\partial y} , \\
\gamma_{xy}^{\circ(i)} &= \frac{\partial u^{\circ(i)}}{\partial y} + \frac{\partial v^{\circ(i)}}{\partial x} + \frac{\partial w_1^{\circ(i)}}{\partial x}\frac{\partial w_1^{\circ(i)}}{\partial y} + \\
&\frac{\partial w_o^{\circ(i)}}{\partial x}\frac{\partial w_1^{\circ(i)}}{\partial y} + \frac{\partial w_o^{\circ(i)}}{\partial y}\frac{\partial w_1^{\circ(i)}}{\partial x} .
\end{aligned} \tag{3.20}$$

The normal and shearing strains are zero when the fiber-plate is unloaded. The curvatures are defined by

$$\begin{aligned}
\kappa_x^{\circ(i)} &= -\frac{\partial^2 w_1^{(i)}}{\partial x^2} \\
\kappa_y^{\circ(i)} &= -\frac{\partial^2 w_1^{(i)}}{\partial y^2} \\
\kappa_{xy}^{\circ(i)} &= -\frac{\partial^2 w_1^{(i)}}{\partial x \partial y} .
\end{aligned} \tag{3.21}$$

The initial imperfections do not appear in the definition of the curvatures since the curvatures are determined by the change in slope of the midplane from the initial midplane geometry.

The matrix-foundations elastically connect the fiber-plates. The i-th matrix-foundation is located between the i-th and the (i+1)-st fiber-plates and has displacement $u_m^{(i)}$, $v_m^{(i)}$, and $w_m^{(i)}$ in the x, y, and z directions, respectively. The through-the-thickness coordinate of the matrix-foundation $\tilde{z}$ is defined such that

$$-t_m \le \tilde{z} \le t_m. \tag{3.22}$$

The displacements of the i-th matrix-foundation are linear functions of the displacements of the adjacent fiber-plates and are defined by

$$\begin{aligned}
u_m^{(i)} &= u^{\circ(i)} + \frac{t_f}{4t_m}\left[(t_m+\tilde{z})\frac{\partial w_1}{\partial x}^{(i+1)} - (t_m-\tilde{z})\frac{\partial w_1}{\partial x}^{(i)} \right], \\
v_m^{(i)} &= v^{\circ(i)} + \frac{t_f}{4t_m}\left[(t_m+\tilde{z})\frac{\partial w_1}{\partial y}^{(i+1)} - (t_m-\tilde{z})\frac{\partial w_1}{\partial y}^{(i)} \right], \\
w_m^{(i)} &= \frac{t_f}{2t_m}\left[(t_m+\tilde{z})\, w_1{}^{(i+1)} + (t_m-\tilde{z})\, w_1{}^{(i)} \right].
\end{aligned} \tag{3.23}$$

The initial imperfections of the adjacent fiber-plates do not appear in equations (3.17). Deformation of the matrix-foundation is the result of displacements due to loading of adjacent fiber-plates. The matrix is assumed to be initially unstrained.

In this model the matrix-foundations have extensional stiffness in the z direction and shearing stiffness in the y-z and x-z planes. The out-of-plane strain-displacement relations for the i-th matrix-foundation are

$$\varepsilon_{mz}^{\circ(i)} = \frac{\partial w^{(i)}}{\partial \tilde{z}},$$

$$\gamma_{myz}^{\circ(i)} = \frac{\partial v_m^{(i)}}{\partial \tilde{z}} + \frac{\partial w_m^{(i)}}{\partial y},$$

$$\gamma_{mxz}^{\circ(i)} = \frac{\partial u_m^{(i)}}{\partial \tilde{z}} + \frac{\partial w_m^{(i)}}{\partial x}. \tag{3.24}$$

The matrix-foundation equations for the out-of-plane strains were derived using a shear-lag formulation.

3.2.2 Model Loading, Boundary Conditions, and Solution Procedure

The model is loaded in compression by assuming uniform end shortening. Because no external loads are applied to the model the potential energy of the applied loads is zero. The loading enters the theory as a u displacement boundary condition for each fiber-plate as

$$u^{\circ(i)}(0, y) = 0$$

$$u^{\circ(i)}(a, y) = -\bar{u}_o, \mathrm{i} = 1, 2, ..., \mathrm{N}. \tag{3.25}$$

The u and v displacement boundary conditions on the four boundaries are chosen to assure that the model remains rectangular during loading, as the test specimens are rectangular. The u and v boundary conditions for each fiber-plate are designated as

for i = 1, 2, ..., N

$u^{\circ(i)}(x, 0) = -\bar{u}_o\left(\frac{x}{a}\right)$, where $\bar{u}_0$ is a known constant,

$$u^{\circ(i)}(x, b) = u^{\circ(i)}(x, 0),$$

$$v^{\circ(i)}(0,y) = \left(\frac{A_{12}^T}{A_{22}^T}\right)(y-\frac{b}{2})\frac{\bar{u}_o}{a},$$

$$v^{\circ(i)}(a,y) = v^{\circ(i)}(0,y),$$

$$v^{\circ(i)}(x,0) = \left(-\frac{A_{12}^T}{A_{22}^T}\right)(\frac{b}{2})\frac{\bar{u}_o}{a},$$

$$v^{\circ(i)}(x,b) = -v^{\circ(i)}(x,0), \tag{3.26}$$

where A_{12}^T and A_{22}^T are extensional stiffnesses for the total laminate and are defined by

$$(A_{12}^T,\ A_{22}^T) = \sum_{i=1}^{N}(A_{12}^{(i)},\ A_{22}^{(i)}). \tag{3.27}$$

The $A_{jk}^{(i)}$ are extensional stiffnesses, or inplane moduli, for the i-th layer of the laminate. Their definition is the standard.[25,26] The v displacement boundary conditions are the result of Poisson expansion during loading.

The model is simply supported on the unloaded edges. These simple-support boundary conditions are indicated as

at y = 0 and y = b

$$w_1^{(i)} = 0 \qquad M_y^{(i)} = 0 \qquad i = 1, 2, ..., N. \tag{3.28}$$

It is assumed that when the model with initial imperfections is loaded in the x direction it deforms out-of-plane into a short-wavelength deflection mode. This mode may or may not be the critical short-wavelength buckling mode. It has been mentioned that both short wavelengths due to buckling and short wavelengths resulting from manufacturing anomalies will be considered. In either case, the half-wavelength is much smaller than the laminate's length or the laminate's width. Because the half-wavelength is so much smaller than the laminate dimensions the fiber-plates in the model behave as elastically supported semi-infinite strips for which the displacement and moment boundary conditions at x=0 and x=a to have negligible effect on the short-wavelength buckling behavior of the model. The displacement and moment boundary conditions for this model can be expressed along node lines of the mode shape as

<u>at $\bar{x} = 0$ and at $\bar{x} = \lambda$</u>

$$w_1^{(i)} = 0 \qquad M_x^{(i)} = 0 \qquad i = 1, 2, \ldots, N, \tag{3.29}$$

where the $\bar{x}$-axis is parallel to the x-axis and is the localized coordinate for $0 \le \bar{x} \le \lambda$. The analysis is thus confined to this region.

If the short wavelength used is the critical one, that wavelength must be determined from a linear buckling analysis. The linearized buckling analysis is discussed in the next section.

3.3 Linear Theory

The nonlinear governing equations were linearized to determine the laminate end shortening associated with short-wavelength buckling. This end shortening is the critical end shortening $(\bar{u}_o)_{cr}$. The linearized equations are also used to determine the critical buckling half-wavelength. The critical buckling half-wavelength is considered a laminate property. The linearized equations are derived using the adjacent-equilibrium criterion. Adjacent equilibrium configurations for the fiber-plates are investigated by adding small increments to the fiber-plate displacements. The relationships between the displacements prior to buckling, $u_a^{(i)}$, $v_a^{(i)}$, and $w_a^{(i)}$, and the displacements of an adjacent equilibrium configuration, $u^{(i)}$, $v^{(i)}$, and $w^{(i)}$, are expressed by

$$u^{(i)} = u_a^{(i)} + \varepsilon\bar{u}$$

$$v^{(i)} = v_a^{(i)} + \varepsilon\bar{v}$$

$$w_1^{(i)} = w_a^{(i)} + \varepsilon\bar{w}_1, \tag{3.30}$$

where the quantity ε is infinitesimally small. The prebuckling displacement $w_a^{(i)}$ and it's derivatives are zero for the flat i-th fiber-plate loaded by uniform end shortening. The fiber-plates do not include imperfections in the linear analysis ($w_o^{(i)} = 0$).

3.3.1 Linearized Governing Equations

The linear stability equations for the collection of fiber-plates are stated below. Please note that all quantities with an overbar, except $\bar{x}$, are the variational form of the same quantity without the bar. The equations are:

<u>for i = 1</u>

$$\bar{D}^{(1)}[\bar{w}_1^{(1)}] - N_{x^o}^{(1)}\frac{\partial^2\bar{w}_1^{(1)}}{\partial x^2} - N_{y^o}^{(1)}\frac{\partial^2\bar{w}_1^{(1)}}{\partial y^2} - 2N_{xy^o}^{(1)}\frac{\partial^2\bar{w}_1^{(1)}}{\partial x\partial y} +$$

$$E^{\alpha}(\bar{w}_1^{(1)} - \bar{w}_1^{(2)}) - G^{\alpha}\left(\frac{\partial^2\bar{w}_1^{(1)}}{\partial y^2} + \frac{\partial^2\bar{w}_1^{(1)}}{\partial x^2}\right) - G^{\beta}\left(\frac{\partial^2\bar{w}_1^{(2)}}{\partial y^2} + \frac{\partial^2\bar{w}_1^{(2)}}{\partial x^2}\right) = 0; \tag{3.31}$$

<u>for i = 2, 3, ..., N-1</u>

$$\bar{D}^{(i)}[\bar{w}_1^{(i)}] - N_{x^o}^{(i)}\frac{\partial^2\bar{w}_1^{(i)}}{\partial x^2} - N_{y^o}^{(i)}\frac{\partial^2\bar{w}_1^{(i)}}{\partial y^2} - 2N_{xy^o}^{(i)}\frac{\partial^2\bar{w}_1^{(i)}}{\partial x\partial y} +$$

$$E^{\alpha}(2\bar{w}_1^{(i)} - \bar{w}_1^{(i-1)} - \bar{w}_1^{(i+1)}) - 2G^{\alpha}\left(\frac{\partial^2\bar{w}_1^{(i)}}{\partial y^2} + \frac{\partial^2\bar{w}_1^{(i)}}{\partial x^2}\right) +$$

$$G^{\beta}\left(\frac{\partial^2\bar{w}_1^{(i-1)}}{\partial y^2} + \frac{\partial^2\bar{w}_1^{(i-1)}}{\partial x^2} + \frac{\partial^2\bar{w}_1^{(i+1)}}{\partial y^2} + \frac{\partial^2\bar{w}_1^{(i+1)}}{\partial x^2}\right) = 0; \qquad (3.32)$$

<u>for i = N</u>

$$\bar{D}^{(N)}[\bar{w}_1^{(N)}] - N_{x^o}^{(N)}\frac{\partial^2\bar{w}_1^{(N)}}{\partial x^2} - N_{y^o}^{(N)}\frac{\partial^2\bar{w}_1^{(N)}}{\partial y^2} - 2N_{xy^o}^{(N)}\frac{\partial^2\bar{w}_1^{(N)}}{\partial x\partial y} +$$

$$E^{\alpha}(\bar{w}_1^{(N)} - \bar{w}_1^{(N-1)}) - G^{\alpha}\left(\frac{\partial^2\bar{w}_1^{(N)}}{\partial y^2} + \frac{\partial^2\bar{w}_1^{(N)}}{\partial x^2}\right) -$$

$$G^{\beta}\left(\frac{\partial^2\bar{w}_1^{(N-1)}}{\partial y^2} + \frac{\partial^2\bar{w}_1^{(N-1)}}{\partial x^2}\right) = 0. \qquad (3.33)$$

3.3.2 Definition of Terms in Preceding Equations

The short-wavelength mode shape for an anisotropic fiber-plate can have half-waves that are oriented at an angle ϕ to the orientation of a normal wave. These half-waves are referred to as “skewed waves”. The form of the z displacement that satisfies the linear stability equations and boundary conditions for a model composed of anisotropic fiber plates is

$$\bar{w}_1^{(i)} = w_s^{(i)}(y)\sin\frac{\pi\bar{x}}{\lambda} + w_c^{(i)}(y)\cos\frac{\pi\bar{x}}{\lambda}. \qquad (3.34)$$

For orthotropic fiber-plates, the cosine term above goes to zero. Also, $A_{16}^{(i)}$, $A_{26}^{(i)}$, $D_{16}^{(i)}$, and $D_{26}^{(i)}$ go to zero. This simplifies previous and following equations considerably. The A_{jk}, and D_{jk} terms are defined in any text on classical lamination theory.[25,26]

The quantities $N_{x^o}^{(i)}$, $N_{y^o}^{(i)}$, and $N_{xy^o}^{(i)}$ are prebuckling stress resultants and are defined below as

$$N_{x^\circ}^{(i)} = A_{11}^{(i)}\frac{\partial u_a^{(i)}}{\partial x} + A_{12}^{(i)}\frac{\partial v_a^{(i)}}{\partial y} + A_{16}^{(i)}\left(\frac{\partial u_a^{(i)}}{\partial y} + \frac{\partial v_a^{(i)}}{\partial x}\right)$$

$$N_{y^\circ}^{(i)} = A_{12}^{(i)}\frac{\partial u_a^{(i)}}{\partial x} + A_{22}^{(i)}\frac{\partial v_a^{(i)}}{\partial y} + A_{26}^{(i)}\left(\frac{\partial u_a^{(i)}}{\partial y} + \frac{\partial v_a^{(i)}}{\partial x}\right)$$

$$N_{xy^\circ}^{(i)} = A_{16}^{(i)}\frac{\partial u_a^{(i)}}{\partial x} + A_{26}^{(i)}\frac{\partial v_a^{(i)}}{\partial y} + A_{66}^{(i)}\left(\frac{\partial u_a^{(i)}}{\partial y} + \frac{\partial v_a^{(i)}}{\partial x}\right). \tag{3.35}$$

3.3.3 Solution Procedure

The eigenvalues and eigenvectors for the assemblage of fiber-plates are obtained using the Galerkin method. The functions of y for the i-th fiber-plate, $w_s^{(i)}(y)$, and $w_c^{(i)}(y)$, are expanded into a Fourier sine series. These series satisfy the boundary conditions for $\bar{w}_1^{(i)}$ at y=0 and at y=b and are expressed as

$$w_s^{(i)}(y) = \sum_{m=1}^{M} \bar{w}_{sm}^{(i)} \sin\frac{m\pi y}{b}$$

$$w_c^{(i)}(y) = \sum_{n=1}^{M} \bar{w}_{cn}^{(i)} \sin\frac{n\pi y}{b}, \tag{3.36}$$

where M is the number of terms in the series and is an even number. Equations (3.34) and (3.36) are substituted into equations (3.31) to (3.33) and the series expansions for $w_s^{(i)}$ and $w_c^{(i)}$ are solutions to these equations if the equations are orthogonal to $\sin\frac{m\pi y}{b}$ and to $\sin\frac{n\pi y}{b}$ for each m and n, respectively. Therefore each equation is multiplied by $\sin\frac{m\pi y}{b}$ and $\sin\frac{n\pi y}{b}$. These resulting equations are then integrated to obtain 2*M simultaneous equations for each fiber-plate in terms of the 2*M undetermined coefficients $\bar{w}_{sm}^{(i)}$ and $\bar{w}_{cn}^{(i)}$. The series of simultaneous equations for N fiber-plates leads to an eigenvalue problem of order 2*M*N. For a given value of λ, this 2*M*N system has M*N unique eigenvalues. The eigenvalues represent values of $\bar{u}_o/a$. The critical value of $\bar{u}_o/a$, i.e.,

$(\bar{u}_o/a)_{cr}$, and the half-wavelength that goes with it, λ_{cr}, are determined by minimizing $(\bar{u}_o/a)_{cr}$ with respect to λ.

3.3.4 Computer Program for Linear Theory

The computer program written in conjunction with reference 21 to implement the linear buckling theory is called THESL and was implemented on a Control Data Corporation Cyber 205 vector processing computer. The program used eigensolving and minimizing subroutines developed at the NASA-Langley Research Center. More will be said about the computer program in the next chapter, including an example.

3.4 Nonlinear Theory

The governing nonlinear differential equations are used to obtain displacements, strains, loads, and stresses for a model containing initially imperfect fiber-plates. In the previous work the initial imperfections for all fiber-plates are the same and have the shape of the buckling mode for the model. The Kantorovich method and a numerical scheme are used to obtain solutions to the nonlinear equations. The unknown functions are expanded in kinematically admissible trigonometric series in the $\bar{x}$-coordinate, and this spatial variable is eliminated by integrating along the length of the laminate. The governing equations then become nonlinear coupled ordinary differential equations in the width-wise coordinate. These nonlinear ordinary differential equations are solved numerically. These steps are elaborated upon in the following sections.

3.4.1 Governing Equations

The kinematically admissible trigonometric series representing the displacements for the i-th fiber-plate are expressed as

$$u^{\circ(i)} = \frac{-\bar{u}_0 x}{a} + u_o^{(i)}(y) + u_s^{(i)}(y)\sin\frac{2\pi\bar{x}}{\lambda} + u_c^{(i)}(y)\cos\frac{2\pi\bar{x}}{\lambda}$$

$$v^{\circ(i)} = v_o^{(i)}(y) + v_s^{(i)}(y)\sin\frac{2\pi\bar{x}}{\lambda} + v_c^{(i)}(y)\cos\frac{2\pi\bar{x}}{\lambda}$$

$$w^{\circ(i)} = w_{\circ s}(y)\sin\frac{\pi\bar{x}}{\lambda} + w_{\circ c}(y)\cos\frac{\pi\bar{x}}{\lambda} + w_s^{(i)}(y)\sin\frac{\pi\bar{x}}{\lambda} + w_c^{(i)}(y)\cos\frac{\pi\bar{x}}{\lambda}, \qquad (3.37)$$

where the $w_{\circ s}$ and $w_{\circ c}$ terms contain the initial imperfection, or initial waviness.

Equations (3.37) are substituted into equations (3.20), and (3.21) to obtain kinematically admissible midplane strains and curvatures, and those results are substituted into the standard formulation for stress and moment resultants. The total potential energy is formulated, integration with respect to $\bar{x}$ is performed, the total potential energy minimized, and the following governing ordinary differential equations obtained:

for i = 1, 2, ..., N

$$\frac{dN_{\circ xy}^{(i)}}{dy} = 0;$$

$$\frac{2\pi}{\lambda}N_{xc}^{(i)} - \frac{dN_{xys}^{(i)}}{dy} = 0;$$

$$\frac{2\pi}{\lambda}N_{xs}^{(i)} - \frac{dN_{xyc}^{(i)}}{dy} = 0;$$

$$\frac{dN_{\circ y}^{(i)}}{dy} = 0;$$

$$\frac{2\pi}{\lambda}N_{xyc}^{(i)} - \frac{dN_{ys}^{(i)}}{dy} = 0;$$

$$\frac{2\pi}{\lambda}N_{xys}^{(i)} - \frac{dN_{yc}^{(i)}}{dy} = 0; \qquad (3.38)$$

for i = 1

$$\frac{dV_{ys}^{(1)}}{dy} = -\left(\frac{\pi}{\lambda}\right)^2 M_{xs}^{(1)} - \left(\frac{\pi}{\lambda}\right)^2 \left(N_{\circ x}^{(1)} + \frac{1}{2}N_{xc}^{(1)}\right)\left(w_s^{(1)} + w_{\circ s}\right) +$$

$$\frac{1}{2}\left(\frac{\pi}{\lambda}\right)^2 N_{xs}^{(1)}\left(w_c^{(1)} + w_{\circ c}\right) - \left(\frac{\pi}{\lambda}\right)\Big[\left(N_{\circ xy}^{(1)} + \frac{1}{2}N_{xyc}^{(1)}\right)\Big(\beta_s^{(1)} +$$

$$\frac{dw_{\circ c}}{dy}\Big) + \frac{1}{2}N_{xys}^{(1)}\left(\beta_s^{(1)} + \frac{dw_{\circ s}}{dy}\right)\Big] - G^{\alpha}\left[-\frac{d\beta_s^{(1)}}{dy} + \left(\frac{\pi}{\lambda}\right)^2 w_s^{(1)}\right] -$$

$$G^{\beta}\left[-\frac{d\beta_s^{(2)}}{dy} + \left(\frac{\pi}{\lambda}\right)^2 w_s^{(2)}\right] - E^{\alpha}\left(w_s^{(1)} - w_s^{(2)}\right); \qquad (3.39)$$

$$\frac{dV_{yc}^{(1)}}{dy} = -\left(\frac{\pi}{\lambda}\right)^2 M_{xc}^{(1)} - \left(\frac{\pi}{\lambda}\right)^2 \left(N_{\circ x}^{(1)} - \frac{1}{2}N_{xc}^{(1)}\right)\left(w_c^{(1)} + w_{\circ c}\right) +$$

$$\frac{1}{2}\left(\frac{\pi}{\lambda}\right)^2 N_{xs}^{(1)}\left(w_s^{(1)} + w_{\circ s}\right) + \left(\frac{\pi}{\lambda}\right)\Big[\left(N_{\circ xy}^{(1)} - \frac{1}{2}N_{xyc}^{(1)}\right)\Big(\beta_c^{(1)} +$$

$$\frac{dw_{\circ s}}{dy}\Big) + \frac{1}{2}N_{xys}^{(1)}\left(\beta_c^{(1)} + \frac{dw_{\circ c}}{dy}\right)\Big] - G^{\alpha}\left[-\frac{d\beta_c^{(1)}}{dy} + \left(\frac{\pi}{\lambda}\right)^2 w_c^{(1)}\right] -$$

$$G^{\beta}\left[-\frac{d\beta_c^{(2)}}{dy} + \left(\frac{\pi}{\lambda}\right)^2 w_c^{(2)}\right] - E^{\alpha}\left(w_c^{(1)} - w_c^{(2)}\right); \qquad (3.40)$$

for i = 2, 3, ..., N-1

$$\frac{dV_{ys}^{(i)}}{dy} = -\left(\frac{\pi}{\lambda}\right)^2 M_{xs}^{(i)} - \left(\frac{\pi}{\lambda}\right)^2 \left(N_{\circ x}^{(i)} + \frac{1}{2}N_{xc}^{(i)}\right)\left(w_s^{(i)} + w_{\circ s}\right) +$$

$$\frac{1}{2}\left(\frac{\pi}{\lambda}\right)^2 N_{xs}^{(i)}\left(w_c^{(i)} + w_{\circ c}\right) - \left(\frac{\pi}{\lambda}\right)\Big[\left(N_{\circ xy}^{(i)} + \frac{1}{2}N_{xyc}^{(i)}\right)\Big(\beta_s^{(i)} +$$

$$\frac{dw_{\circ c}}{dy}\Big) + \frac{1}{2}N_{xys}^{(i)}\left(\beta_s^{(i)} + \frac{dw_{\circ s}}{dy}\right)\Big] - 2G^{\alpha}\left[-\frac{d\beta_s^{(i)}}{dy} + \left(\frac{\pi}{\lambda}\right)^2 w_s^{(i)}\right] -$$

$$G^{\beta}\left[-\frac{d\beta_s^{(i-1)}}{dy} + \left(\frac{\pi}{\lambda}\right)^2 w_s^{(i-1)} - \frac{d\beta_s^{(i+1)}}{dy} + \left(\frac{\pi}{\lambda}\right)^2 w_s^{(i+1)}\right] -$$

$$E^{\alpha}(2w_s^{(i)} - w_s^{(i-1)} - w_s^{(i+1)}) ; \tag{3.41}$$

$$\frac{dV_{yc}^{(i)}}{dy} = -\left(\frac{\pi}{\lambda}\right)^2 M_{xc}^{(i)} - \left(\frac{\pi}{\lambda}\right)^2 (N_{\circ x}^{(i)} - \frac{1}{2}N_{xc}^{(i)})\,(w_c^{(i)} + w_{\circ c}) +$$

$$\frac{1}{2}\left(\frac{\pi}{\lambda}\right)^2 N_{xs}^{(i)}\,(w_s^{(i)} + w_{\circ s}) + \left(\frac{\pi}{\lambda}\right)\Big[\,(N_{\circ xy}^{(i)} - \frac{1}{2}N_{xyc}^{(i)})\,(\beta_c^{(i)} +$$

$$\frac{dw_{\circ s}}{dy}) + \frac{1}{2}N_{xys}^{(i)}(\beta_c^{(i)} + \frac{dw_{\circ c}}{dy})\,\Big] - 2G^{\alpha}\Big[-\frac{d\beta_c^{(i)}}{dy} + \left(\frac{\pi}{\lambda}\right)^2 w_c^{(i)}\Big] -$$

$$G^{\beta}\Big[-\frac{d\beta_c^{(i-1)}}{dy} + \left(\frac{\pi}{\lambda}\right)^2 w_c^{(i-1)} - \frac{d\beta_c^{(i+1)}}{dy} + \left(\frac{\pi}{\lambda}\right)^2 w_c^{(i+1)}\Big] -$$

$$E^{\alpha}(2w_c^{(i)} - w_c^{(i-1)} - w_c^{(i+1)}) ; \tag{3.42}$$

for i = N

$$\frac{dV_{ys}^{(N)}}{dy} = -\left(\frac{\pi}{\lambda}\right)^2 M_{xs}^{(N)} - \left(\frac{\pi}{\lambda}\right)^2 (N_{\circ x}^{(N)} + \frac{1}{2}N_{xc}^{(N)})\,(w_s^{(N)} + w_{\circ s}) +$$

$$\frac{1}{2}\left(\frac{\pi}{\lambda}\right)^2 N_{xs}^{(N)}\,(w_c^{(N)} + w_{\circ c}) - \left(\frac{\pi}{\lambda}\right)\Big[\,(N_{\circ xy}^{(N)} + \frac{1}{2}N_{xyc}^{(N)})\,(\beta_s^{(N)} +$$

$$\frac{dw_{\circ c}}{dy}) + \frac{1}{2}N_{xys}^{(N)}\,(\beta_s^{(N)} + \frac{dw_{\circ s}}{dy})\,\Big] - G^{\alpha}\Big[-\frac{d\beta_s^{(N)}}{dy} + \left(\frac{\pi}{\lambda}\right)^2 w_s^{(N)}\Big] -$$

$$G^{\beta}\Big[-\frac{d\beta_s^{(N-1)}}{dy} + \left(\frac{\pi}{\lambda}\right)^2 w_s^{(N-1)}\Big] - E^{\alpha}(w_s^{(N)} - w_s^{(N-1)}) ; \tag{3.43}$$

$$\frac{dV_{yc}^{(N)}}{dy} = -\left(\frac{\pi}{\lambda}\right)^2 M_{xc}^{(N)} - \left(\frac{\pi}{\lambda}\right)^2 (N_{\circ x}^{(N)} - \frac{1}{2}N_{xc}^{(N)})\,(w_c^{(N)} + w_{\circ c}) +$$

$$\frac{1}{2}\left(\frac{\pi}{\lambda}\right)^2 N_{xs}^{(N)}\,(w_s^{(N)} + w_{\circ s}) + \left(\frac{\pi}{\lambda}\right)\Big[\,(N_{\circ xy}^{(N)} - \frac{1}{2}N_{xyc}^{(N)})\,(\beta_c^{(N)} +$$

$$\frac{dw_{\circ s}}{dy}) + \frac{1}{2}N_{xys}^{(N)}\,(\beta_c^{(N)} + \frac{dw_{\circ c}}{dy})\,\Big] - G^{\alpha}\Big[-\frac{d\beta_c^{(N)}}{dy} + \left(\frac{\pi}{\lambda}\right)^2 w_c^{(N)}\Big] -$$

$$G^{\beta}\left[-\frac{d\beta_c^{(N-1)}}{dy} + \left(\frac{\pi}{\lambda}\right)^2 w_c^{(N-1)}\right] - E^{\alpha}\left(w_c^{(N)} - w_c^{(N-1)}\right). \tag{3.44}$$

The boundary conditions derived from this formulation are:

for i = 1, 2, ..., N

$$N_{\circ xy}^{(i)}\delta u_{\circ}^{(i)}\Big|_0^b = 0 \qquad N_{xys}^{(i)}\delta u_s^{(i)}\Big|_0^b = 0$$

$$N_{xyc}^{(i)}\delta u_c^{(i)}\Big|_0^b = 0 \qquad N_{\circ y}^{(i)}\delta v_{\circ}^{(i)}\Big|_0^b = 0$$

$$N_{ys}^{(i)}\delta v_s^{(i)}\Big|_0^b = 0 \qquad N_{yc}^{(i)}\delta v_c^{(i)}\Big|_0^b = 0$$

$$M_{ys}^{(i)}\frac{\partial}{\partial x}\left(\delta w_s^{(i)}\right)\Big|_0^b = 0 \qquad M_{yc}^{(i)}\frac{\partial}{\partial y}\left(\delta w_c^{(i)}\right)\Big|_0^b = 0$$

$$V_{ys}^{(i)}\delta w_s^{(i)}\Big|_0^b = 0 \qquad V_{yc}^{(i)}\delta w_c^{(i)}\Big|_0^b = 0. \tag{3.45}$$

The model remains rectangular during loading and is simply supported on the unloaded edges. The boundary conditions are expressed as

at y = 0 and at y = b

$$u_{\circ}^{(i)} = u_s^{(i)} = u_c^{(i)} = v_s^{(i)} = v_c^{(i)} = w_s^{(i)} = w_c^{(i)} = 0,$$

$$N_{\circ y}^{(i)} = M_{ys}^{(i)} = M_{yc}^{(i)} = 0. \tag{3.46}$$

3.4.2 Definition of Terms in Preceding Equations

The stress and moment resultants are rearranged into subequations that are only dependent on y, subequations that include sine terms, and subequations that include cosine terms.

A complete description of each is given in reference 21 on pages 82 to 85. The stress and moment resultants are written as:

$$N_x^{(i)} = N_{\circ x}^{(i)}(y) + N_{xs}^{(i)}(y)\sin\frac{2\pi\bar{x}}{\lambda} + N_{xc}^{(i)}(y)\cos\frac{2\pi\bar{x}}{\lambda};$$

$$N_y^{(i)} = N_{\circ y}^{(i)}(y) + N_{ys}^{(i)}(y)\sin\frac{2\pi\bar{x}}{\lambda} + N_{yc}^{(i)}(y)\cos\frac{2\pi\bar{x}}{\lambda};$$

$$N_{xy}^{(i)} = N_{\circ xy}^{(i)}(y) + N_{xys}^{(i)}(y)\sin\frac{2\pi\bar{x}}{\lambda} + N_{xyc}^{(i)}(y)\cos\frac{2\pi\bar{x}}{\lambda};$$

$$M_x^{(i)} = M_{xs}^{(i)}(y)\sin\frac{\pi\bar{x}}{\lambda} + M_{xc}^{(i)}(y)\cos\frac{\pi\bar{x}}{\lambda};$$

$$M_y^{(i)} = M_{ys}^{(i)}(y)\sin\frac{\pi\bar{x}}{\lambda} + M_{yc}^{(i)}(y)\cos\frac{\pi\bar{x}}{\lambda};$$

$$M_{xy}^{(i)} = M_{xys}^{(i)}(y)\sin\frac{\pi\bar{x}}{\lambda} + M_{xyc}^{(i)}(y)\cos\frac{\pi\bar{x}}{\lambda}. \tag{3.47}$$

Other previously undefined functions for the i-th fiber-plate are:

$$V_{ys}^{(i)} = -M_{ys}^{(i)} + \frac{2\pi}{\lambda}M_{xyc}^{(i)} - (N_{\circ y}^{(i)} - \frac{1}{2}N_{yc}^{(i)})\ (\beta_s^{(i)} + \frac{dw_{\circ s}}{dy}) -$$

$$\frac{1}{2}N_{ys}^{(i)}\ (\beta_c^{(i)} + \frac{dw_{\circ c}}{dy}) + (\frac{\pi}{\lambda})\Big[\ (N_{\circ xy}^{(i)} - \frac{1}{2}N_{xyc}^{(i)})\ (w_c^{(i)} +$$

$$w_{\circ c}) - \frac{1}{2}N_{xys}^{(i)}(w_s^{(i)} + w_{\circ s})\ ]; \tag{3.48}$$

$$V_{yc}^{(i)} = -M_{yc}^{(i)} - \frac{2\pi}{\lambda}M_{xys}^{(i)} - (N_{\circ y}^{(i)} + \frac{1}{2}N_{yc}^{(i)})\ (\beta_c^{(i)} + \frac{dw_{\circ c}}{dy}) -$$

$$\frac{1}{2}N_{ys}^{(i)}\ (\beta_s^{(i)} + \frac{dw_{\circ s}}{dy}) - (\frac{\pi}{\lambda})\Big[\ (N_{\circ xy}^{(i)} + \frac{1}{2}N_{xyc}^{(i)})\ (w_s^{(i)} +$$

$$w_{o_s}) - \frac{1}{2} N_{xys}^{(i)} (w_c^{(i)} + w_{o_c})] ; \tag{3.49}$$

$$\beta_s^{(i)} = \frac{dw_s^{(i)}}{dy} ; \tag{3.50}$$

$$\beta_c^{(i)} = \frac{dw_c^{(i)}}{dy} . \tag{3.51}$$

The functions of y for w_{o_s} and w_{o_c} are expressed as

$$w_{o_s}(y) = \bar{w}_{o_s} \sin \frac{\pi y}{b} ,$$

$$w_{o_c}(y) = \bar{w}_{o_c} \cos \frac{\pi y}{b} , \tag{3.52}$$

where $\bar{w}_{o_s} = \bar{w}_{o_c} = W_o$, and is equal to the amplitude of the initial imperfection.

3.4.3 Solution Procedure of Nonlinear Theory

An approximate solution to the nonlinear coupled ordinary differential equations is obtained by using an algorithm developed by Lentini and Pereyra[29]. The algorithm is based on Newton's method and can be used to solve a system of simultaneous first-order nonlinear ordinary differential equations subject to two-point boundary conditions. The algorithm uses finite differences to solve the differential equations. Adaptive mesh spacings are automatically produced so that mild boundary layers are detected and resolved. The difference between successive approximations for each unknown is calculated. The algorithm iterates until this difference is less than a specified tolerance.

The first-order governing equations for a model with anisotropic fiber-plates can be expressed as a function of 20 unknowns for each fiber-plate. These unknowns for the i-th fiber-plate are listed below. The other unknowns are expressed as functions of these twenty.

The twenty first-order differential equations were obtained through substituting into and reorganizing equations (3.20), (3.21), (3.37) to (3.43), and (3.44). The 20 unknowns for an eight-layer plate are

$$u_{\circ}^{(i)}, u_{s}^{(i)}, u_{c}^{(i)}, v_{\circ}^{(i)}, v_{s}^{(i)}, v_{c}^{(i)}, w_{s}^{(i)}, w_{c}^{(i)}, \beta_{s}^{(i)}, \beta_{c}^{(i)}$$

$$N_{y^{\circ}}^{(i)}, N_{ys}^{(i)}, N_{yc}^{(i)}, N_{xy^{\circ}}^{(i)}, N_{xys}^{(i)}, N_{xyc}^{(i)}, M_{ys}^{(i)}, M_{yc}^{(i)}, V_{ys}^{(i)}, V_{yc}^{(i)} . \tag{3.53}$$

3.4.4 Computer Program for Nonlinear Theory

The program to implement the nonlinear theory, written in conjunction with reference 21 and known as THESN, was originally run on a Cyber 205. The finite-difference analysis has a maximum of 41 stations. The ratio of the maximum distance between adjacent stations to plate width is 0.05 when using all 41 stations. Since the results of this analysis are approximate, an error tolerance is specified for each unknown in the nonlinear analysis. This specified tolerance between successive iterations is approximately 1% of the maximum calculated value for each unknown. The next chapter describes modifications to the program to extend its capabilities beyond its original form.

4.0 MODIFICATION AND ADDITIONS TO THEORY

This chapter deals with modifications and additions to the theory presented in the previous chapter. The major emphasis of the modifications and additions are placed on obtaining and using further information from the theory, the associated computer programs, and making the theory more versatile.

4.1 Linear Theory

As mentioned in Chapter 3, coding for the analysis based on the linear buckling theory resulted in the computer program named THESL. Given a particular laminate, or lay-up scheme, the purpose of the analysis using the linear theory was to obtain a critical buckling load, or strain, and a critical half-wavelength. THESL was originally written in FORTRAN for a Control Data Corporation CYBER computer at the NASA Langley Research Center. The program was transferred to Virginia Polytechnic Institute and State University. THESL was then modified so it would run on an IBM 3090 computer. The most current version of THESL takes less than 35 seconds clock time to run on the IBM 3090.

4.1.1 Modifications to the Linear Theory

Mostly cosmetic and portability changes were made to THESL. The version of FORTRAN originally used to write the program was not current, so minor changes were made to bring the FORTRAN to the FORTRAN 77 standard. Also the program was changed to double precision. This allowed more accurate results when a FORTRAN compiler would not implicitly make the program double precision. The eigenvalue solving subroutines and the minimizer subroutine used in the original program were routines written at the NASA Langley Research Center. Equivalent subroutines from the International Math Subroutine Library (IMSL) were used in their place. These subroutines are from a highly refined commercially available package. Most mainframe computers use the IMSL library, so the program should be quite portable. The modifications also enhanced the accuracy of THESL. The program uses an initial guess in the calculation of the critical buckling half-wavelength. To check the eigenvalue solving accuracy and the accuracy of the search routine for the critical wavelength, two input test cases, identical except for the initial guess of the critical wavelength, were submitted to the original program on the CYBER. The critical wavelengths obtained from the two test cases differed by about 5%. When the same two test cases were submitted to the modified program on the IBM 3090 at Virginia Polytechnic Institute and State University, results which agreed to five significant digits were obtained. The modified version of the program is known as THESLD.

4.1.2 Using The Modified Linear Theory and a Sample Test Case

The linear code THESLD reads from a single input file and writes three output files. Except for the two text lines at the beginning of the input file, the reading of the input data was changed to list directed input so that data on an input line can be separated by commas, eliminating the need to remember restrictive format fields. The output files consists of a file that will contain any error or special messages, a file that essentially echoes the input file, holds the calculated critical half-wavelength and buckling load, and a file to hold two columns of data representing strain versus half-wavelength for a given laminate. The user may select from four options, or cases, when conducting an analysis of a laminate. The option chosen depends on the type of laminate. These options are:

A. All layers orthotropic, and all layers the same;

B. All layers anisotropic, and all layers the same;

C. All layers orthotropic, and all layers may be different, and;

D. All layers anisotropic, and all layers may be different.

The last option will perform any of the analyses of the first three options, but the less general options may take less cpu time. Option A utilizes a closed-form solution which takes considerably less computer time, so it should be used when ever possible. The present work primarily uses options A and D.

A sample input file and output from the program are included in Appendix A. A description of the input file is also give in Appendix A. The laminate considered in the sample case uses eight layers, a 30° angle-ply lay-up, and the IM7/8551-7a material system.

4.2 Nonlinear Theory

The analysis using the nonlinear theory consists of three main computer programs and the data interpretation associated with those programs. The original and primary code is called THESN. The modified version of THESN is known as THESNS. Two post-processor programs were written to make the data interpretation faster and make THESNS more powerful.

The original nonlinear program was written for the CYBER system. No analyses were conducted in the present study using the nonlinear program on the CYBER. For the current work the THESN FORTRAN program was transferred to a CONVEX computer used by the Aircraft Structures Branch at the NASA-Langley Research Center. The THESN program is self-contained and essentially no modifications were made to allow it to run on the CONVEX.

The purpose of the analysis using the nonlinear theory is to obtain inplane stresses and interlaminar strains for a laminate with a specified level of imperfection, load level, lay-up, and material system. The finite-difference method used to solve the series of differential equations results in solutions at discrete x, y, and layer locations. The two post-processor programs use these data to calculate stresses and strains at the discrete points, and then search for the highest stresses and strains at each layer and load step.

The procedure for the analysis using the nonlinear theory is as follows: Elastic properties, a description of laminate geometry, imperfection levels, and load steps, are input into THESNS. The output from THESNS is post-processed to obtain stresses and strains. The incremental load steps allow the user to start ‘loading’ the laminate at an appropriate load level, and then keep increasing the load until a point at which the laminate ‘fails’ because one or more of the inplane stresses or interlaminar shear strains has exceeded a certain failure level.

4.2.1 Modifications to Nonlinear Theory

Two major types of modifications were made to the original computer code. The first type was to change the program to execute faster. At the initial load step the computer program relied on estimates, or guesses, for solutions to each of the variables in the first-order nonlinear differential equations that it solved by iteration. In the original program, when the variables at the second and consecutive load steps were solved for, the program would start over on its solving process and use the original guesses. This was changed so the results from the previous load step were used as guesses for the next load step. For a four load step case, approximately 33% of the cpu time was saved.

The second type of modification of the nonlinear theory was made so that it would be more general. The nonlinear theory was changed so that each layer of the laminate could have a different amplitude of imperfection. The wavelength of each imperfection in the laminate is still the same, however. In the original program the out-of-plane displacement for the i-th layer, equation (3.37), was as follows:

$$w^{(i)\circ} = w_{\circ_s}(y)\sin\frac{\pi\bar{x}}{\lambda} + w_{\circ_c}(y)\cos\frac{\pi\bar{x}}{\lambda} + w_s^{(i)}(y)\sin\frac{\pi\bar{x}}{\lambda} + w_c^{(i)}(y)\cos\frac{\pi\bar{x}}{\lambda}, \tag{4.1}$$

where the $w_{\circ_s}$ and $w_{\circ_c}$ terms contain the initial imperfection and are defined as

$$w_{\circ_s}(y) = \bar{w}_{\circ_s}\sin\frac{\pi y}{b},$$

$$w_{\circ_c}(y) = \bar{w}_{\circ_c}\cos\frac{\pi y}{b}. \tag{4.2}$$

With the modified nonlinear theory it is assumed that each layer can have a different initial imperfection. The out-of-plane displacement of the i-th layer then becomes

$$w^{(i)\circ} = w_{\circ_s}^{(i)}(y)\sin\frac{\pi\bar{x}}{\lambda} + w_{\circ_c}^{(i)}(y)\cos\frac{\pi\bar{x}}{\lambda} + w_s^{(i)}(y)\sin\frac{\pi\bar{x}}{\lambda} + w_c^{(i)}(y)\cos\frac{\pi\bar{x}}{\lambda}, \tag{4.3}$$

where the $w_{\circ_s}^{(i)}$ and $w_{\circ_c}^{(i)}$ terms contain the initial imperfection and are now defined as

$$w_{\circ_s}^{(i)}(y) = \bar{w}_{\circ_s}^{(i)}\sin\frac{\pi y}{b},$$

$$w_{\circ_c}^{(i)}(y) = \bar{w}_{\circ_c}^{(i)}\cos\frac{\pi y}{b}. \tag{4.4}$$

The $\bar{w}^{(i)}_{\circ s}$ and $\bar{w}^{(i)}_{\circ c}$ terms are the amplitudes of the initial imperfections that can vary from layer to layer.

Also, the computer program THESN was modified so that elastic properties, strains, load levels, load step information, and ply information were written to a separate file for post-processing. Output to the original file was not changed. The modified code, THESNS, writes out the following values for each layer at each discrete point x, y:

$$\varepsilon^{(i)}_{xo}, \varepsilon^{(i)}_{xs}, \varepsilon^{(i)}_{xc}, \varepsilon^{(i)}_{yo}, \varepsilon^{(i)}_{ys}, \varepsilon^{(i)}_{yc}, \gamma^{(i)}_{xyo}, \gamma^{(i)}_{xys}, \gamma^{(i)}_{xyc}$$

$$\kappa^{(i)}_{xs}, \kappa^{(i)}_{xc}, \kappa^{(i)}_{ys}, \kappa^{(i)}_{yc}, \kappa^{(i)}_{xys}, \kappa^{(i)}_{xyc}.$$

These expressions listed above are used to formulate stresses and strains and will be explained in the next section.

4.2.2 Post-Processors

As mentioned, two post-processors were written to help with the present work. The two post-processor programs quickly search through and manipulate data from THESNS. The first program is called MOREI. The second program is called EXTRACTI. The program MOREI uses inplane strains, curvatures, and elastic properties to obtain inplane stresses. The inplane strain components are defined as:

$$\varepsilon^{(i)}_{x} = \varepsilon^{(i)}_{xo} + \varepsilon^{(i)}_{xs}\sin\frac{2\pi\bar{x}}{\lambda} + \varepsilon^{(i)}_{xc}\cos\frac{2\pi\bar{x}}{\lambda} + z^{(i)}\kappa^{(i)}_{xs}\sin\frac{\pi\bar{x}}{\lambda} + z^{(i)}\kappa^{(i)}_{xc}\cos\frac{\pi\bar{x}}{\lambda},$$

$$\varepsilon^{(i)}_{y} = \varepsilon^{(i)}_{yo} + \varepsilon^{(i)}_{ys}\sin\frac{2\pi\bar{x}}{\lambda} + \varepsilon^{(i)}_{yc}\cos\frac{2\pi\bar{x}}{\lambda} + z^{(i)}\kappa^{(i)}_{ys}\sin\frac{\pi\bar{x}}{\lambda} + z^{(i)}\kappa^{(i)}_{yc}\cos\frac{\pi\bar{x}}{\lambda},$$

$$\gamma_{xy}^{(i)} = \gamma_{xyo}^{(i)} + \gamma_{xys}^{(i)} \sin\frac{2\pi\bar{x}}{\lambda} + \gamma_{xyc}^{(i)} \cos\frac{2\pi\bar{x}}{\lambda} + z^{(i)}\kappa_{xys}^{(i)} \sin\frac{\pi\bar{x}}{\lambda} + z^{(i)}\kappa_{xyc}^{(i)} \cos\frac{\pi\bar{x}}{\lambda}. \quad (4.5)$$

The strains are then combined with elastic properties of each layer to obtain inplane stresses as

$$\sigma_x^{(i)}(x,y) = \bar{Q}_{11}\varepsilon_x^{(i)}(x,y) + \bar{Q}_{12}\varepsilon_y^{(i)}(x,y) + \bar{Q}_{16}\gamma_{xy}^{(i)}(x,y),$$

$$\sigma_y^{(i)}(x,y) = \bar{Q}_{12}\varepsilon_x^{(i)}(x,y) + \bar{Q}_{22}\varepsilon_y^{(i)}(x,y) + \bar{Q}_{26}\gamma_{xy}^{(i)}(x,y),$$

$$\tau_{xy}^{(i)}(x,y) = \bar{Q}_{16}\varepsilon_x^{(i)}(x,y) + \bar{Q}_{26}\varepsilon_y^{(i)}(x,y) + \bar{Q}_{66}\gamma_{xy}^{(i)}(x,y). \quad (4.6)$$

The stresses are transformed into the fiber coordinate system as

$$\sigma_1^{(i)}(x,y) = \sigma_x^{(i)}(x,y)c^2 + \sigma_y^{(i)}(x,y)s^2 + 2\tau_{xy}^{(i)}(x,y)sc,$$

$$\sigma_2^{(i)}(x,y) = \sigma_x^{(i)}(x,y)s^2 + \sigma_y^{(i)}(x,y)c^2 - 2\tau_{xy}^{(i)}(x,y)sc,$$

$$\tau_{12}^{(i)}(x,y) = -\sigma_x^{(i)}(x,y)sc + \sigma_y^{(i)}(x,y)cs + 2\tau_{xy}^{(i)}(x,y)\,(c^2 - s^2), \quad (4.7)$$

where s stands for $\sin\theta^{(i)}$, c stands for $\cos\theta^{(i)}$, and $\theta^{(i)}$ is the angle of orientation for each layer. Definitions for the transformations and $\bar{Q}_{ij}$ can be found in texts on classical lamination theory.[25,26]

The program MOREI then searches in the x direction and y direction to find the maximum fiber, inplane transverse, and inplane shear stress for each layer and each load step. The maximum stresses at two consecutive load steps are then linearly interpolated to obtain load levels that result in failure based on previously determined failure values for fiber direction, inplane transverse, and inplane shear stresses.

The program EXTRACTI extracts interlaminar strains γ_{xz}, γ_{yz}, and ε_z, and w displacements for each layer from another output file. Searches for the interlaminar strains are performed in the x and y directions and between every set of layers. A search is also made for the displacements. Maximum values of the strains and displacements are obtained for each load step. A linear interpolation method is again used to obtain failure loads based on specified failure levels of interlaminar shear strain. Neither extensional strain nor displacement w is considered critical so no interpolation is done with these quantities.

4.2.3 Sample Case for Analysis using the Nonlinear Theory

A sample input file and a summary of the output from the nonlinear theory are included in Appendix B. A description of the input file is given in Appendix B. The laminate considered in the sample case uses eight layers, a 30° angle-ply lay-up, and the IM7/8551-7a material system.

The next chapter describes results that were obtained using the programs discussed in this chapter. These results are used to help explain the discrepancies between experimental results and classical predictions as discussed in Chapter 2.

5.0 ANALYTICAL RESULTS

The analytical results presented in this chapter are obtained using the theory presented in the previous chapters. The emphasis will be on the nonlinear analysis, particularly on the role that wavy-layer type imperfections play in determining laminate compressive strength. Two categories of wavy-layer type imperfections will be discussed: The first category includes imperfections where the imperfection length is the critical buckling half-wavelength. For the present work there is no concern as to how the imperfections appear in that form. The linear buckling analysis is used to determine these critical half-wavelengths and, though they are not used, critical loads for this category. The second category includes imperfections of the wavy-layer type but where the half-wavelengths are not the critical half-wavelengths, rather the wavelengths represent manufacturing imperfections. For this second category, waviness or imperfections that are the same for every layer, as well as imperfections that vary from layer to layer, will be investigated. For both categories the amplitude of the imperfection will be assumed to be either one-tenth, two-tenths, or one-half a layer thickness in amplitude. All laminates discussed and analyzed in this chapter will be angle-ply laminates with a lay-up of $[(\pm\theta)/(\mp\theta)]_s$, where $0^\circ \le \theta \le 90^\circ$ and θ will be referred to as the off-axis angle. Analytical predictions and experimental results using the IM7/8551-7a material system will be compared with analytical predictions and experimental results that use the AS4/3502 material system.

5.1 Results from Linear Theory

The elastic properties and strengths for IM7/8551-7a, as determined in chapter 2 and documented Table 2.2, are presented again in Table 5.1. In the context of the analysis the laminate properties are assigned to the properties of the fiber-plate. The layer thickness used in the computations will be 0.00573 in., as calculated in chapter 2. In the table the superscript 'c' denotes compressive properties and the superscript 't' denotes tensile properties.

Table 5.1 IM7/8551-7a Elastic Properties and Strengths

Fiber-Plate			Matrix-Foundation[30]			Strengths		
E_{11}	(Msi)	21.0	E_m	(Msi)	0.506	S_1^c	(ksi)	240
E_{22}	(Msi)	1.28	G_m	(Msi)	0.185	S_2^c	(ksi)	31.4
G_{12}	(Msi)	0.707	ν_m		0.366	S_2^t	(ksi)	7.70
ν_{12}		0.360				S_{12}	(ksi)	17.2

As mentioned in conjunction with Table 2.2, the fiber-plate Poisson's ratio given in Table 5.1 was not obtained from the experimental tests. Because of the poor quality of the Poisson's ratio data acquired experimentally, a published value was chosen. From studies conducted using both the linear and nonlinear theory, it was determined any fiber-plate Poisson's ratio between 0.32 and 0.36 will give virtually identical results. Properties for the matrix-foundation are neat resin properties and were taken from reference 30. Elastic properties and strengths for AS4/3502 from previous work[21,31] are shown in Table 5.2. The layer thickness used in the AS4/3502 computations is 0.0052 in.

5.1.1 Critical Buckling Half-Wavelengths and Loads

For an infinitely long isotropic plate simply-supported along two sides, the buckling

Table 5.2 AS4/3502 Elastic Properties and Strengths

Fiber-Plate[21]			Matrix-Foundation[21]			Strengths		
E_{11}	(Msi)	18.5	E_m	(Msi)	0.590	$S_1{}^c$	(ksi)	206.0[31]
E_{22}	(Msi)	1.64	G_m	(Msi)	0.260	$S_2{}^c$	(ksi)	36.99[21]
G_{12}	(Msi)	0.870	ν_m		0.360	$S_2{}^t$	(ksi)	6.30[31]
ν_{12}		0.300				S_{12}	(ksi)	13.80[21]

load can be computed as a function of the assumed buckling wavelength. The buckling load vs. buckling wavelength relationship for laminated plates is similar. The lowest buckling load is called the critical buckling load and the corresponding wavelength is called the critical wavelength. In figure 5.1 normalized buckling loads are plotted as a function of normalized buckling wavelength for a representative laminate using the IM7/8551-7a material system. Note there is a minimum buckling load that has an associated wavelength. By the nature of the relationship shown in figure 5.1, a buckling analysis usually involves searching for the critical, or lowest, load.

Using the above idea to find the lowest buckling load, critical buckling loads for IM7/8551-7a and AS4/3502 are computed using the linear multilayer analysis described in chapters 3 and 4. The buckling loads are shown as a function of off-axis angle in figure 5.2. Critical buckling half-wavelengths for IM7/8551-7a and AS4/3502, normalized by the thickness of one layer, are shown as a function of off-axis angle in figure 5.3. Notice that the buckling loads are practically independent of off-axis angle, whereas the critical half-wavelength decreases with increasing off-axis angle. The critical wavelengths range from 12 to 27 layer thicknesses. The normalized quantities provide insight into the length scales involved in this study. The data of figure 5.3 are tabulated in Table 5.3. These data are important because the next section will discuss the nonlinear analysis of laminates with im-

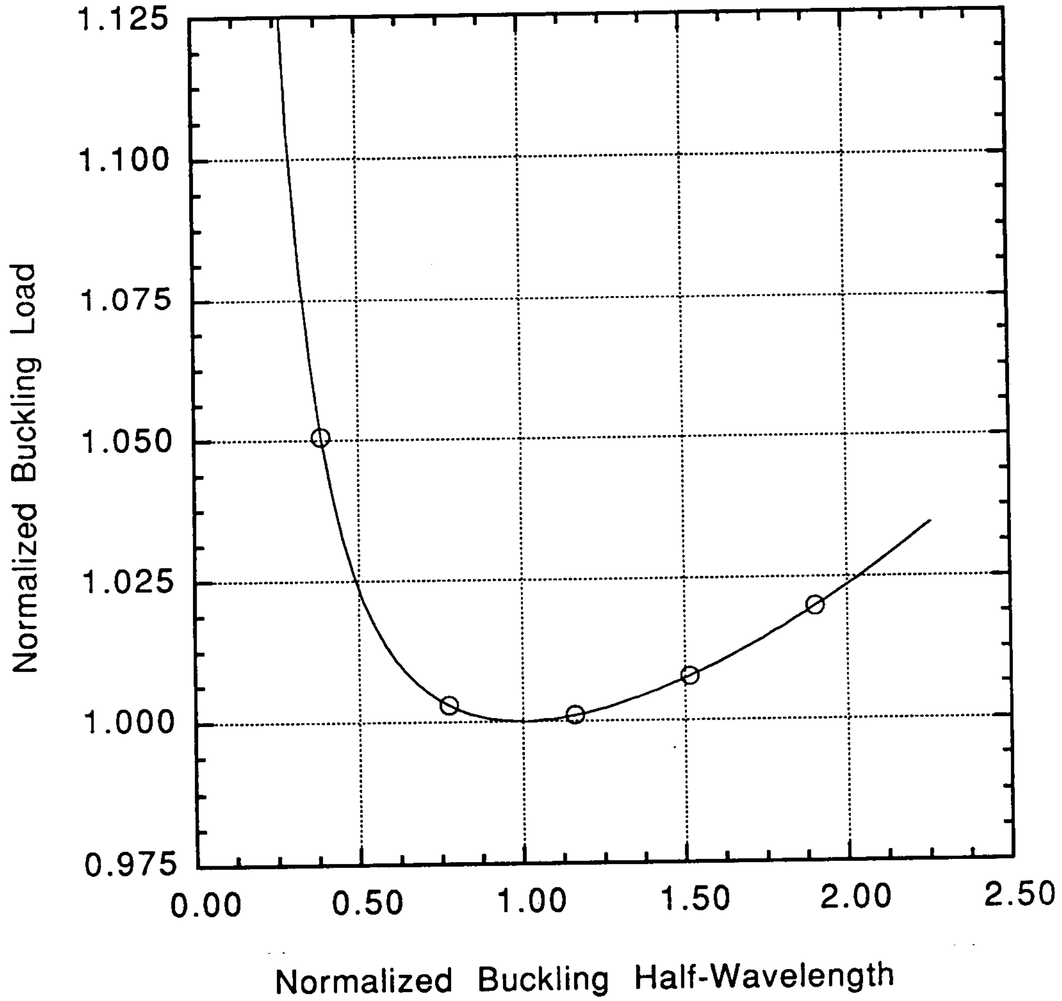

Figure 5.1 Normalized buckling loads vs. normalized buckling wavelengths.

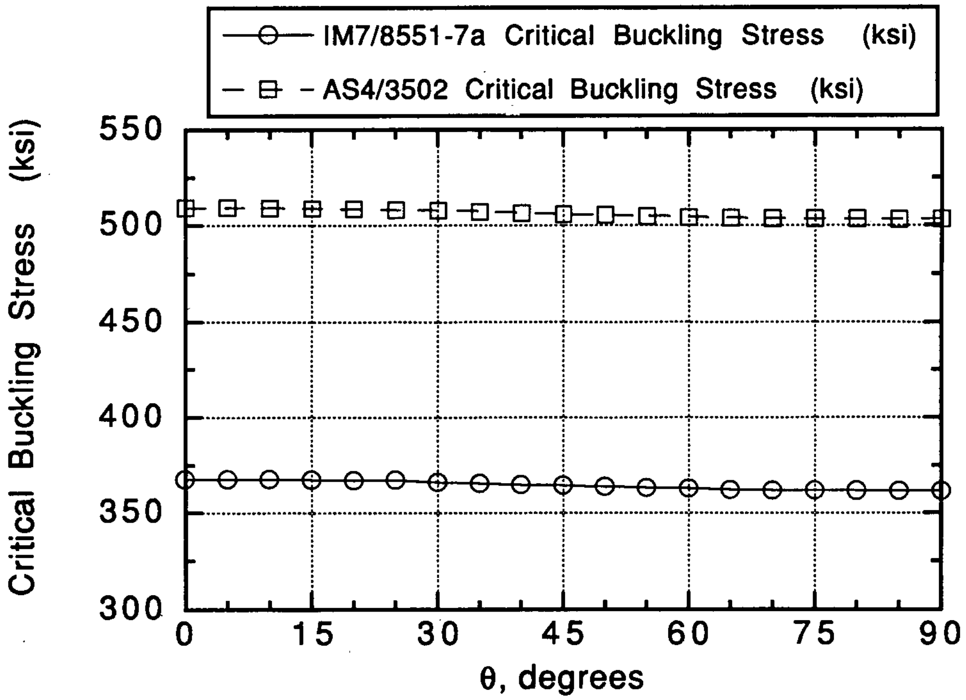

Figure 5.2 Critical buckling loads as a function of off-axis angle.

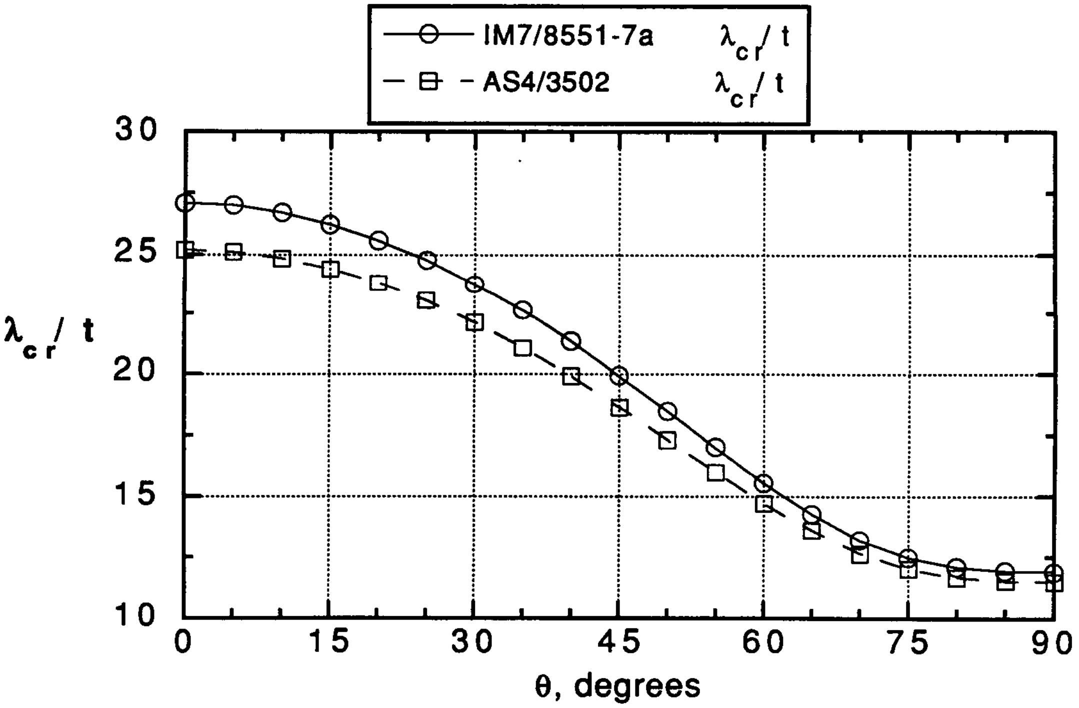

Figure 5.3 Normalized critical half-wavelengths as a function of off-axis angle.

ANALYTICAL RESULTS

C-2

perfections with the shape of the critical short-wavelength buckling mode.

It was noted in chapter 2 in the section on test fixtures that if the test section lengths are smaller than or close in size to the critical buckling half-wavelength, then the fixture could restrain the laminate from failing in the short-wavelength buckling mode. The critical half-wavelengths found in Table 5.3 are useful in determining proper test section lengths.

Table 5.3 Critical Half-Wavelengths for IM7/8551-7a and AS4/3502

Angle	λ_{cr} for IM7/8551-7a		λ_{cr} for AS4/3502	
	(in.)	λ_{cr}/t	(in.)	λ_{cr}/t
0°	0.155	27.1	0.131	25.2
5°	0.155	27.0	0.131	25.2
10°	0.153	26.7	0.129	24.8
15°	0.150	26.2	0.126	24.2
20°	0.147	25.7	0.124	23.8
25°	0.142	24.8	0.120	23.0
30°	0.136	23.7	0.115	22.1
35°	0.130	22.6	0.110	21.1
40°	0.122	21.3	0.104	19.9
45°	0.114	19.9	0.0970	18.7
50°	0.106	18.5	0.0900	17.3
55°	0.0974	17.0	0.0831	16.0
60°	0.0892	15.6	0.0765	14.7
65°	0.0817	14.3	0.0705	13.6
70°	0.0757	13.2	0.0658	12.7
75°	0.0716	12.5	0.0625	12.0
80°	0.0694	12.1	0.0607	11.7
85°	0.0685	12.0	0.0600	11.5
90°	0.0682	11.9	0.0598	11.5

Critical buckling strains as a function of off-axis angle for IM7/8551-7a and AS4/3502 are shown in figure 5.4. The critical strains tend to increase rather dramatically as the off-axis angle increases, though they are quite constant for $0^\circ \leq \theta \leq 15^\circ$ and for $75^\circ \leq \theta \leq 90^\circ$. This increase is due to decreasing stiffness of the laminate as a function of off-axis angle.

None of the calculations used to create the previously mentioned figures take into account that a laminate may fail due to another mechanism before it reaches a critical buck-

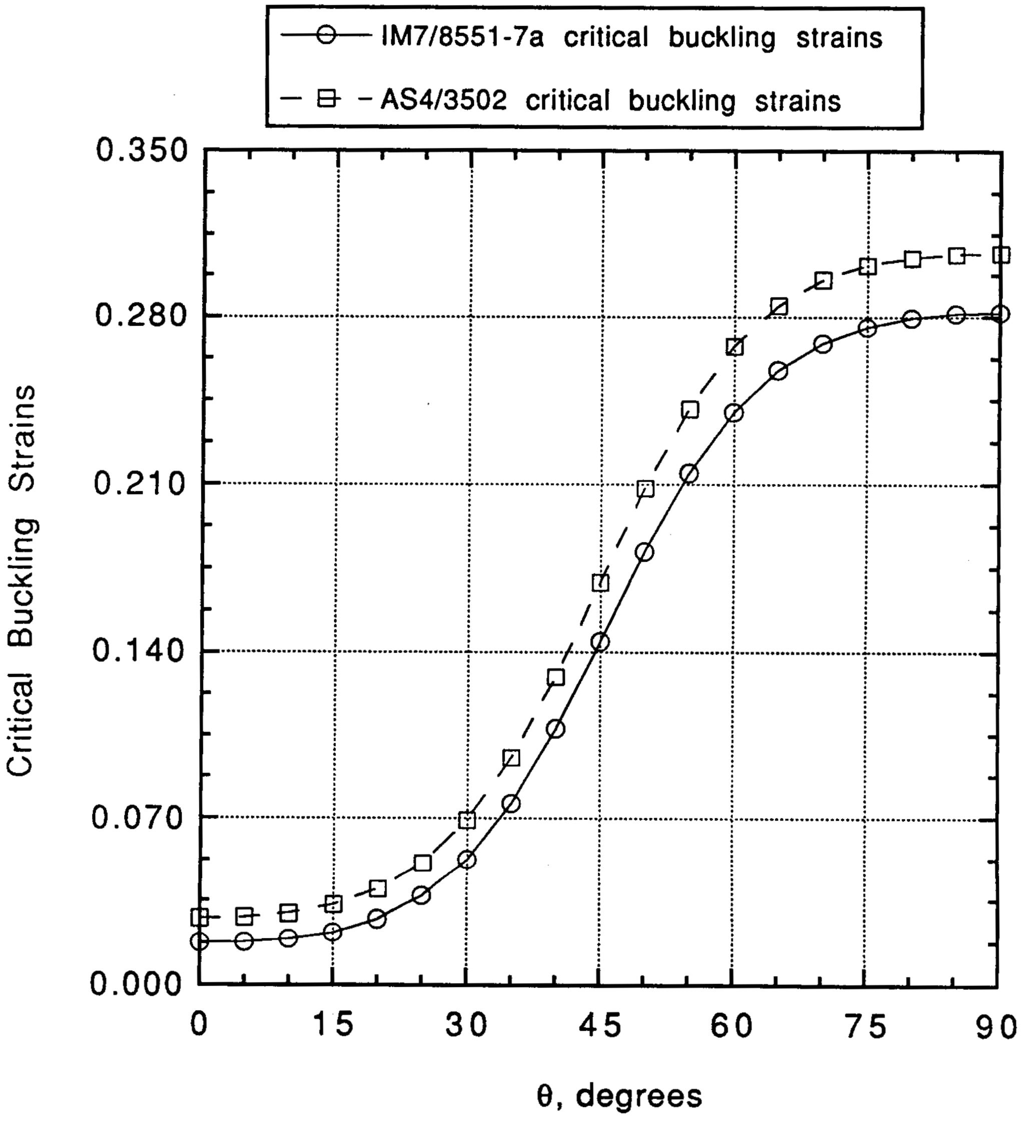

Figure 5.4 Critical buckling strains as a function of off-axis angle.

ling load or strain. Hence, laminates with certain stiffnesses or lamina orientations may never reach their critical buckling loads or strains. Thus, the critical short-wavelength buckling loads obtained from the linear analysis represent an upper bound on compressive strength for high-modulus laminates.

5.2 Imperfections Having Critical Half-Wavelengths

In the chapter 3 it was mentioned that the critical half-wavelength λ_{cr} can be considered a laminate property. A possible form for imperfections in a laminate is that of a wavy layer, the waviness being in the form of the buckling mode with half-wavelength λ_{cr} and amplitude W_0. Such imperfections could possibly come from thermal buckling of the plies during curing of the laminate, buckling of initially flat plies, and various other sources.

To follow is an examination of the influence on compression strength of imperfections where the imperfection lengths are the critical half wavelengths, and the imperfections have various amplitudes. It was determined through observation and calculation in references 21 and 22 that a reasonable maximum imperfection amplitude W_0 would be 0.5t, where t is the thickness of a layer as defined in chapter 3. Imperfection amplitudes of 0.1t and 0.2t are also considered in order to understand the effects of imperfection amplitude.

5.2.1 Results with $W_0 = 0.1t$ and $\lambda = \lambda_{cr}$

In figure 5.5 predictions from the nonlinear analysis are compared to experimental and classical predictions for IM7/8551-7a. For the predictions shown in figure 5.5 the nonlinear analysis used critical half-wavelengths and an imperfection amplitude of 0.1t. Failure is predicted using the maximum stress criterion. By classical is meant the use of classical lamination theory to compute the stresses in a perfectly flat laminate, that is, one with no im-

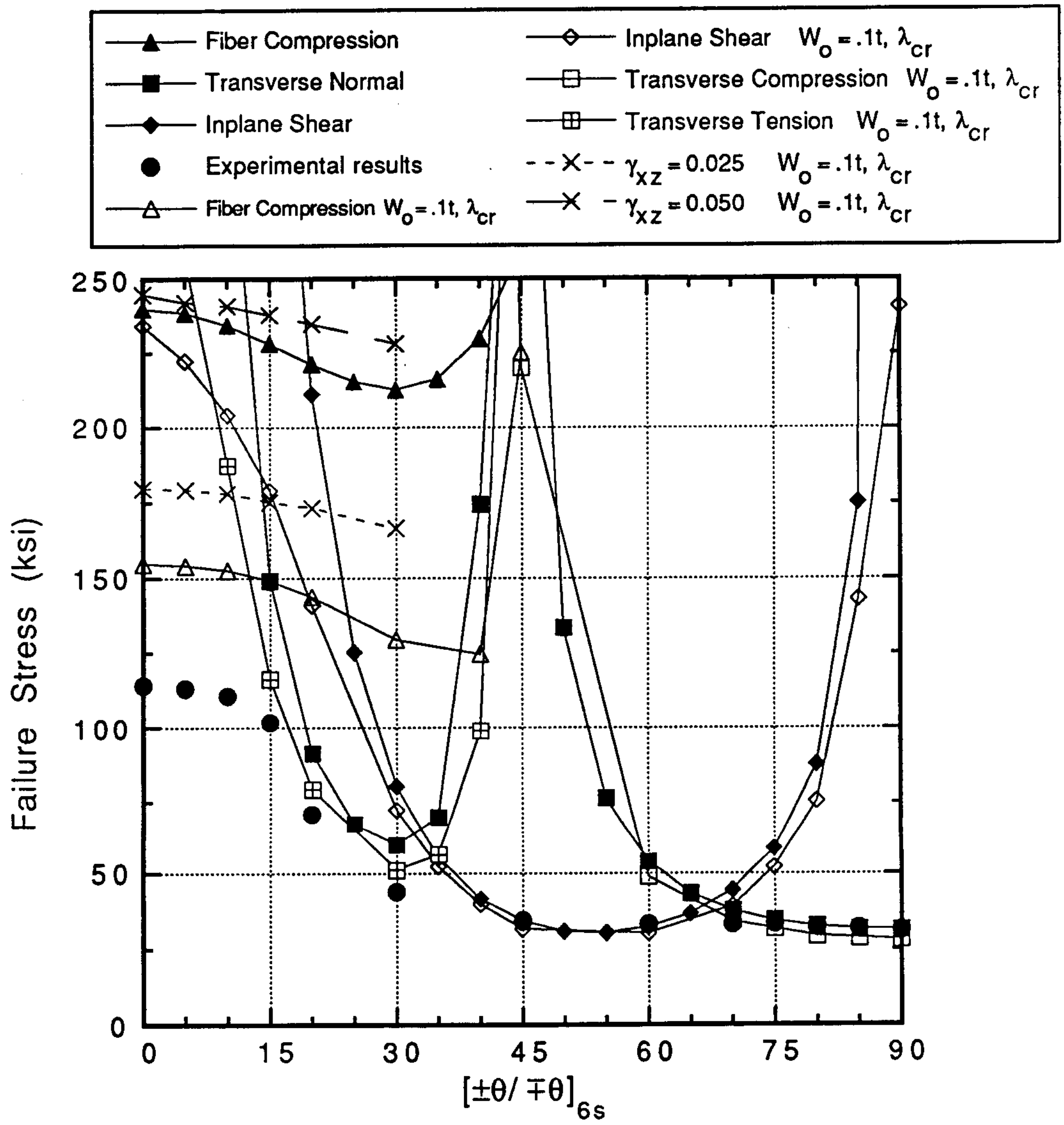

Figure 5.5 Comparison of nonlinear and classical predictions and experimental results for IM7/8551-7a with $W_0 = 0.1t$ and $\lambda = \lambda_{cr}$.

perfections. The classical predictions were discussed in chapter 2. The filled circles represent experimental results. The filled triangles represent fiber compression failure predicted using classical lamination theory. The filled diamonds represent inplane shear failure predicted using the classical theory. The filled squares represent inplane transverse normal failure using the classical theory. The transverse normal failure mode includes failure due to inplane transverse tension and failure due to transverse compression. Recall, for $\theta < 45^\circ$ the transverse failure mode is predicted to be tension, while for $\theta > 45^\circ$ the transverse failure mode is predicted to be compression. Symbols of the same type are joined together to form a failure locus. The loci discussed so far are the same as those in figure 2.36. However, figure 5.5 includes additional loci. The loci of open triangles, diamonds, and squares represent the same predicted failure modes as the closed triangles, diamonds, and squares, but use the nonlinear analysis to compute fiber direction, transverse, and shear stresses, and the resulting failure loads. The x's with the short and long dashes represent failure due to interlaminar shear strain γ_{xz} using failure strain levels of 0.025 and 0.050, respectively, i.e., $\gamma_{xz}^{max} = 0.025$ or $\gamma_{xz}^{max} = 0.050$. Two values were used because an accurate failure strain for γ_{xz} could not be found, although conflicting values of 0.031 and 0.051 were obtained[30]. The assumed γ_{xz}^{max} value of 0.050 is probably more correct than $\gamma_{xz}^{max} = 0.025$ but both will be discussed. The interlaminar shear strain γ_{xz} was used because it was at least an order of magnitude larger than other interlaminar strains. Of all the loci in the figure, at a particular off-axis angle the locus with the lowest predicted failure load is the important one, or the one considered to cause failure.

Using the method discussed in the previous chapter for determining failure and considering the locus with the lowest failure load, the failure modes for figure 5.5 are predicted to be: fiber compression for θ in the range of 0° to 12°; inplane transverse tension for θ in the range of approximately 12° to 35°; inplane shear for θ in the range of 35° to 70°, and; transverse compression for θ in the range of 70° to 90°. Because of the imperfection, failure, whatever the mode, occurs at a particular x-y location and within a particular layer. In fact, failure occurs at a particular z location within a certain layer. If the laminate was perfectly flat, as the classical theory assumes, failure would occur at all x-y locations simultaneously and entirely through the thickness of all layers. In addition, interlaminar failure would not be an issue.

It appears that for θ ranging from 45° to 90° there is no major difference between nonlinear predictions and the classical predictions. This corresponds well with the previous assumption that angle-ply laminates are not sensitive to imperfections for angles greater than about 40°. More importantly, in this range of θ there is good agreement between the experimental and the predictions.

Although an imperfection in a 0° specimen with a critical half-wavelength of 27t, or 0.155 in., and an imperfection amplitude of 0.1t is not considered severe, the predicted compression strength for a 0° specimen, limited by the fiber compression failure mode, decreased from 240 ksi (the classical prediction) to approximately 155 ksi, this represents a reduction in strength of almost one-half. Between θ = 0° and θ = 15° the compression strength predicted by the nonlinear analysis varies little. Correspondingly, between 0° and 10° the experimental results were quite constant. It appears that failure due to interlaminar shear at $\gamma_{xz}^{max} = 0.050$ occurs at a higher load than failure due to fiber compression using the classical theory.

For θ between approximately 15° and 35° inplane transverse tension is predicted to be the dominant failure mode, both by the classical theory and by the nonlinear theory. The solid squares in that region represent predictions due to inplane transverse tension using the classical theory. The open squares with the crosses in them represent failure loads due to inplane transverse tension using the nonlinear theory. The failure loads due to inplane transverse tension using nonlinear theory show good correlation with the experimentally observed values.

Relative to the classical theory, with the nonlinear analysis the inplane shearing mode changed dramatically. Using the nonlinear analysis and an off-axis angle of 0°, for the inplane shear mode there is a distinct predicted failure load of approximately 238 ksi. However, at $\theta = 0°$ and for failure due to inplane shear, the classical theory predicts a compressive failure load of infinity. This implies that even a small imperfection can alter the importance of shear stress in a laminate at low off-axis angles.

Predictions using the nonlinear analysis are compared with experimental results and classical predictions for AS4/3502 in figure 5.6. The nonlinear analysis shown in figure 5.6 uses critical half-wavelengths and an imperfection amplitude of 0.1t. The symbols representing experimental and predicted loads are the same as those discussed for figure 5.5 except that the x's with the medium dashed lines represent interlaminar shear failure at γ_{xz}^{max} of 0.036. This failure level was used in refs. 21 and 22 when considering interlaminar shear in AS4/3502 and is used here simply for consistency. For comparison with the predictions for IM7/8551-7a the failure loci for $\gamma_{xz}^{max} = 0.050$ and 0.025 are included.

From the failure loci, the failure modes predicted for AS4/3502 using critical half-wavelengths and an imperfection amplitude of 0.1t are: fiber compression for θ ranging from 0° to approximately 12°; inplane transverse tension for θ in the range of approximately 12° to 32°; inplane shear for θ ranging from 32° to approximately 75°, and; transverse compression for θ ranging from 75° to 90°. Because in figure 5.6 the interlaminar shear strain loci for $\gamma_{xz}^{max} = 0.036$ and $\gamma_{xz}^{max} = 0.050$ are off the scale, it can be seen by comparing

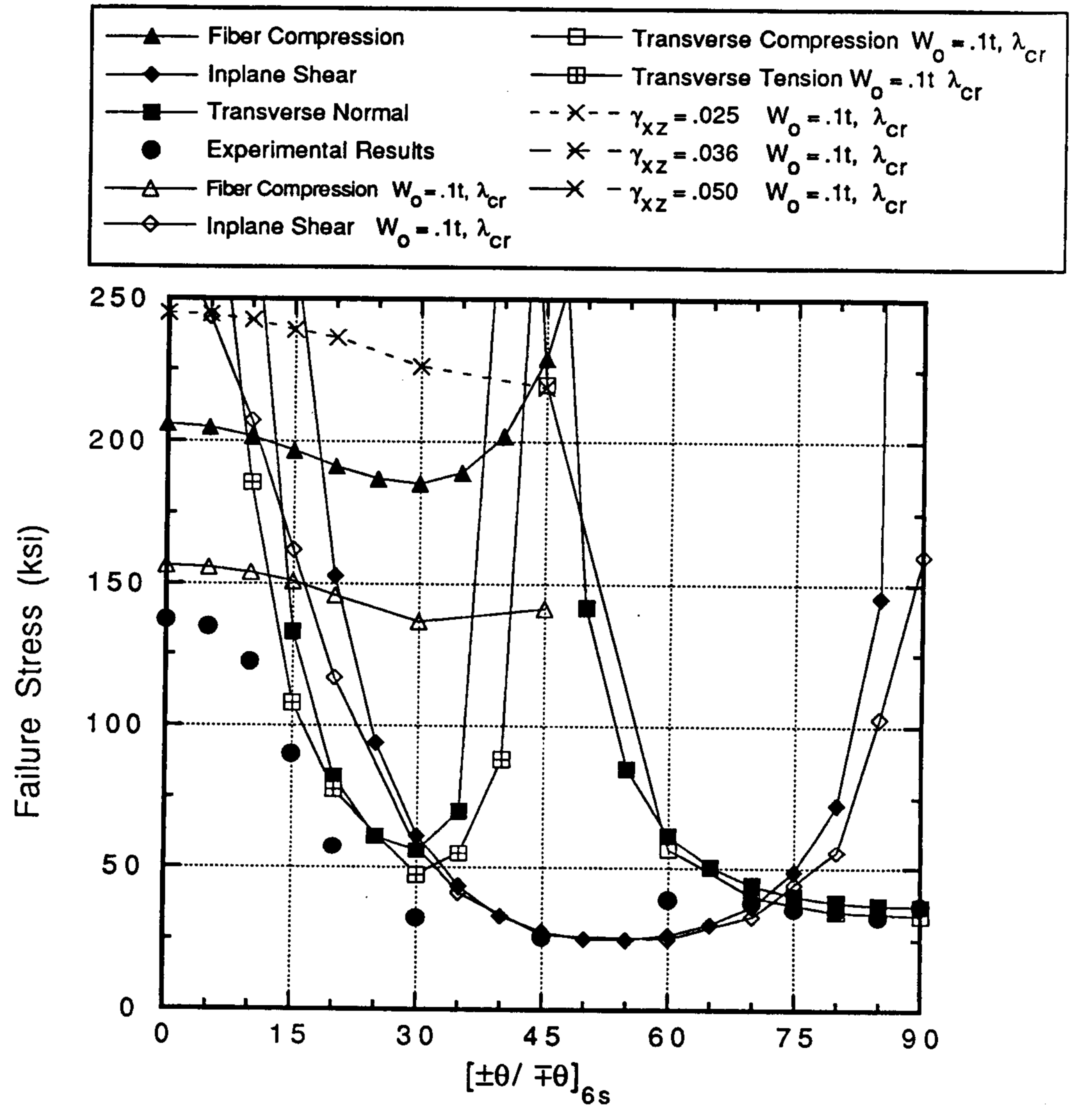

Figure 5.6 Comparison of nonlinear and classical predictions and experimental results for AS4/3502 with $W_o = 0.1t$ and $\lambda = \lambda_{cr}$.

figure 5.5 with figure 5.6 that at low off-axis angles failure due to interlaminar shear strain occurs at much higher loads for AS4/3502 than for IM7/8551-7a. Failure due to inplane shear also occurs at a much higher loads for low angles.

At 0° the failure load due to fiber compression as predicted by the nonlinear theory is about 156 ksi. This compares to a strength of 206 ksi predicted by the classical theory and a experimentally measured strength of approximately 137 ksi. The failure load due to the fiber compression mode as predicted by the nonlinear theory for AS4/3502 at this imperfection level does not decrease as much as the predicted load did for IM7/8551-7a at the same 0° off-axis angle and imperfection level. It appears that the imperfection sensitivity of a laminate may vary according to its elastic properties. Also, the AS4/3502 laminate does not seem to be sensitive to the imperfection for off-axis angles greater than about 40°. The failure loads due to the inplane transverse tension failure mode, using the nonlinear theory, show the same trends as those represented in figure 5.5. However the reduction relative to the classical values does not seem to be as large.

5.2.2 Results with $W_0 = 0.2t$ and $\lambda = \lambda_{cr}$

In figure 5.7 predictions from the nonlinear analysis are compared to experimental results and classical predictions for IM7/8551-7a. For the results shown in figure 5.7 the nonlinear analysis uses critical half-wavelengths and an imperfection amplitude of 0.2t. The various symbols and what they represent are identical to the situation of the last two figures. The failure modes predicted for the analyses in figure 5.7 are: fiber compression or interlaminar shear, if one uses the lower value of $\gamma_{xz}^{max} = 0.025$, for θ ranging from 0° to approximately 13°; inplane transverse tension for θ ranging from 13° to approximately 35°; inplane shear for θ ranging from 35° to 70°, and; transverse compression for θ ranging from

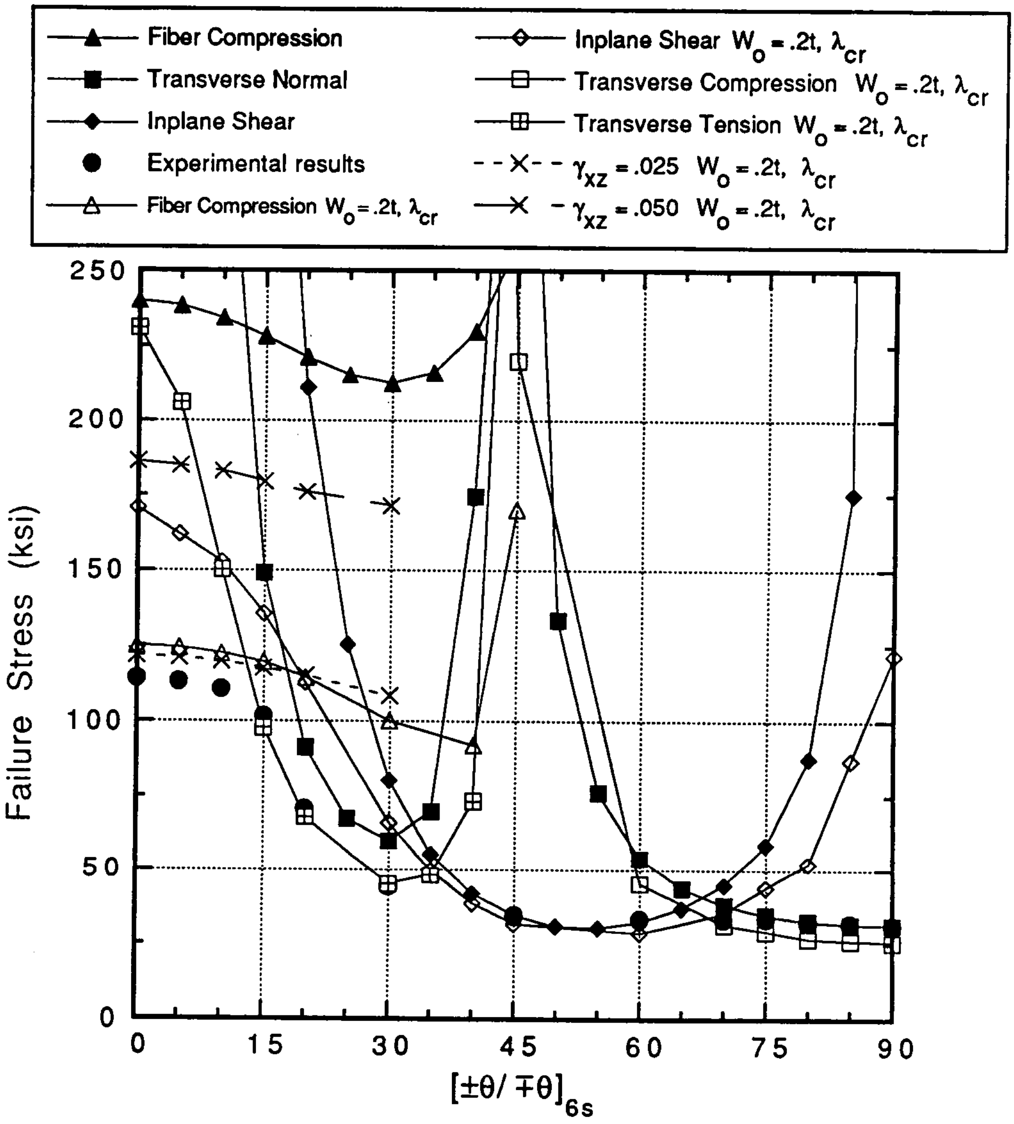

Figure 5.7 Comparison of nonlinear and classical predictions and experimental results for IM7/8551-7a with $W_o = 0.2t$ and $\lambda = \lambda_{cr}$.

70° to 90°.

The imperfection amplitude for the analyses presented in figure 5.7 is double that of figure 5.5. At an off-axis angle of 0° the predicted failure load from the nonlinear analysis for fiber compression is about 125 ksi compared to 155 ksi for figure 5.5 and 240 ksi for the classical (flat) case. Obviously there is not a linear relationship between predicted fiber compression strength and imperfection amplitude. This reflects on the nonlinear nature of the problem. In addition, the increased imperfection amplitude reduces the predicted compressive strength due to interlaminar shear by a greater amount than it does for fiber compression failure. If this trend with increased amplitude continues, it would appear that at a large enough imperfection amplitude interlaminar shear would become the dominant failure mechanism for θ in the range of 0° to 20°. As the imperfection amplitude increases, it also appears as if the locus due to inplane shear failure is moving down and to the left away from the locus predicted by classical theory for inplane shear. The failure loads due to inplane transverse tension, as predicted by the nonlinear theory, are now lower than experimentally observed values for $\theta = 15°$ to $\theta = 30°$. If this pattern continues, it appears that for more severe imperfections the nonlinear theory will predict failure loads due to inplane transverse tension that are considerably lower than experimental values. The imperfection has affected the inplane transverse tension failure mode to the degree that for a unidirectional laminate as modeled in figure 5.7, the predicted failure load due to inplane transverse tension is approximately 230 ksi, rather than infinity as it is for the classical theory. For θ greater than approximately 40° the nonlinear analysis is predicting failure loads due to inplane shear, and transverse compression, that are lower than experimentally observed.

Figure 5.8 compares predictions from the nonlinear theory with experimental results and classical predictions for AS4/3502. For the results shown in figure 5.8 the nonlinear

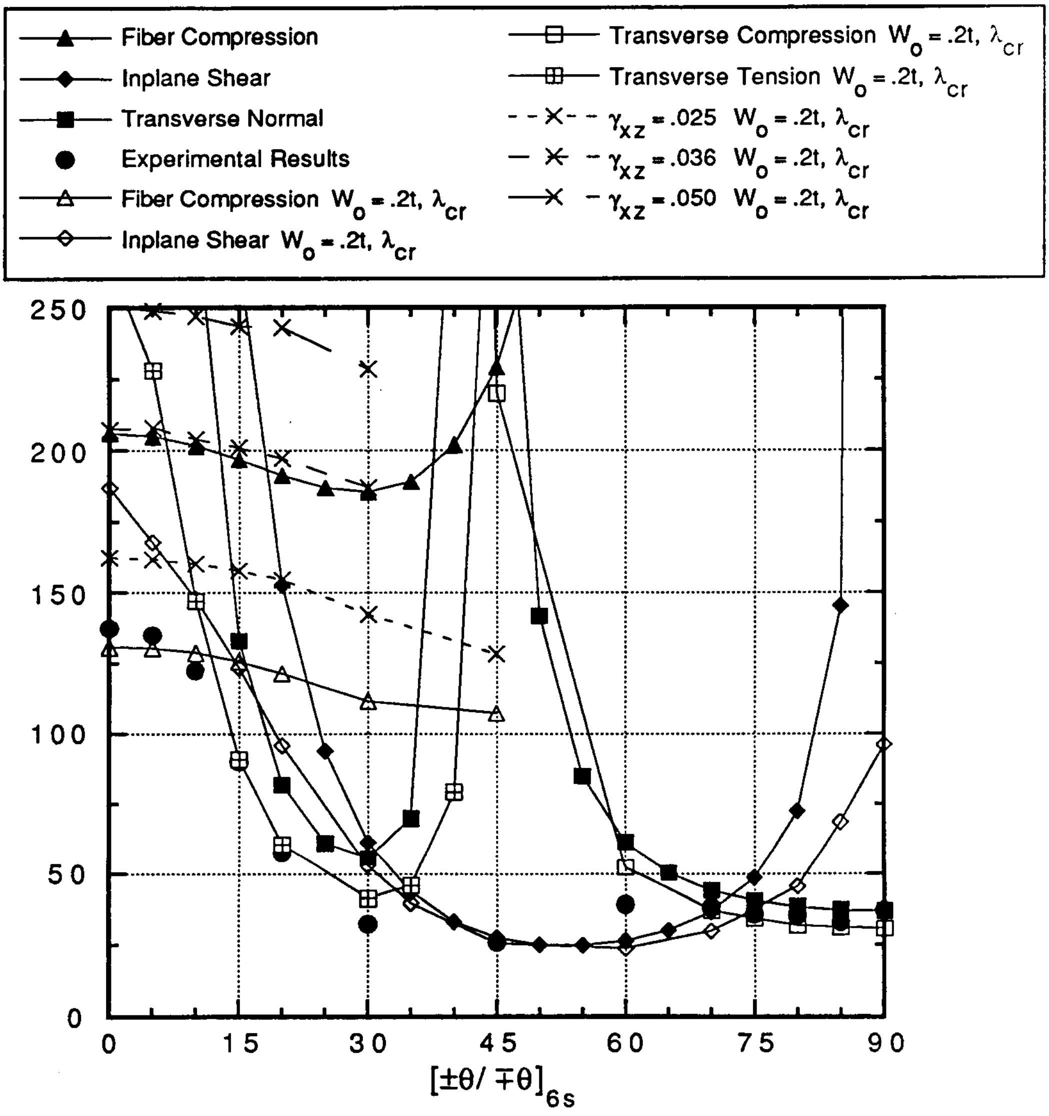

Figure 5.8 Comparison of nonlinear and classical predictions and experimental results for AS4/3502 with $W_o = 0.2t$ and $\lambda = \lambda_{cr}$.

analysis uses critical half-wavelengths and an imperfection amplitude of 0.2t. The predicted failure modes of AS4/3502 laminates with imperfections of $W_0 = 0.2t$ and $\lambda = \lambda_{cr}$ are: fiber compression for θ ranging from 0° to approximately 12°; inplane transverse tension for θ ranging from 12° to approximately 35°; inplane shear for θ ranging from 35° to approximately 75°, and; transverse compression for θ greater than 75°. The predicted compression strength due to the fiber compression mode is somewhat less than the experimental results. Assuming $\gamma_{xz}^{max} = 0.036$, for off-axis angles less than about 10° failure due to the interlaminar shear strain mode would occur at a compressive load of 210 ksi at $\theta = 0^\circ$ and then decrease to less than 200 ksi at 20°. The failure load due to this mode is higher than the failure load due to the inplane shear mode, a mode which starts at about 185 ksi at $\theta = 0^\circ$ and drops quite rapidly to 26 ksi at $\theta = 45^\circ$. The failure load due to the interlaminar shear strain mode is also slightly higher than the failure load due to fiber compression based on the classical analysis. It appears then, for this level of imperfection, that AS4/3502 angle-ply laminates with off-axis angles less than 10° will not fail due to interlaminar shear. For θ ranging from 12° to 30° the predicted failure loads due to inplane transverse tension using the nonlinear theory correlate quite closely with experimental results. Again, for off-axis angles greater than 40° the nonlinear analysis gives conservative estimates for compression strength.

5.2.3 Results with $W_0 = 0.5t$ and $\lambda = \lambda_{cr}$

Figure 5.9 compares predictions from the nonlinear analysis using critical half-wavelengths and an imperfection amplitude of 0.5t with experimental results and classical predictions for IM7/8551-7a. The imperfection amplitude of 0.5 times a layer thickness is the most severe considered so far. This level of imperfection severely, and perhaps unrealisti-

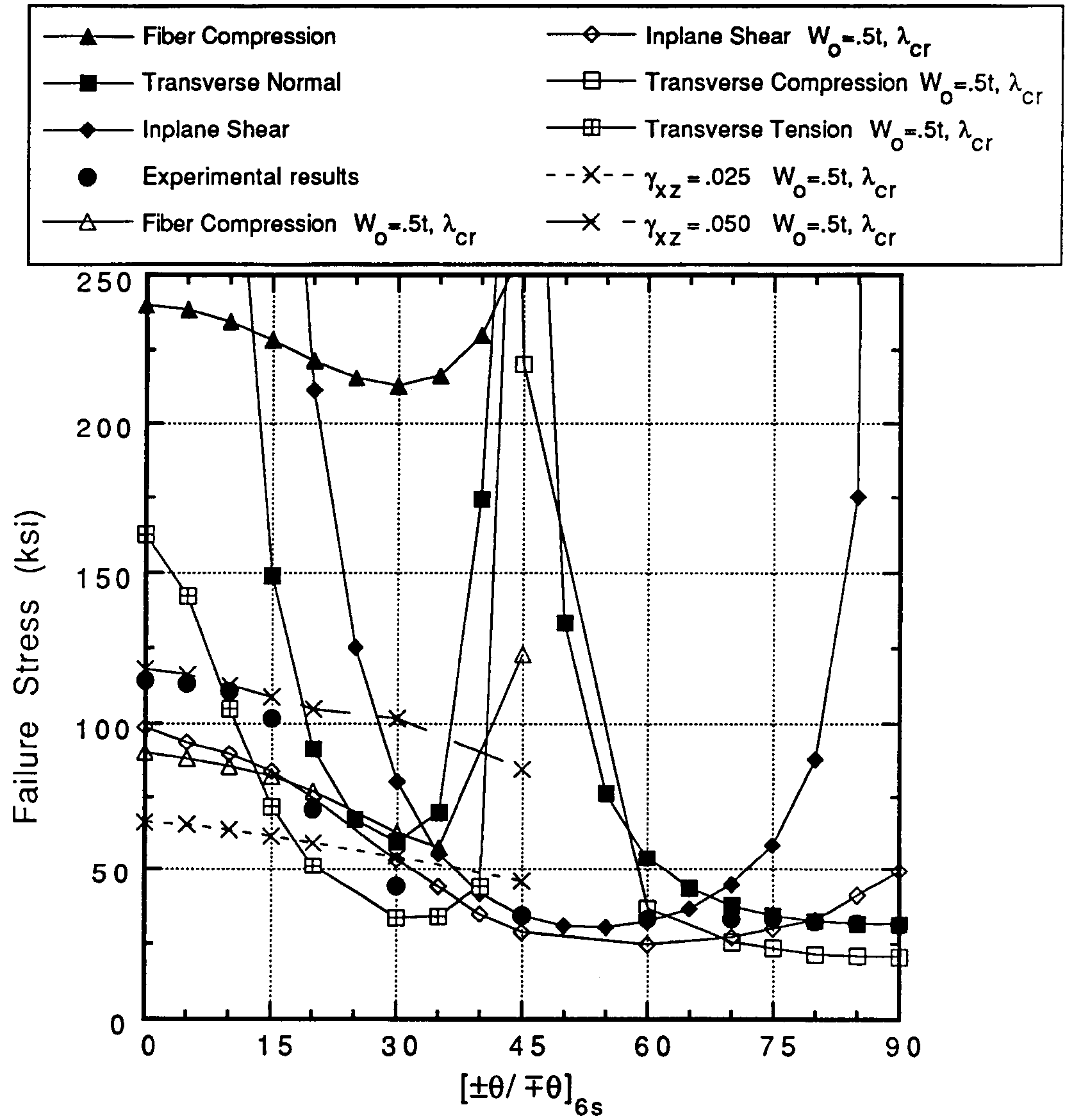

Figure 5.9 Comparison of nonlinear and classical predictions and experimental results for IM7/8551-7a with $W_0 = 0.5t$ and $\lambda = \lambda_{cr}$.

cally affects the predicted compression strength of the IM7/8551-7a angle-ply laminates.

A point not discussed yet is the fact that as the off-axis angle θ increases, the critical half-wavelength decreases. This was shown in figure 5.3 and Table 5.3. For a given imperfection amplitude, W_0, a shorter half-wavelength results in higher curvatures in the imperfection. For a given applied load these higher curvatures lead to higher stresses in the plane of the layer and higher interlaminar strains. Thus for a given imperfection amplitude the shorter half-wavelength produces a more severe imperfection. Correspondingly, it reduces laminate strength more. So for figure 5.9 and the past figures, the relative severity of the imperfection analyzed increases as the off-axis angle θ increases. This could explain why for θ from about 40° to 90° the nonlinear theory predicts lower failure loads than measured experimentally. This will be discussed more and examples will be given in the next section.

Ignoring in figure 5.9 the case of $\gamma_{xz}^{max} = 0.025$, the predicted failure modes of IM7/8551-7a with $W_0 = 0.5t$ and $\lambda = \lambda_{cr}$ are: either fiber compression or inplane shear for θ ranging from 0° to 15°; inplane transverse tension for θ ranging from 15° to approximately 38°; inplane shear for θ ranging from 38° to 70°, and; transverse compression for θ greater than 70°. From $\theta = 0^\circ$ to about 15° the fiber compression and inplane shear modes are so close to each other that it is difficult to determine which actually causes failure. Both modes probably contribute to failure. If the failure value for interlaminar shear strain γ_{xz}^{max} were considered to be 0.025, then interlaminar shear would cause the laminate to fail at much lower loads than predicted for the fiber compression or inplane shear modes. From $\theta = 0^\circ$ to approximately 20° all predictions except the interlaminar shear failure associated with $\gamma_{xz}^{max} = 0.050$ are below experimental results. This would indicate that either the laminates tested do not have as severe an imperfection as those used in the predictions for figure 5.9, or $\gamma_{xz}^{max} = 0.050$ is the dominant failure condition, despite the fact there are other modes that lead to lower failure stresses.

Figure 5.10 contrasts predictions from the nonlinear analysis with experimental results and classical predictions for AS4/3502 using critical half-wavelengths and an imperfection amplitude of 0.5t. In almost every case the predictions from the nonlinear analysis in figure 5.10 give significantly lower failure loads than are actually experienced. Not considering the $\gamma_{xz}^{max} = 0.025$ locus, the predicted modes of failure are: fiber compression or inplane shear for θ ranging from 0° to 12°, with the emphasis on inplane shear; inplane transverse tension for θ ranging from 12° to approximately 36°; inplane shear for θ ranging from 36° to 75°, and; inplane transverse tension for θ ranging from 75° to 90°. In the range of $\theta = 0^\circ$ to $\theta = 15^\circ$, the interlaminar shear prediction locus for a $\gamma_{xz}^{max} = 0.036$ is also lower than experimental data. One startling observation that can be made regarding figures 5.9 and 5.10 is that a shear failure mode, either inplane or interlaminar shear, could conceivably constitute the major mode of failure for most of the range of θ. Also, the severe imperfection amplitude, coupled with nonlinear effects, is causing predicted failure loads due to inplane transverse tension to decrease significantly.

5.2.4 Discussion

From the last six figures many important facts were learned about the compressive failure of graphite-epoxy angle-ply laminates which have imperfections in the form of critical buckling half-wavelengths. Angle-ply laminates are not as imperfection-sensitive for off-axis angles of about 40° and greater. For off-axis angles less than about 35°, even a very small imperfection amplitude can have significant effect on the compressive strength of a laminate. The mode of failure can be strongly influenced by the level of imperfection. Generally the predicted compressive failure modes are: fiber compression for θ ranging from

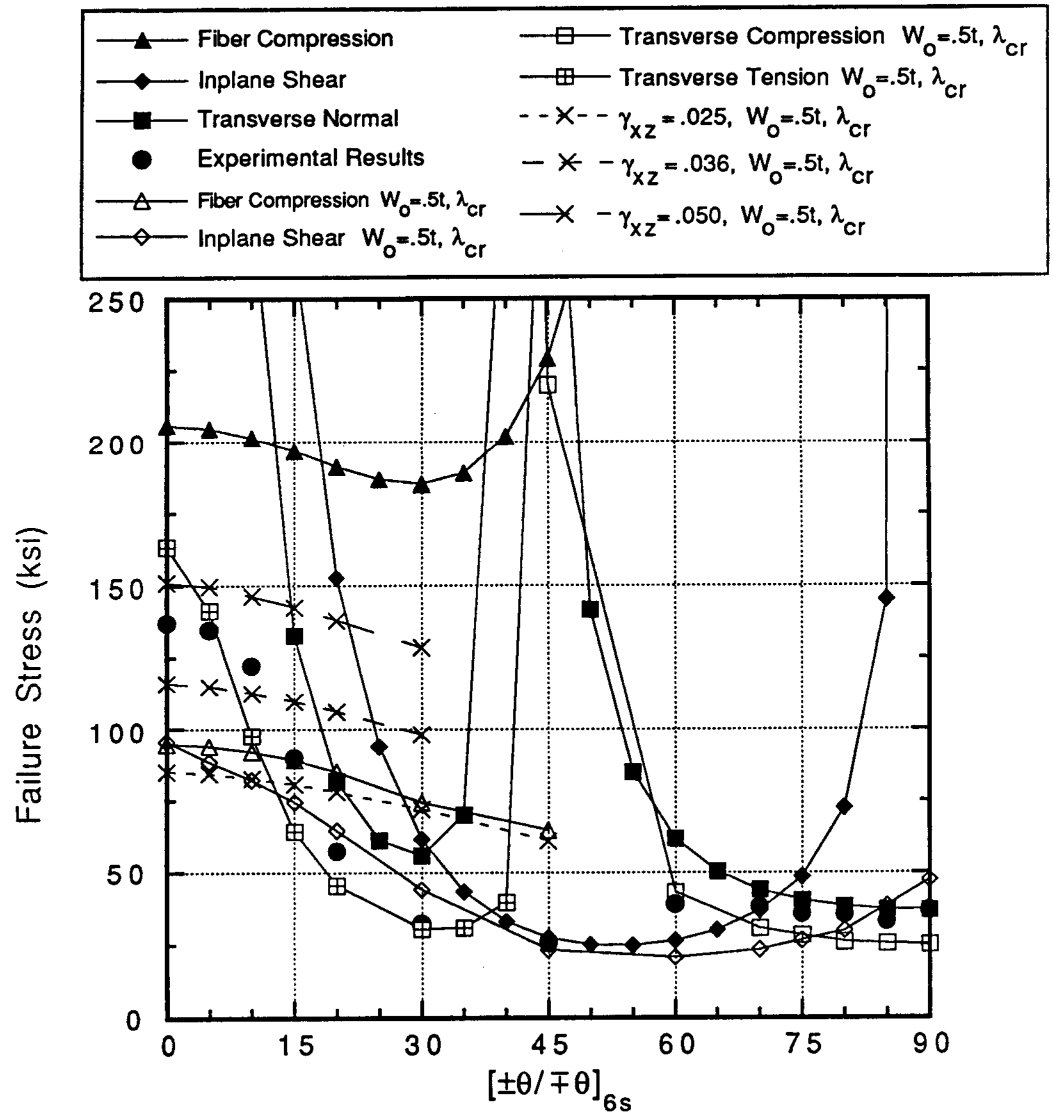

Figure 5.10 Comparison of nonlinear and classical predictions and experimental results for AS4/3502 with $W_o = 0.5t$ and $\lambda = \lambda_{cr}$.

0° to approximately 12°; inplane transverse tension for θ ranging from 12° to approximately 35°; inplane shear for θ ranging from 35° to 70°, and; transverse compression for θ greater than 70°. As the imperfection amplitude increases, i.e., $W_0 > 0.2t$, the compressive failure mode for θ ranging from 0° to 12° tends to be the inplane shear mode or the interlaminar shear mode. This is because the more severe imperfection amplitudes increases out-of-plane deflections at lower loads. The increasing out-of-plane deflections cause more load to be transferred within the laminate through shear. Thus for the most severe imperfection amplitude of 0.5t, the most dominant failure mechanism is shear. There may be several failure modes acting simultaneously and interacting to produce failure at low off-axis angles. As has already been discussed, for θ ranging from 40° to 90° the nonlinear theory consistently predicted failure loads that were too low.

Although IM7/8551-7a is stiffer and stronger in the axial direction than AS4/3502, the imperfections had a relatively greater impact on IM7/8551-7a. For example, at an off-axis angle of 0° the strength of IM7/8551-7a is 240 ksi if no imperfections are considered, i.e., the classic case. The experimentally observed strength is 114 ksi. For an imperfection of $W_0 = 0.1t$ and $\lambda = \lambda_{cr}$ the predicted strength is about 155 ksi, a decrease in strength of 85 ksi relative to the perfect case. However, for AS4/3502 at an off-axis angle of 0° the strength is 206 ksi if no imperfections are considered. The experimentally observed strength is 137 ksi, and for an imperfection of $W_0 = 0.1t$ and $\lambda = \lambda_{cr}$ the predicted strength is about 156 ksi, a decrease in predicted strength of 50 ksi. This indicates that AS4/3502 is less sensitive to imperfections at low off-axis angles than IM7/8551-7a. Likewise, for $\theta <$ 15° the experimental results for AS4/3502 are higher than the experimental results for IM7/8551-7a. The analyses using the more severe imperfections also support the assertion. Comparisons between material systems when considering the inplane transverse tension failure mode also show the same trend.

5.3 Using Other Half-Wavelengths as Imperfection Shapes

One of the concerns expressed in the last section is the fact that the critical half-wavelength decreases as the off-axis angle θ increases. Thus, for the analyses presented in the last section the imperfections analyzed at $\theta = 0^\circ$ are not geometrically the same ones that are analyzed at $\theta = 20^\circ$. This section will consider failure of angle-ply laminates which contain imperfections, but the geometry of the imperfections will be independent of θ.

5.3.1 Source of Half-Wavelengths and Imperfection Amplitudes

In chapter 2 it was shown that wavy-type imperfections were observed in scraps left over from the IM7/8551-7a test specimens. The wavy imperfections had lengths of 9 to 17 times a layer thickness. The amplitudes of the imperfections were from 0.2 to 0.5 times a layer thickness. The analyses in the previous section indicated that an imperfection amplitude of 0.5 times a layer thickness, or $W_0 = 0.5t$, predicted considerably lower failure loads than observed experimentally. Reasonable imperfection amplitudes were considered to be $W_0 = 0.1t$ and $0.2t$. Based on these considerations, the next sections discuss the predicted failure characteristics for two imperfection amplitudes, $W_0 = 0.1t$ and $0.2t$, and two wavelengths, $\lambda = 10t$ and $20t$. Both material systems are considered and comparisons with experimental observations are made.

5.3.2 Results with $W_0 = 0.1t$ and $\lambda = 20t$

In figure 5.11 compressive failure predictions based on the nonlinear theory with an imperfection of $W_0 = 0.1t$ and $\lambda = 20t$, where $t = 0.00573$ in., experimental results, and failure predictions based on the classical theory are shown for IM7/8551-7a. The symbols are the

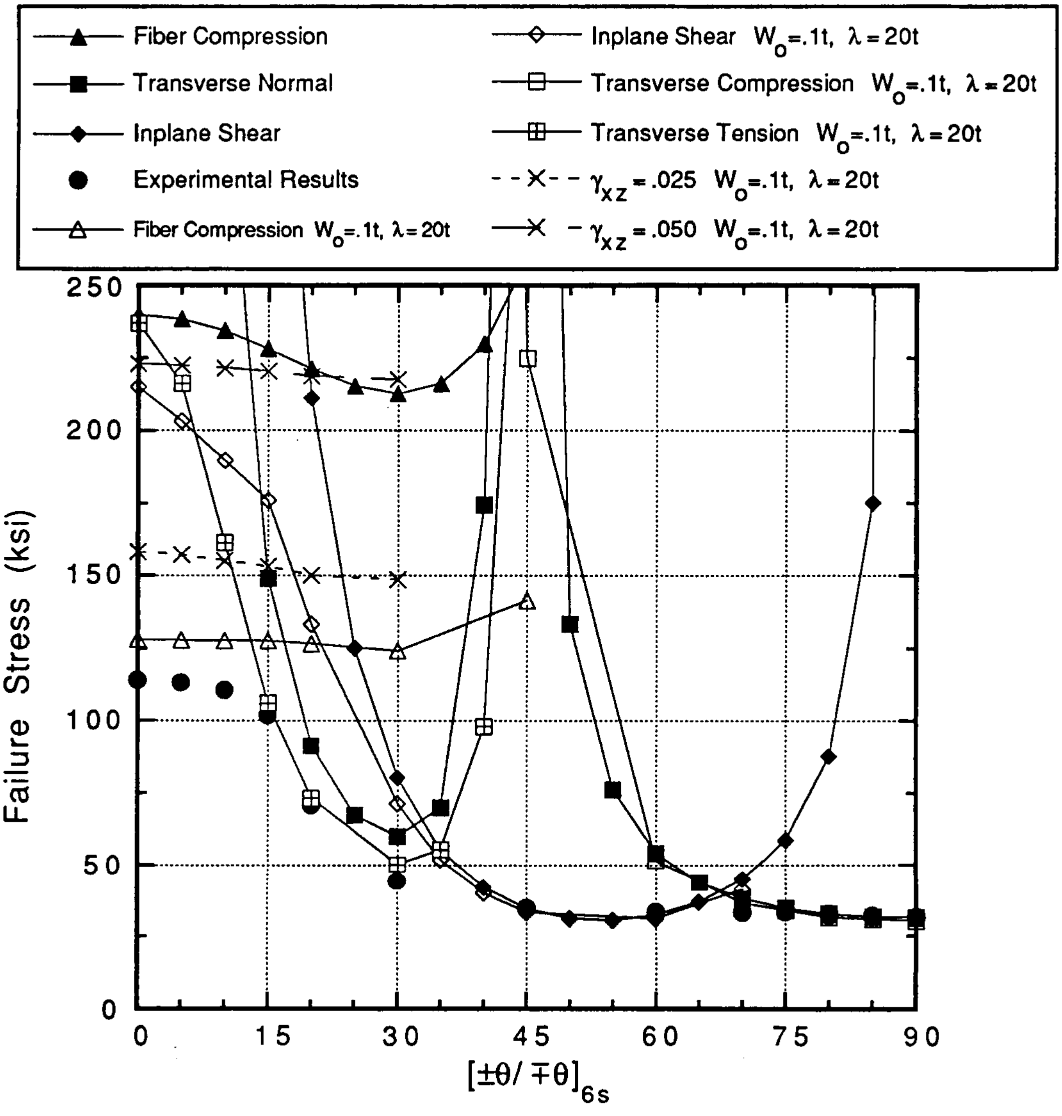

Figure 5.11 Comparison of nonlinear and classical predictions and experimental results for IM7/8551-7a with $W_0 = 0.1t$ and $\lambda = 20t$.

same as in previous figures. The filled circles represent experimental results. The filled triangles represent fiber compression failure using classical theory with the maximum stress failure criterion. The filled diamonds represent inplane shear failure, using classical theory, and the filled squares represent transverse normal failure, using classical theory, which includes both inplane transverse tension at off-axis angles less than 45° and transverse compression at off-axis angles greater than 45°. The open triangles, diamonds, and squares represent the same failure modes as the closed triangles, diamonds, and squares, but use the nonlinear analysis to compute fiber, transverse, and shear stresses, and the resulting failure loads. The x's with the short and long dashes, respectively, represent the interlaminar shear strain γ_{xz} at levels of 0.025 and 0.050.

Predicated on the results in the figure, the predicted failure modes are: fiber compression for $\theta = 0°$ to 15°; inplane transverse tension for $\theta = 15°$ to approximately 35°; inplane shearing for $\theta = 35°$ to approximately 70°, and; transverse compression for $\theta = 70°$ to 90°. For off-axis angles less than 20° failure due to interlaminar or inplane shear would occur at much higher loads than failure due to fiber compression. The character of the inplane shear mode has changed significantly relative to using the classical theory. The inplane shear failure mode now predicts a finite strength at $\theta = 0°$ compared to an infinite strength using classical predictions. The inplane transverse tension failure mode shows similar trends concerning the prediction of failure strength at $\theta = 0°$. Recall figure 5.5 shows predictions for IM7/8551-7a with $W_0 = 0.1t$. However, the wavelength changes with θ in that figure. At low off-axis angles, λ_{cr} in figure 5.5 is larger than the imperfection length used in figure 5.11 (see Table 5.3). The results of figure 5.11, then, show that shorter wavelengths lead to reduced strength at low off-axis angles. For θ ranging from 0° to 20° in figure 5.11, the predicted compression strength, which is due to the fiber compression mode, stays virtually constant. This contrasts with figure 5.5 where the predicted compression strength, which is also due to the fiber compression mode, decreases slightly for $\theta = 5^\circ$ to $\theta = 10^\circ$. This effect is probably due to λ_{cr} decreasing with θ in the results of figure 5.5. In figure 5.11, for $\theta = 40^\circ$ and higher, the nonlinear theory predicts failure loads almost identical to experimental results.

Figure 5.12 compares failure predictions based on the nonlinear theory, experimental results, and failure predictions based on the classical theory for AS4/3502. The nonlinear theory uses an imperfection of $W_0 = 0.1t$ and $\lambda = 20t$ where t = 0.0052 in. The predicted failure modes are: fiber compression for $\theta = 0^\circ$ to 12°; inplane transverse tension for $\theta = 12^\circ$ to approximately 33°; inplane shear for $\theta = 33^\circ$ to approximately 70°, and; transverse compression for $\theta = 70^\circ$ to 90°. These are the same failure mode characteristics as observed in figure 5.11 for IM7/8551-7a. However, at low off-axis angles, predictions based on the nonlinear analysis for the IM7/8551-7a material system continue to be relatively lower than their counterparts for the AS4/3502 material system for the same imperfection level. In figure 5.12 the predicted failure loads due to the fiber compression failure mode coincide very well with experimental data for about the first 10°. Although the character of the inplane shear failure mode has changed from the classical case, it does not follow the experimental results until approximately $\theta = 40^\circ$. The predicted failure loads resulting from the inplane transverse tension mode, using the nonlinear theory, have moved somewhat closer to the experimentally observed results, though they are still too high. The failure loads predicted for an interlaminar shear strain $\gamma_{xz}^{max} = 0.036$ are considerably higher than the classical predictions. It appears that this level of waviness affects the fiber compression and inplane transverse tension modes more than the interlaminar shear and inplane shear modes. In all figures showing the predictions from the nonlinear analysis and predictions from classical

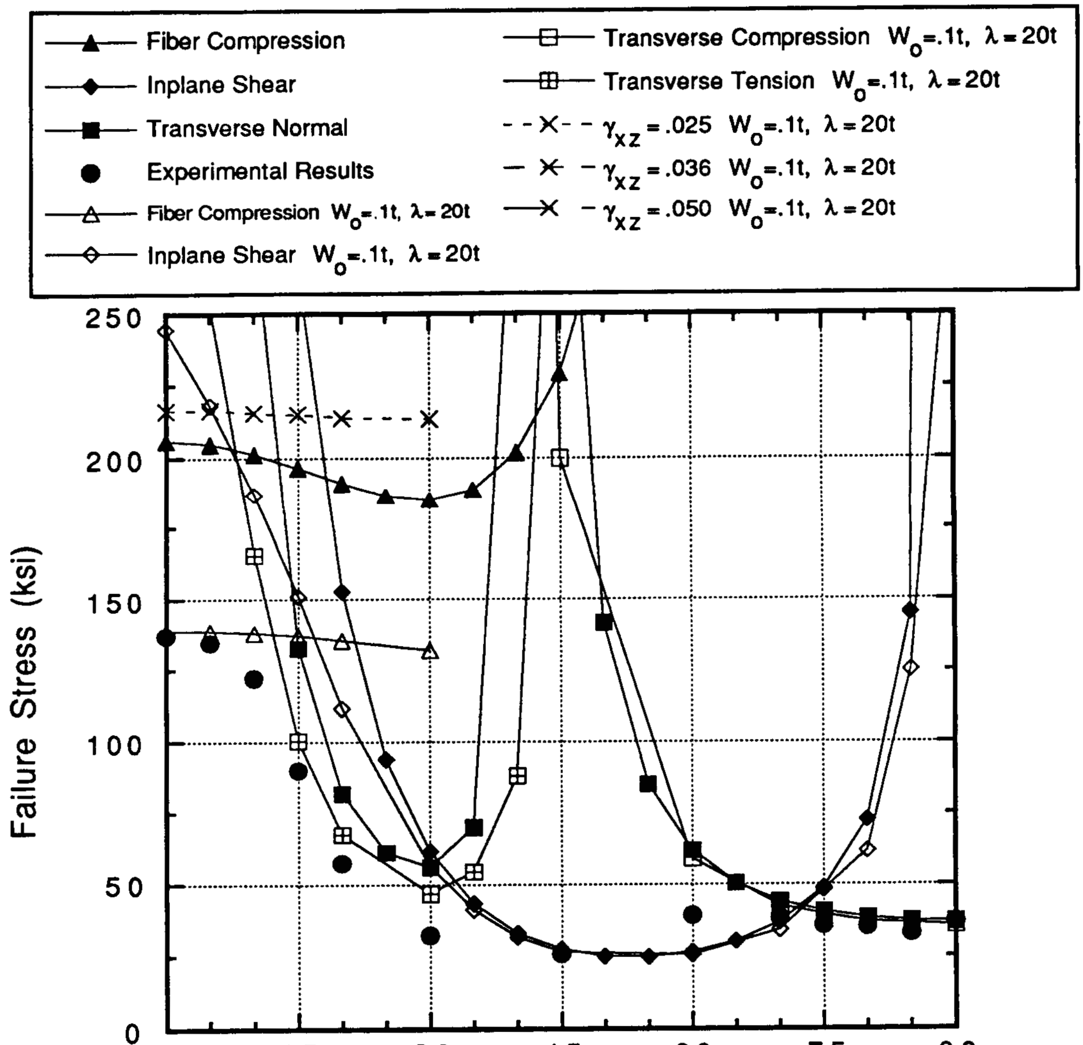

Figure 5.12 Comparison of nonlinear and classical predictions and experimental results for AS4/3502 with $W_0 = 0.1t$ and $\lambda = 20t$.

theory for AS4/3502, neither prediction correctly follows experimental results from approximately 60° to 70°. It almost appears as if the loci representing the predictions have been shifted 10° to the right.

5.3.3 Results with $W_0 = 0.1t$ and $\lambda = 10t$

Failure predictions based on the nonlinear theory for the case with $W_0 = 0.1t$ and $\lambda = 10t$ for IM7/8551-7a are shown in figure 5.13. For this case the half-wavelength is 50% of the half-wavelength in figure 5.11. Note the downward trend of all the failure loci associated with the nonlinear analysis. The shortening of the wavelength seems to have a serious impact on strength. The predicted failure modes are: fiber compression for $\theta = 0°$ to approximately 15°; inplane transverse tension for $\theta = 15°$ to approximately 35°; inplane shear for $\theta = 35°$ to approximately 65°, and; inplane transverse tension for $\theta = 65°$ to 90°. Failure due to the fiber compression and inplane transverse tension modes are predicted to occur at very low loads relative to classical predictions. In addition, there are other significant changes in the failure predictions. The reduced imperfection length also decreased angle-ply compression strength due to the interlaminar shear mode. The locus predicting inplane shear is shifted further to the left. For $\theta > 40°$ failure loads lower than experimentally observed values are predicted due to inplane shear and due to transverse compression.

The failure predictions using the nonlinear theory for AS4/3502 with $W_0 = 0.1t$ and $\lambda = 10t$ are graphically depicted in figure 5.14. The character of the predictions in figure 5.14 are similar to those in figure 5.13. However, the failure loads resulting from the fiber compression mode and interlaminar shear mode aren't as low as their counterparts for IM7/8551-7a shown in figure 5.13. The predicted compressive failure modes are: fiber compression for $\theta = 0°$ to approximately 13°; inplane transverse tension for $\theta = 13°$ to approximate-

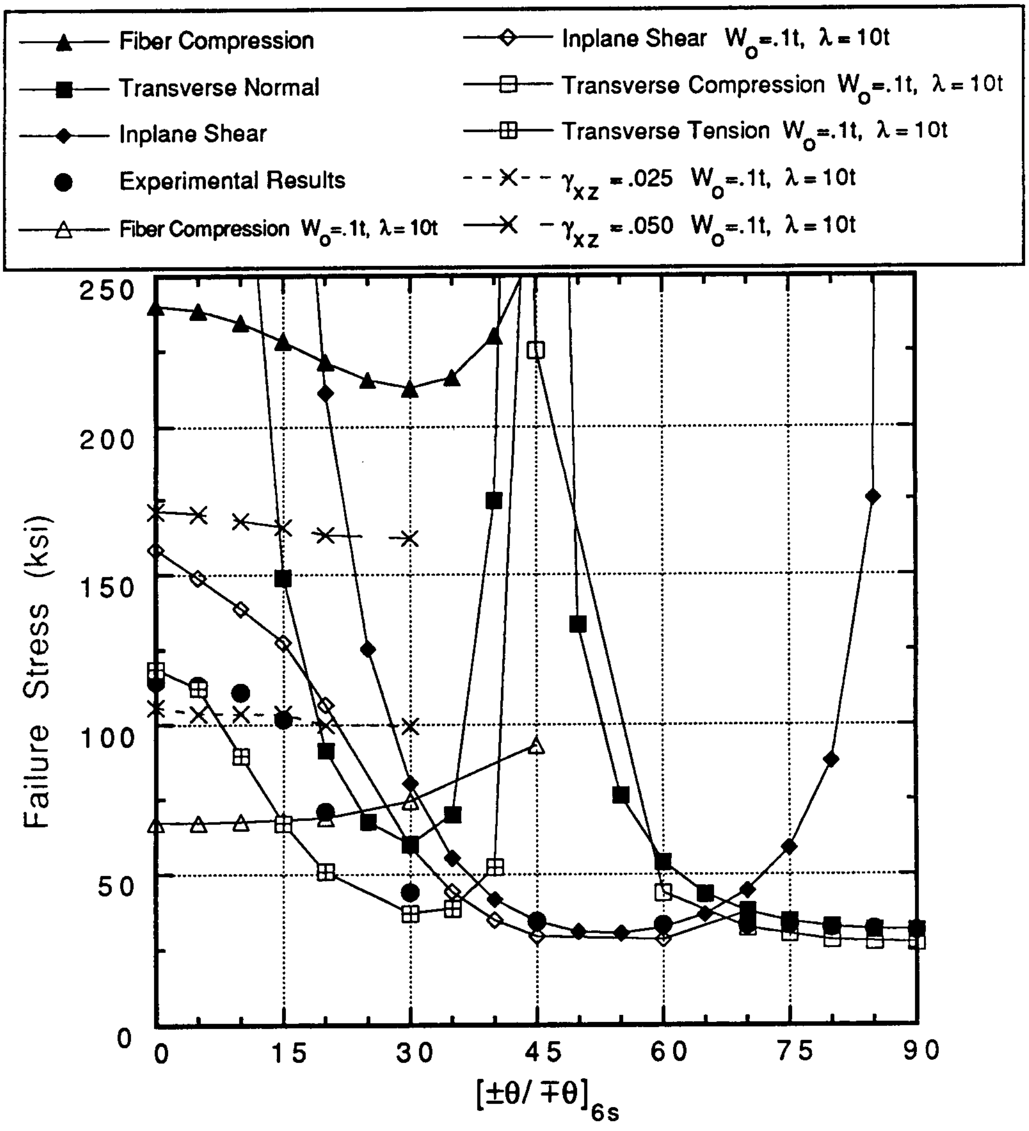

Figure 5.13 Comparison of nonlinear and classical predictions and experimental results for IM7/8551-7a with $W_0 = 0.1t$ and $\lambda = 10t$.

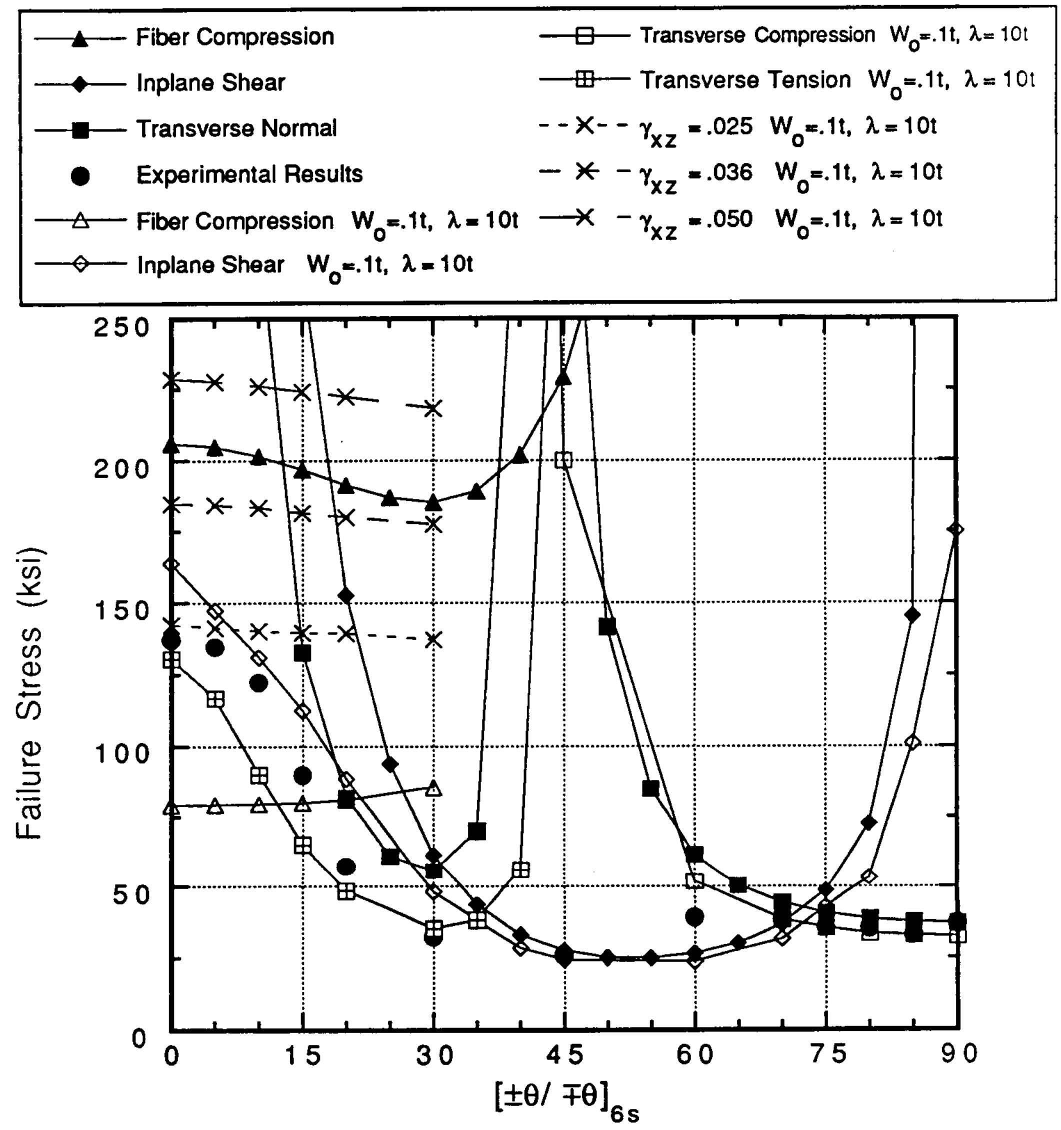

Figure 5.14 Comparison of nonlinear and classical predictions and experimental results for AS4/3502 with $W_0 = 0.1t$ and $\lambda = 10t$.

ly 35°; inplane shear for $\theta = 35^\circ$ to approximately 75°, and; transverse compression for $\theta = 75^\circ$ to 90°. Compared to figure 5.12, the shorter imperfection length seems to greatly affect the inplane transverse tension mode. In figure 5.14 the predicted failure loads for $\theta < 30^\circ$ due to inplane transverse tension are all lower than experimental values. As mentioned with previous figures, since the predicted compression strengths due to the fiber compression failure mode are much lower than measured results for low off-axis angles, it would appear that the laminate did not fail in the fiber compression mode. Alternately, it may be that laminate imperfections were not as severe as analyzed. The interlaminar shear failure mode using $\gamma_{xz}^{max} = 0.036$ predicts larger loads than the fiber compression mode, the inplane transverse tension mode, or the inplane shear mode.

5.3.4 Results with $W_0 = 0.2t$ and $\lambda = 20t$

In figure 5.15 the failure predictions using the nonlinear theory are shown for the case of $W_0 = 0.2t$ and $\lambda = 20t$ and the IM7/8551-7a material system. Much can be learned by comparing the predictions in this figure with those shown in figure 5.13. Some researchers[17] use a non-dimensional ratio to uniquely describe the level of imperfection in their laminates. This ratio is usually defined as

$$I_r = W_0/\lambda_{cr}. \tag{5.1}$$

Using numerical values, I_r should be 0.01 for the results in figures 5.13 and 5.15. Accordingly, these figures should exhibit the same predictions. They do not. The present analyses thus show that a single parameter such as this ratio can be misleading. In figure 5.15 the predicted compressive strength due to fiber compression at low off-axis angles is higher than the predicted compressive strength due to fiber compression in figure 5.13. Also, for

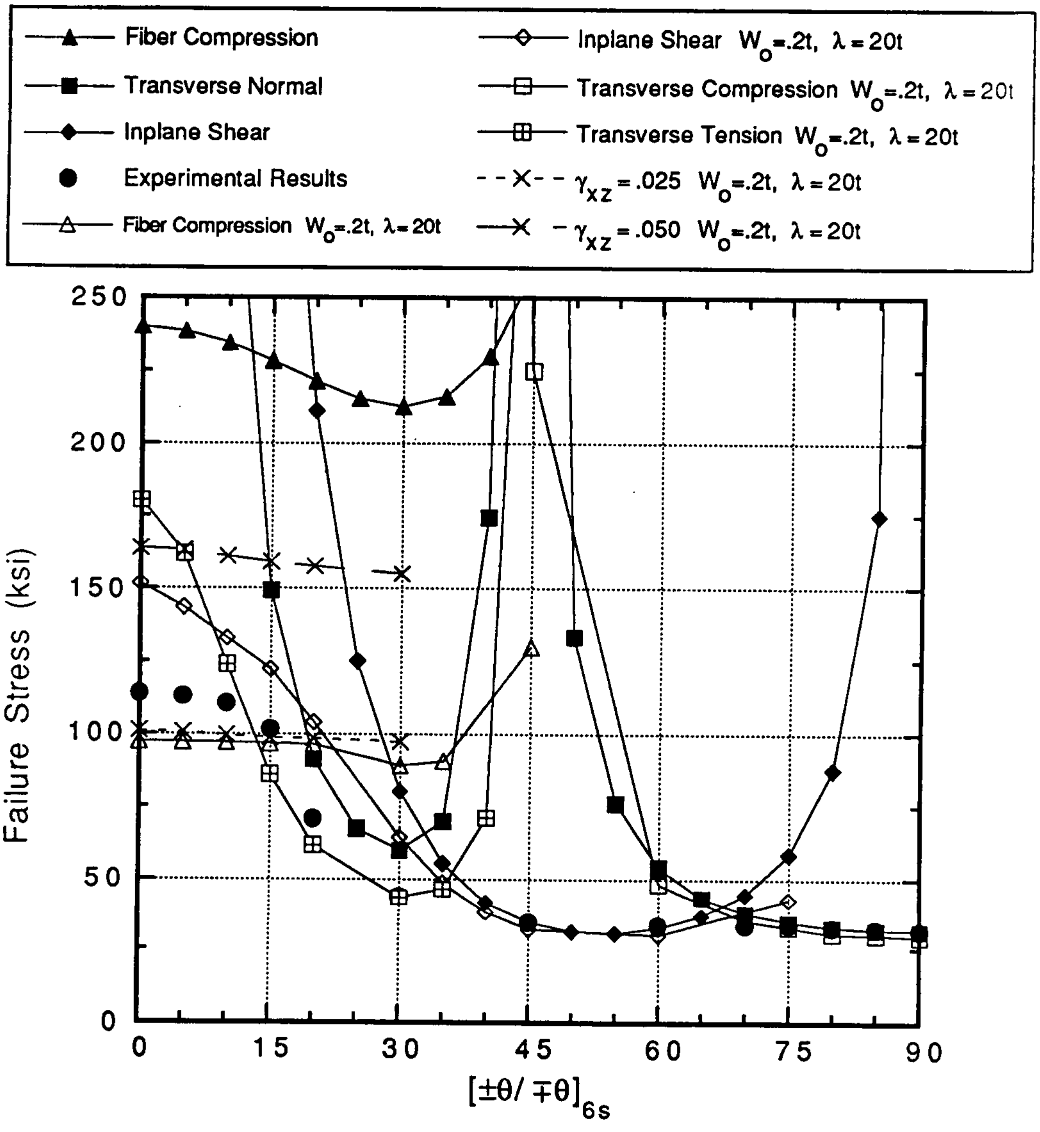

Figure 5.15 Comparison of nonlinear and classical predictions and experimental results for IM7/8551-7a with $W_0 = 0.2t$ and $\lambda = 20t$.

off-axis angles less than 30° the compression strengths due to inplane transverse tension are larger in figure 5.15 than in figure 5.13. The predictions for failure due to interlaminar shear and inplane shear are slightly lower in figure 5.15 than in figure 5.13. Considering, in addition, the predictions of figure 5.11, it appears the shorter imperfection length affects the fiber compression mode and the inplane transverse tension mode more than the larger imperfection amplitude does. However, comparing figure 5.13 with figure 5.15, it appears the larger imperfection amplitude has only a slightly greater affect on the interlaminar shear and inplane shear failure modes than the short imperfection length does. Thus the ratio I_r perhaps has only limited meaning for the interlaminar shear and inplane shear modes.

Turning to the details of figure 5.15, the predicted failure modes are: fiber compression for $\theta = 0°$ to 15°; inplane transverse tension for $\theta = 15°$ to approximately 35°; inplane shear for $\theta = 35°$ to approximately 67°, and; transverse compression for $\theta = 67°$ to 90°. When considering all failure modes, the predicted modes and failure loads presented in figure 5.15, although slightly low, are the nearest to the experimental results of any discussed so far. Note that the interlaminar shear failure mode for $\gamma_{xz}^{max} = 0.025$ and the fiber compression mode coincide for $\theta = 0°$ to 15°.

In figure 5.16 the predictions from the nonlinear analysis with $W_0 = 0.2t$ and $\lambda = 20t$ and the AS4/3502 material system are shown. Relative to the results in figure 5.14, the same observations made about the imperfection ratio I_r in the previous section, these observations related to figures 5.15 and 5.13, also apply. At low off-axis angles there are significant differences between the predicted loads due to the fiber compression and inplane transverse tension modes in figure 5.16 compared to the loads of figure 5.14, detracting from the single ratio theory. However, the failure loads due to the interlaminar shearing mode and inplane shear mode are approximately the same in figure 5.14 as in figure 5.16.

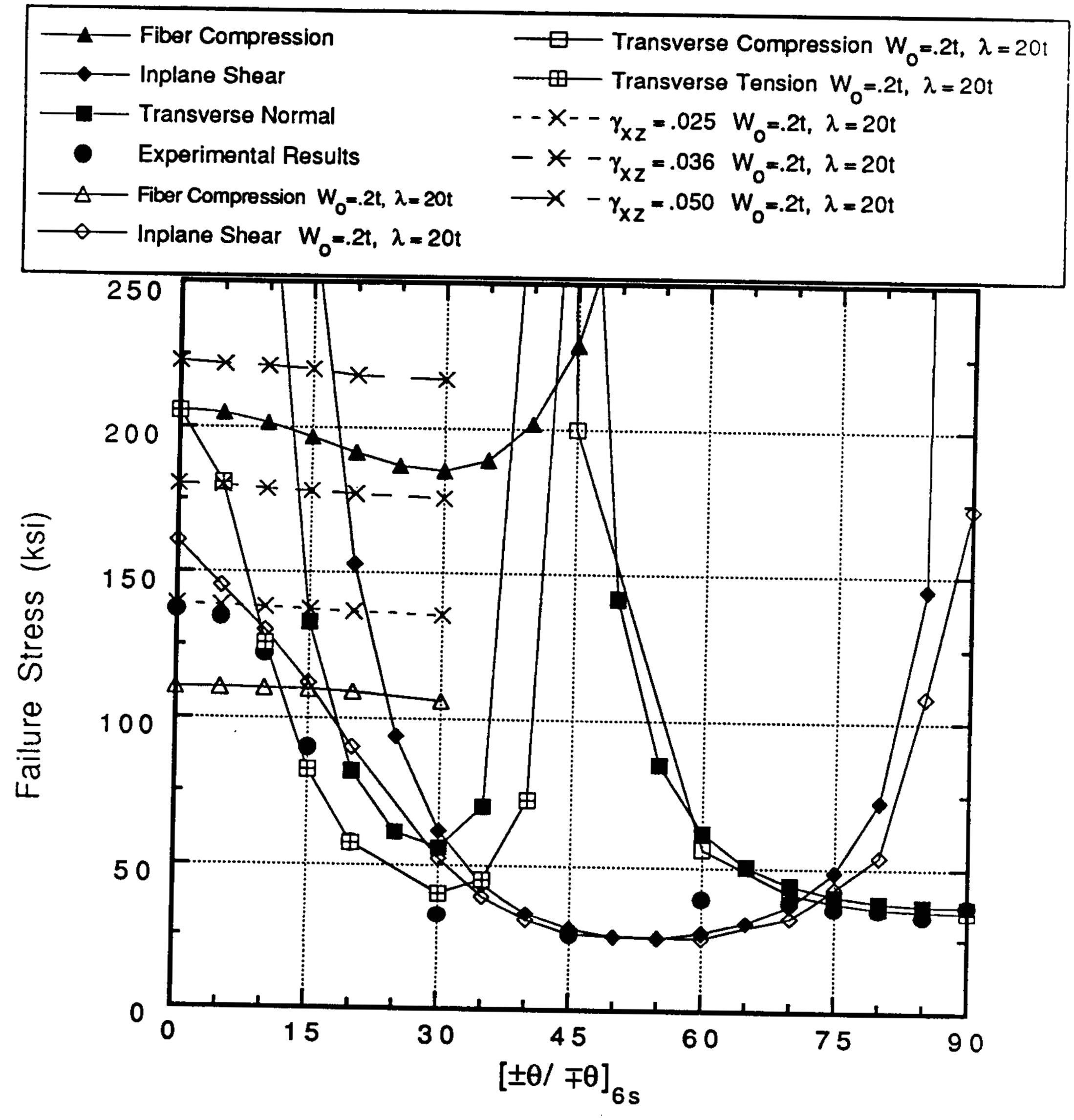

Figure 5.16 Comparison of nonlinear and classical predictions and experimental results for AS4/3502 with $W_o = 0.2t$ and $\lambda = 20t$.

The predicted failure modes in figure 5.16 are: fiber compression for $\theta = 0^\circ$ to approximately 12°; inplane transverse tension for $\theta = 12^\circ$ to approximately 34°; inplane shear for $\theta = 34^\circ$ to approximately 75°, and; transverse compression for $\theta = 75^\circ$ to 90°. The fiber compression mode again predicts low failure loads when compared to experimental results. However, the failure loads due to the inplane transverse tension mode shows excellent correlation with experiments for $\theta = 10^\circ$ to 30°. The predicted interlaminar shear mode $\gamma_{xz}^{max} = 0.036$ at low off-axis angles results in considerably higher failure strengths than the predicted fiber compression and inplane shearing modes do. In addition, the interlaminar shear mode leads to higher strengths than the experimental results. Even though it was learned in section 5.2 that larger imperfection amplitudes seem to affect interlaminar shear somewhat more than fiber compression, considering $\gamma_{xz}^{max} = 0.05$ for IM7/8551-7a, and $\gamma_{xz}^{max} = 0.036$ for AS4/3502, it does not appear that the present combination of imperfection amplitude and length have influenced interlaminar shear, enough to cause it to be a dominant failure mode in figures 5.15 and 5.16.

5.3.5 Results with $W_0 = 0.2t$ and $\lambda = 10t$

The predictions presented in figure 5.17 represent the most severe of the four imperfection cases, namely that of $W_0 = 0.2t$ and $\lambda = 10t$ with the IM7/8551-7a material system. All predictions but the high interlaminar shear mode with $\gamma_{xz}^{max} = 0.05$ and a portion of the inplane shear mode underestimate the failure loads. The failure modes as predicted by the nonlinear theory are: fiber compression for $\theta = 0^\circ$ to 15°; inplane transverse tension for $\theta = 15^\circ$ to approximately 40°; inplane shear for $\theta = 40^\circ$ to approximately 70°, and; transverse compression for $\theta = 70^\circ$ to 90°. The low predicted failure loads result from the short imperfection length aggravating the fiber compression and transverse modes. The interlami-

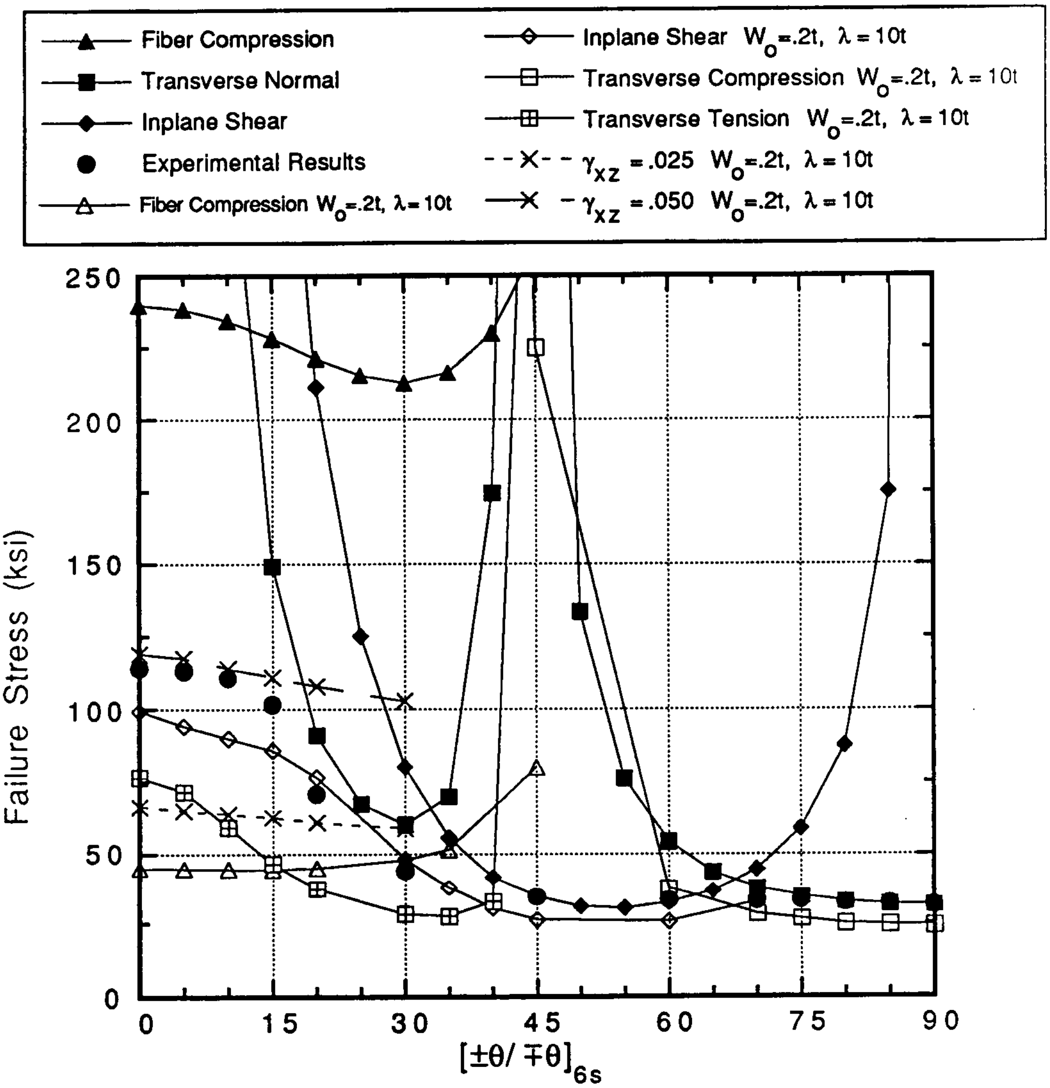

Figure 5.17 Comparison of nonlinear and classical predictions and experimental results for IM7/8551-7a with $W_0 = 0.2t$ and $\lambda = 10t$.

nar shear mode $\gamma_{xz}^{max} = 0.05$ corresponds well with the experimental results. This figure is similar to figure 5.9 for $\lambda = \lambda_{cr}$. If the fiber compression and inplane transverse tension modes are ignored temporarily, it might be possible to use the imperfection ratio I_r that was discussed earlier for a rough comparison. For figures 5.9 and 5.17 I_r is approximately equal to 0.02 for low off-axis angles. Both analyses show the same trends for the shear modes and indicate approximately the same failure loads. The differences in the fiber compression modes are significant, however. The shorter imperfection length of the predictions in figure 5.17 causes the predicted compression strength due to fiber compression failure to be lower, and causes the analysis to predict virtually the same fiber compression strength for θ = 0° to 30°. In figure 5.9 the longer imperfection length and larger imperfection amplitude did not affect the compression strength due to fiber compression as much, and the predicted compression strength due to fiber compression continued to decrease until 30°. For both figures 5.17 and 5.13, where the short imperfection lengths are used, the failure loads predicted due to inplane transverse tension using the nonlinear theory are significantly lower than the predicted inplane transverse tension failure loads shown in figures 5.9 and 5.15, respectively, where long imperfection lengths are used.

The predictions presented in figure 5.18, for the nonlinear analysis with $W_0 = 0.2t$ and $\lambda = 10t$, and from the classical analysis, were determined using the AS4/3502 material system. The trends observed in figure 5.18 are similar to figure 5.17. The predicted failure modes due to the nonlinear theory are: fiber compression failure for $\theta = 0^\circ$ to 12°; inplane transverse tension for $\theta = 12^\circ$ to approximately 37°; inplane shear failure for $\theta = 37^\circ$ to approximately 70°, and; transverse compression for $\theta = 70^\circ$ to 90°. The failure strengths predicted by the interlaminar shear mode using $\gamma_{xz}^{max} = 0.036$, as well as strengths due to the inplane transverse tension mode, are also lower than experimentally observed values. For

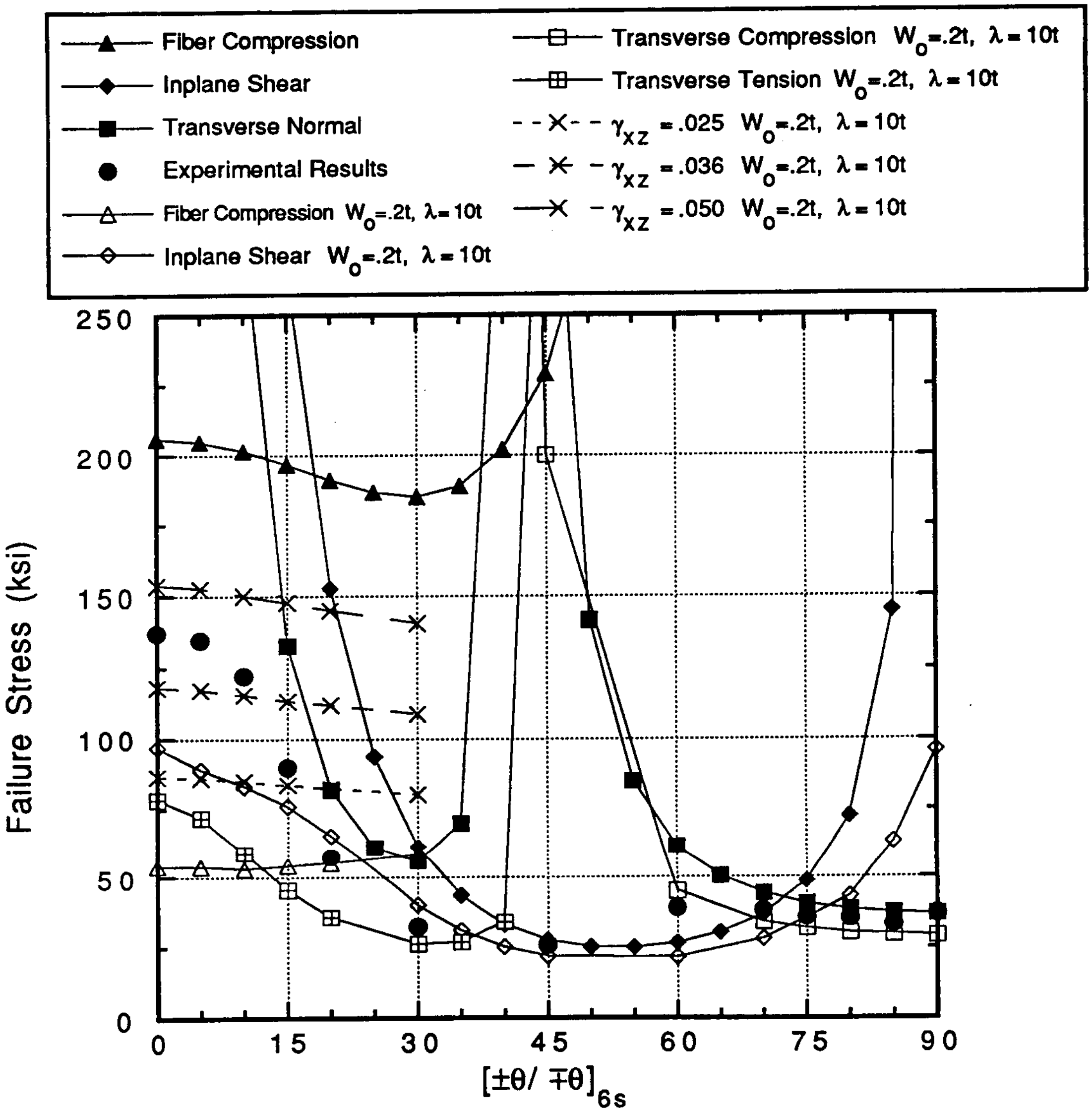

Figure 5.18 Comparison of nonlinear and classical predictions and experimental results for AS4/3502 with $W_0 = 0.2t$ and $\lambda = 10t$.

$\theta = 20^\circ$ to $\theta = 30^\circ$ the predicted inplane shear locus is higher than experimental results. Finally, the laminates shown in figures 5.18 and 5.10 have approximately the same imperfection ratio. The analyses of the two figures predict similar results for the interlaminar shear and inplane shear modes at off-axis angles less than 30°. This lends credibility to the notion the single parameter I_r may be a valid concept for some failure modes.

5.3.6 Discussion

By conducting analyses where the imperfection in a laminate is the same for every off-axis angle, comparisons can be made between different levels of imperfections and different material systems. These comparisons are: Similar trends are observed for both IM7/8551-7a and AS4/3502. However, analysis continues to show that AS4/3502 is less sensitive to wavy-type imperfections than IM7/8551-7a. Fiber-plate and matrix-foundation elastic properties for IM7/8551-7a and AS4/3502 are given in Tables 5.1 and 5.2. It is noted that AS4/3502 has a higher shear modulus than IM7/8551-7a. Since wavy-type imperfections tend to produce a shear response that is lacking in a perfect laminate, the higher shear stiffnesses are beneficial. The higher stiffnesses of the AS4/3502 matrix-foundation relative to the IM7/8551-7a matrix-foundation would also tend to restrain or reduce the effects of waviness.

Less severe imperfections, $\lambda \geq 20t$ and $W_0 < 0.2t$, produce failure loads due to fiber compression and inplane transverse tension that correlate reasonably well with experimental results at lower off-axis angles. The more severe levels of imperfections, $\lambda \leq 10t$, produce failure predictions due to interlaminar shear, using $\gamma_{xz}^{max} = 0.05$ for IM7/8551-7a and using $\gamma_{xz}^{max} = 0.036$ for AS4/3502, and inplane shear that are comparable to experimental results at off-axis angles less than 45°. Several possible conclusions can be drawn from this.

These are:

a. The published strengths due to fiber compression failure are not really generated by testing laminates that are imperfection-free. That is, the imperfection-free strengths due to fiber compression failure for IM7/8551-7a and AS4/3502 should be higher than reported. If this were the case, then the predicted fiber compression failure mode and the two shear failure modes would correlate better with the experimentally observed results discussed in chapter 2. Correspondingly, the published strengths for failure due to inplane transverse tension are also too low, or are not imperfection-free.

b. The test specimens with low off-axis angles discussed in chapter 2, did not fail due to the fiber compression mode, but due to a shear-related mode.

c. The interaction of the layers in the test specimens delayed total or catastrophic laminate failure due to inplane transverse tension.

d. The level of imperfections in the test specimens was not as severe as those modelled in some of the nonlinear analyses.

It is quite obvious from observations made in chapter 2 that ply-level waviness was not evident in every layer of every specimen, or even in every specimen tested. However, the smaller layer irregularities found could reduce the stability of a laminate such that the laminate would act as if it had wavy layers. Such correlation or equivalence of results can only be determined by conducting a carefully devised and controlled experiment, coupled with an appropriate analysis.

It was found that the loads from the fiber compression mode and the inplane transverse tension mode, i.e., modes associated with off-axis angles less than 35°, as predicted by the nonlinear theory depended more on the length of an imperfection analyzed rather than on the amplitude of the imperfection. Laminates with equivalent imperfection ratios, I_r, did not produce the same predicted compression strengths when the fiber compression failure mode or when the inplane transverse tension failure mode were considered. The nonlinear analyses did show that laminates with equivalent imperfection ratios predicted, with a little variation, equivalent failure loads for the interlaminar shear mode and the inplane shear mode. Inplane shear and interlaminar shear might be affected slightly more by larger imperfection amplitudes than by shorter imperfection lengths.

When compared to classical predictions, the shorter or more severe imperfection lengths also changed the character of the predicted fiber compression mode slightly. Instead of the predicted compression strength due to the fiber compression mode decreasing mildly as θ increases to 30°, then increasing sharply as the classical results predict, the predicted compression strength always increased as θ increased. It appears that very low off-axis angles tend to aggravate the effects that short imperfection lengths have on the fiber compression mode. Even less severe imperfections affected the character of the inplane transverse tension and inplane shear modes at very low off-axis angles.

Using the nonlinear theory, the location where each laminate is predicted to fail is the location of highest stress for each failure mode. These locations are a function of failure mode, severity of imperfection, and the off-axis angle of the laminate in question. For a laminate failing due to the fiber compression mode, the laminate is predicted to fail in the outer-most layer on the concave side of the laminate, or layer 1. For a description of layer numbering see figure 5.19. For a failure due to inplane transverse tension the laminate is predicted to fail in layer 8, or the outermost convex layer. However, at lower loads the maximum inplane transverse tension stresses are in layer 1, or the outer-most concave layer. For laminates failing due to inplane shear the predicted location is layer 1 or 2 for laminates

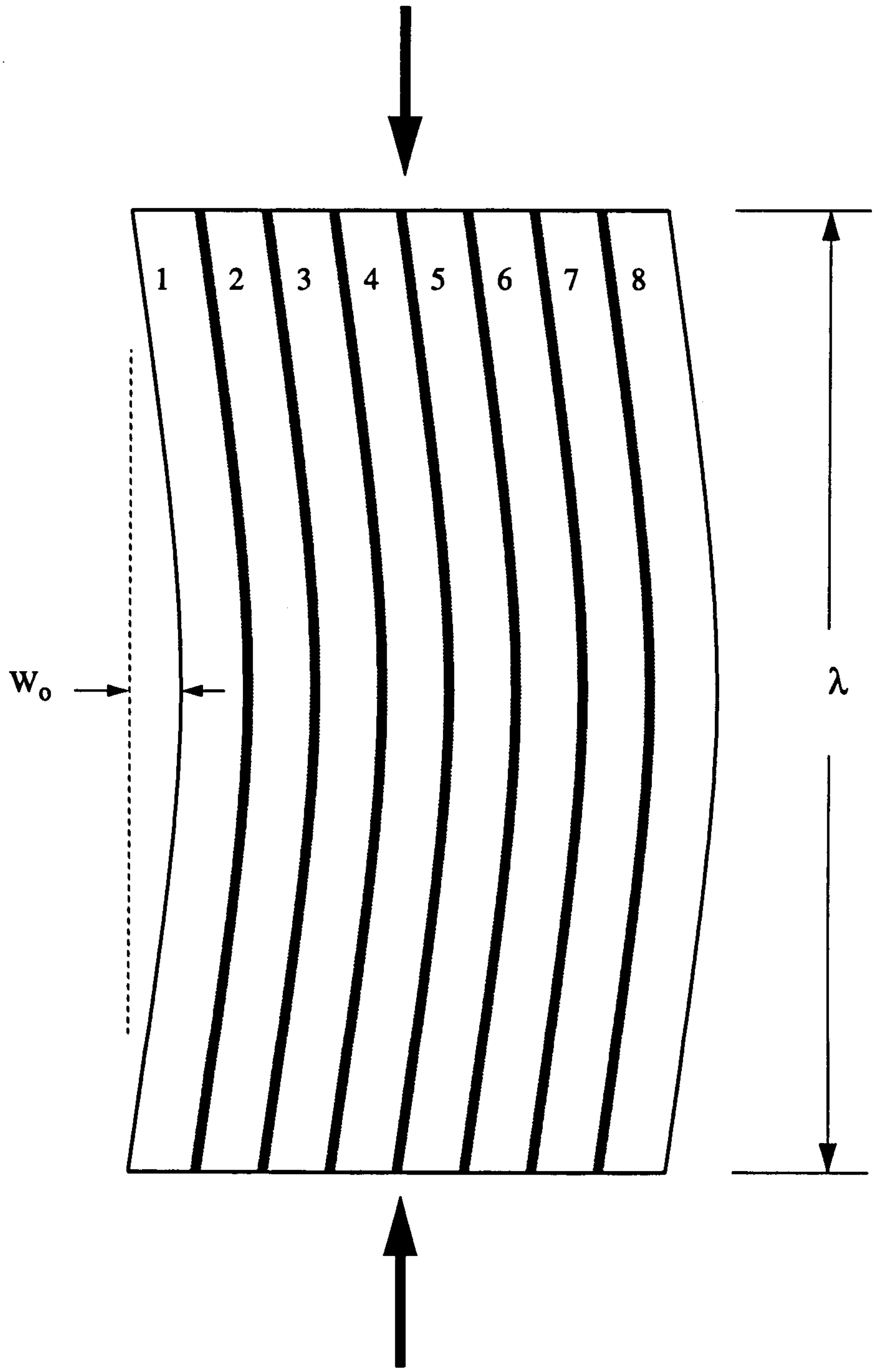

Figure 5.19 Edge view of laminate with layer numbering.

with less severe imperfections, and layer 8 for laminates with more severe imperfections. The predicted location for failure due to transverse compression and interlaminar shear is always layer 1, the outer-most concave layer.

5.4 Imperfections in Some Layers

It is most likely that actual laminates will not have noticeable imperfections in every layer. This is evidenced by the imperfections found in the scrap from the specimens, as discussed in chapter 2. As reviewed in chapter 4, the present work includes the capability to conduct nonlinear analyses of laminates with imperfections in only some of the layers, or with imperfection amplitudes that vary from layer to layer. The nonlinear analysis, however, does not adjust the thicknesses of matrix-foundations between layers to allow for differences in levels of imperfection in adjacent fiber-plates. The errors in matrix-foundation thicknesses are felt to produce negligible errors in fiber-plate stresses and strains. However the errors in matrix-foundation thicknesses can produce significant errors in interlaminar strains. For that reason the predictions discussed in the following paragraphs do not include any discussion of interlaminar strains.

5.4.1 Types of Partial Waviness

The types and levels of partial waviness were chosen to be representative of those found in practice. Four types of partial waviness were studied. These are illustrated in figure 5.20. In figure 5.20a the type of imperfection studied in the previous sections is shown. With this imperfection every layer is assumed to have the same amplitude of waviness. Figure 5.20b illustrates a partial imperfection where the outside layer on one side of the laminate has no waviness and the amplitude of waviness increases on a layer by layer basis so that the out-

1. Every layer imperfect.

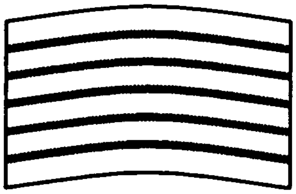

(a)

2. Imperfections ranging from none to max.

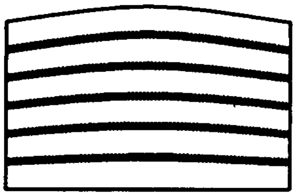

(b)

3. Maximum imperfection at center.

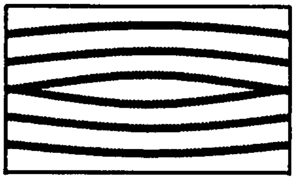

(c)

4. Max imperfection at center, reverse imperfection.

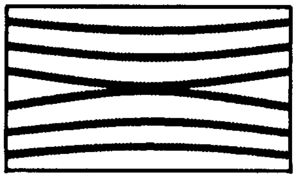

(d)

5. Only one layer imperfect.

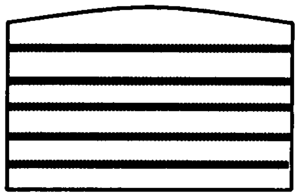

(e)

Figure 5.20 Types of partial imperfections.

side layer on the other side of the laminate has a maximum amount of waviness, W_0. Figure 5.20c illustrates the second type of partial waviness studied. For this case the maximum wave amplitude, W_0, is in the layers adjacent to the midplane of the laminate. Layers on the opposite side of the mid-plane have waviness of the opposite sign such that the mid-plane area is resin-rich. The layers on the outside have no waviness. The third type of partial waviness studied is shown in figure 5.20d. This is similar to the waviness of figure 5.20c except the midplane of the laminate is resin-starved. The fourth type of partial waviness, shown in figure 5.20e, considers one layer to be wavy and the other layers being perfectly flat. In the figure it is the outside layer that is assumed to be wavy. In a following section other isolated layers are considered to be wavy.

A preliminary analysis using the nonlinear theory was conducted to determine the relative severity of each type of partial imperfection. A laminate with an off-axis angle of 5° was analyzed with each imperfection as shown in figure 5.20. The half-wavelength used is 20t and the maximum imperfection amplitude is 0.2t. A load of 125 ksi was applied to each imperfect laminate and the fiber-direction stress computed. The results of this preliminary study can be seen in figure 5.21. In figure 5.21, and hereafter, the various types or levels of imperfections will be known by their corresponding number. For example, a single imperfect layer will be a type 5 imperfection. In figure 5.21 the results are compared to a laminate with full imperfections in every layer, a type 1 imperfection. From figure 5.21 it can be seen that except for the type 1 imperfection, the type 2 and type 5 imperfections produced the highest fiber-direction stresses. The type 3 and 4 imperfections produced the lowest fiber-direction stresses, the stress levels being about the same. As as result of this preliminary study it was decided to use the type 2, type 3, and type 5 partial imperfections for the remainder of the partial imperfection study. It was further decided to use a single layer im-

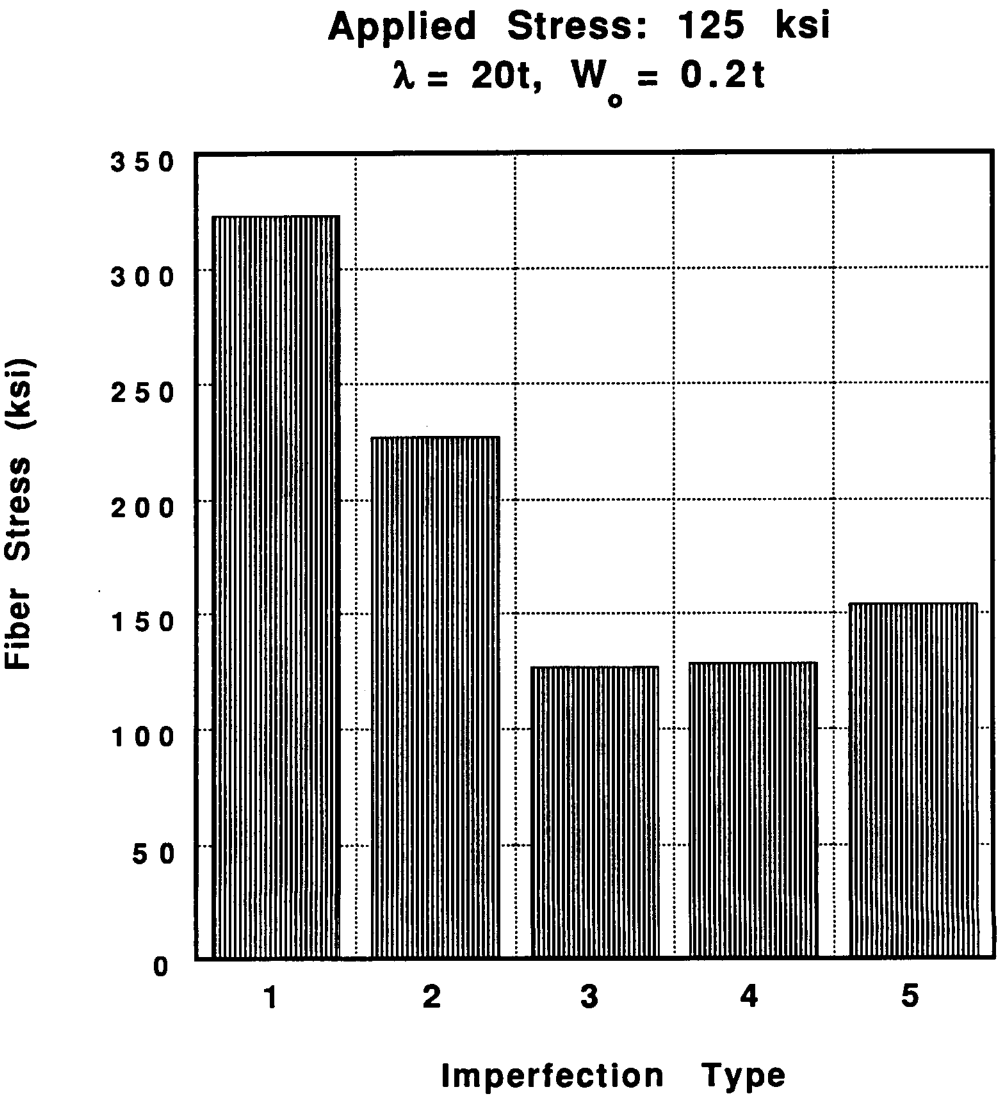

Figure 5.21 The compressive stresses due to the fiber compression failure mode for each imperfection.

perfection with the single imperfect layer is the outer-most layer, then the imperfect layer the second layer in, and finally, the imperfect layer the fourth layer in. All laminates analyzed consist of a total of eight layers. The imperfection length chosen for all analyses in this section is 20t. The maximum imperfection amplitude chosen is 0.2t.

5.4.2 Comparison of Results

Figure 5.22 shows the predictions of analyses conducted using the nonlinear analysis and a type 3 imperfection. The predictions of the classical theory are also included, as are the experimental results. The material system used is IM7/8551-7a. All results discussed in this section will be based on the IM7/8551-7a material system. The solid triangles represent failure loads from the fiber compression failure mode using the classical theory. The solid diamonds and squares represent failure loads from the inplane shear and inplane transverse tension/compression failure modes respectively, using the classical theory. The open triangles represent the failure loads resulting from the fiber compression failure mode using the nonlinear theory. The open squares with crosses in them represent failure loads from the inplane transverse tension failure mode using the nonlinear theory. The open diamonds represent failure loads from the inplane shear failure mode using the nonlinear theory. The open data points represent analyses conducted at 0°, 15° and 30°. A preliminary study showed that predictions obtained from analysis using the nonlinear theory for $\theta \geq 45^\circ$ would produce predictions almost identical to predictions at $\theta \geq 45^\circ$ using the classical theory. Hence the predicted failure loads for $\theta \geq 45^\circ$ due to the inplane shear mode using the nonlinear theory are assumed to be the same as the failure loads calculated using classical theory. Since analyses using the nonlinear theory were only conducted at 0°, 15°, and 30°, the loci represented by each failure mode appear coarse and fragmented.

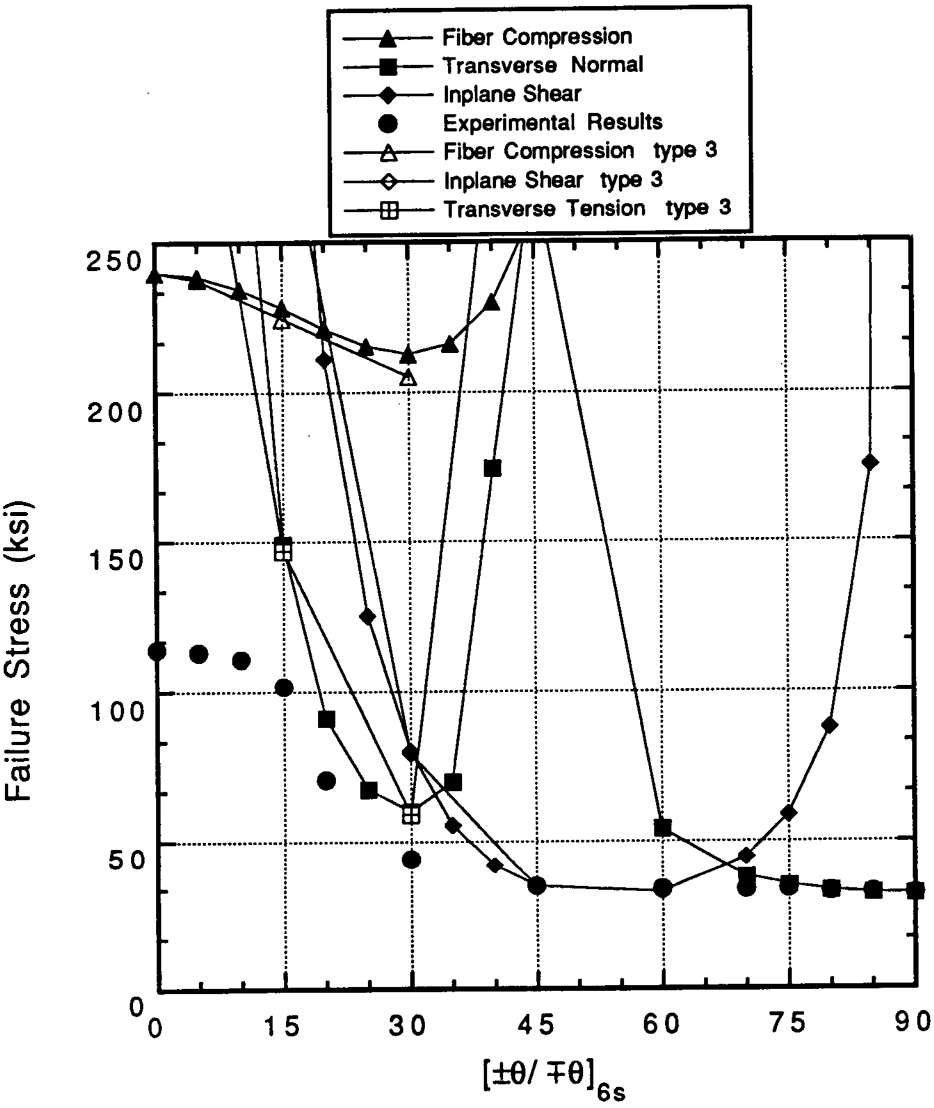

Figure 5.22 Comparison of nonlinear and classical predictions and experimental results for IM7/8551-7a for a type 3 imperfection with $W_0^{max} = 0.2t$ and $\lambda = 20t$.

It is quite obvious in figure 5.22 that compared to the classical analysis, the type 3 imperfection used in the analysis does not affect compression strength much. It appears that failure loads due to the fiber compression mode using the nonlinear theory decreased by less than one percent relative to the values using the classical theory. The failure loads due to the inplane shear failure mode are indistinguishable from their classical counterparts. The failure loads resulting from the inplane transverse tension mode as predicted using the nonlinear theory are slightly lower than the corresponding loads predicted using classical lamination theory. In summary, the type 3 imperfection does not effect the compressive strength of angle-ply laminates.

In figure 5.23 comparisons are made with failure loads as predicted by the nonlinear theory with a type 2 imperfection, as predicted by the classical theory, and as experimentally measured. The analyses conducted using the nonlinear theory show that this type of imperfection reduces the compression strength of angle-ply laminates considerably more than the type 3 imperfection. For a unidirectional laminate ($\theta = 0^\circ$), the failure load due to the fiber compression mode as predicted by the nonlinear theory is approximately one-half the failure load predicted using classical theory. Both the inplane shear and the inplane transverse tension failure modes using the nonlinear theory now predict finite strengths at $\theta = 0^\circ$ rather than infinite strengths as predicted by classical theory. These two failure loci are lower than the failure locus due to fiber compression as predicted by classical theory. The locus of failure loads due to inplane transverse tension failure as predicted by nonlinear theory has decreased from its classical counterpart. The failure strengths due to the inplane transverse tension mode correlate quite well, although non-conservatively, with experimental strengths for θ between 15° and 30°. It is interesting to compare the predictions of figure 5.15 for a type 1 imperfection, the case where every layer has the same level of im-

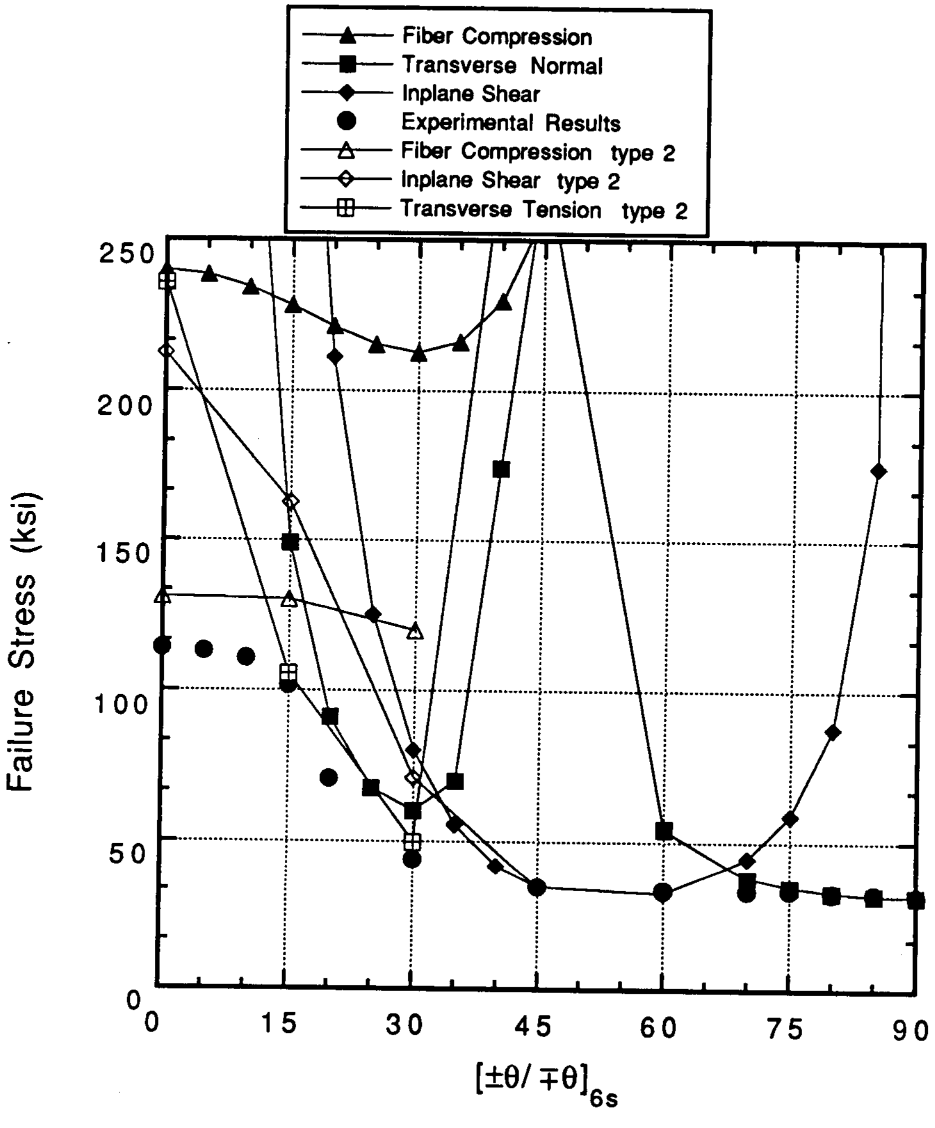

Figure 5.23 Comparison of nonlinear and classical predictions and experimental results for IM7/8551-7a for a type 2 imperfection with $W_0^{max} = 0.2t$ and $\lambda = 20t$.

perfection, with figure 5.23 for the type 2 imperfection. It can be seen that the effects of a type 2 imperfection are similar to, but less severe than, the effects of a type 1 imperfection.

In figures 5.24, 5.25, and 5.26 comparisons are made with failure loads as predicted by the nonlinear theory using a type 5 imperfection, by the classical theory, and as measured in the experiments. In figure 5.24 predictions are shown for analyses where only the outermost layer, or layer 1, is wavy. In figure 5.25 predictions are shown for analyses where only layer 2 is wavy. Figure 5.26 compares predictions where only layer 4 is wavy. As can be seen by comparing these figures, the failure loads due to the various failure modes are essentially the same, regardless of the location of the single imperfect layer. The failure loads predicted due to fiber compression failure using the nonlinear theory are slightly greater when the wavy layer is layer 4, near the center of the laminate, as shown by figure 5.26. This would indicate that adjoining perfect layers may slightly reduce the effects of an imperfection on compressive strength. The failure loads due to fiber compression using the nonlinear theory are still considerably higher than experimentally observed failure strengths. The predicted failure modes due to the nonlinear theory for the analyses shown in all three figures, are: fiber compression failure for $\theta = 0^\circ$ to 15°; inplane transverse tension for $\theta = 15^\circ$ to approximately 35°; inplane shear failure for $\theta = 35^\circ$ to approximately 68°, and; inplane transverse compression for $\theta > 68^\circ$.

5.4.3 Discussion

The analysis using partial imperfections showed the same trends as did the analyses using full imperfections. Some types of imperfections, despite their appearance of being severe, actually had little impact on compression strength of angle-ply laminates. The type 3 imperfection, for example, did not seem to affect compressive strength. Since the type 3

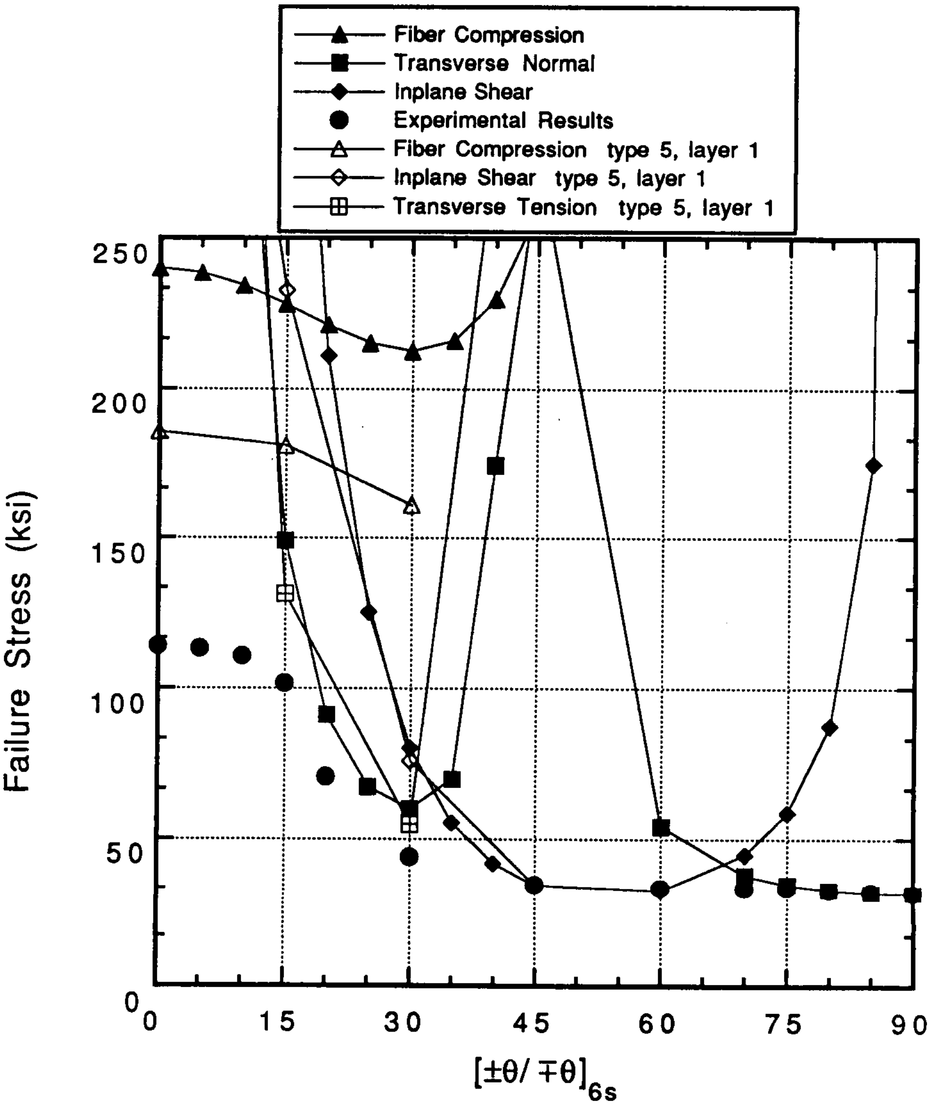

Figure 5.24 Comparison of nonlinear and classical predictions and experimental results for IM7/8551-7a for layer 1 imperfect with $W_0^{max} = 0.2t$ and $\lambda = 20t$.

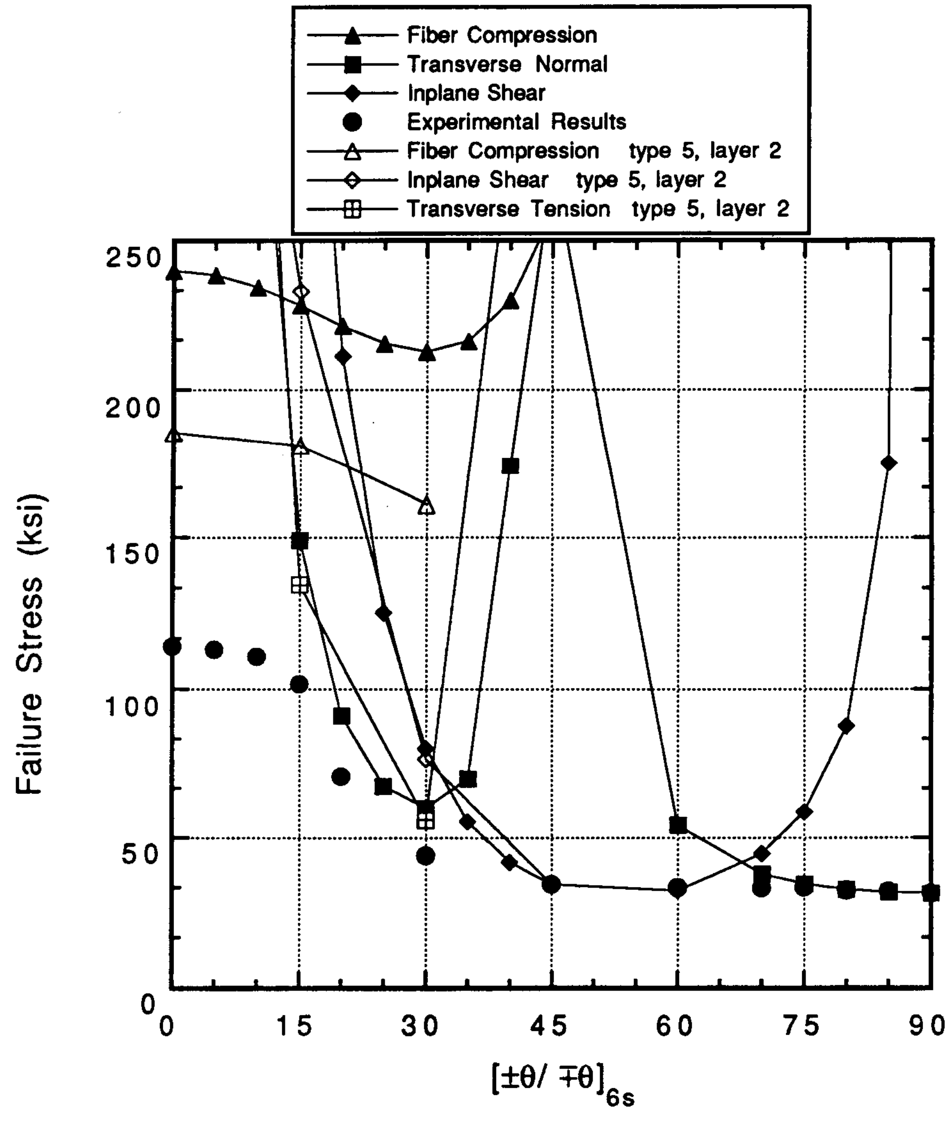

Figure 5.25 Comparison of nonlinear and classical predictions and experimental results for IM7/8551-7a for layer 2 imperfect with $W_0^{max} = 0.2t$ and $\lambda = 20t$.

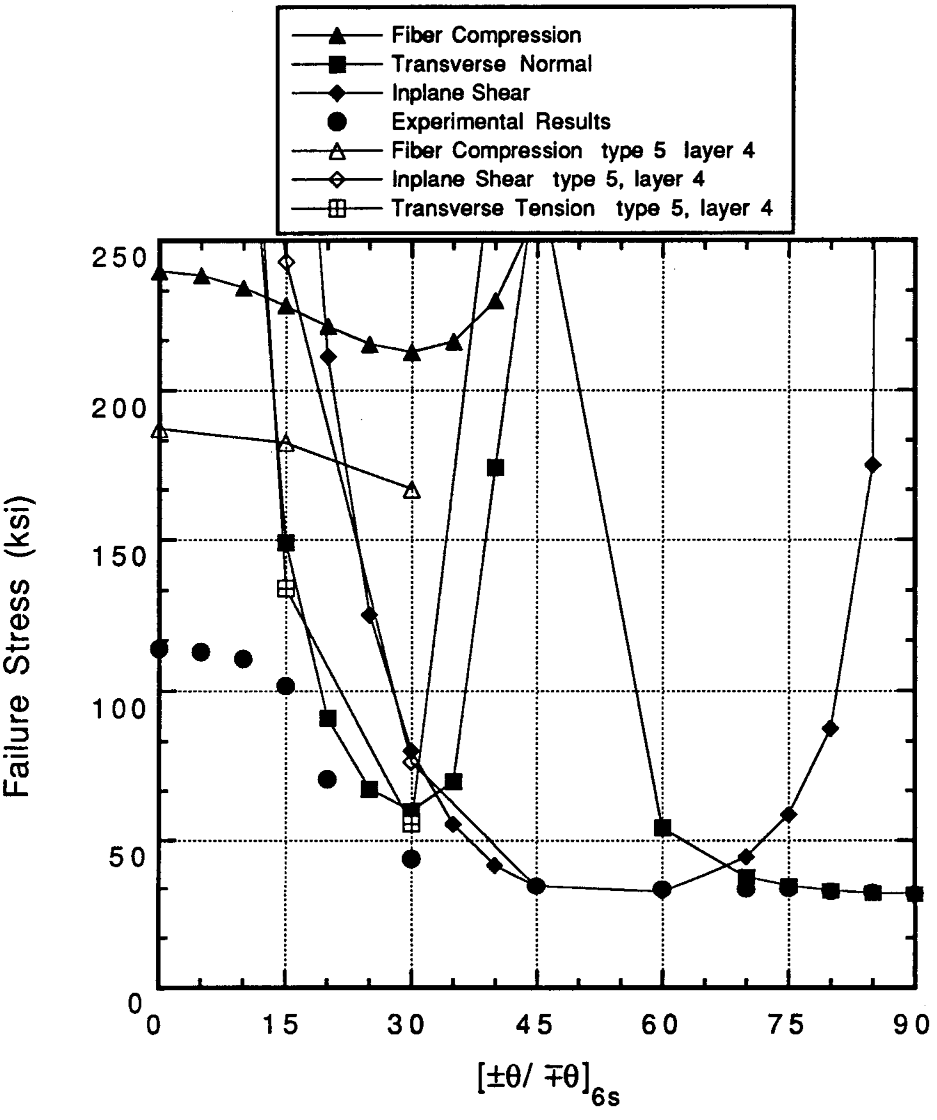

Figure 5.26 Comparison of nonlinear and classical predictions and experimental results for IM7/8551-7a for layer 4 imperfect with $W_0^{max} = 0.2t$ and $\lambda = 20t$.

imperfection is symmetric about the mid-plane of the laminate, the imperfection does not induce an eccentric response. Thus, overall out-of-plane deflections of the layers were small. In addition, with a type 3 imperfection the imperfection amplitude decreases the closer the layer is to the outside. The outer-most layers were perfectly flat. These outer flat layers could restrain any out-of-plane instability-type behavior of the inner layers, further limiting loss of strength when compared to the classic case.

The analysis using the nonlinear theory show that a type 5 imperfection introduces eccentricities into the laminate. These eccentricities are due to a variation in effective stiffness rather than load variation. The resulting out-of-plane deflections and bending yield higher inplane stresses than would occur in a flat laminate. The different locations of the single imperfect layer do not have a significant influence on the predicted failure strength. Hence, it would appear that the stiffness eccentricities introduced by the imperfect layer can overpower the restraining effects of adjacent layers.

For partial imperfections the predicted failure loads from the nonlinear theory are lowest for the type 2 imperfection. This type of imperfection produces increased bending and shear stresses, out-of-plane deflections on the imperfect side of the laminate, and increased axial stresses on the flat side of the laminate. Since the imperfect side of the laminate deflects as soon as a load is applied, and the flatter portion deflects less, or not at all, the nature of the method used to load the laminate causes the flatter portion takes a high percentage of the load.This induces high axial stresses in the flat portion of the laminate. The flatter layers therefore appear stiffer in the axial direction.

The predicted location where each laminate would fail is the location of highest stress for the appropriate failure mode in that laminate. These locations are a function of failure mode, the type of imperfection, and the off-axis angle of the laminate in question. Considering failure due to fiber compression, for $\theta < 25^\circ$ the laminate always failed at the outer-most layer with the lowest imperfection amplitude. As mentioned above, this is the 'stiff-est' layer. Failure due to inplane transverse tension occurs in the layer with the most severe imperfection, or the most convex layer. However, failure due to inplane transverse tension occurs at either outer layer of the laminate for laminates with a type 3 imperfection. Except for unidirectional laminates failure due to inplane shear always occurs at the layer where the imperfection amplitude is greatest. For unidirectional laminates failure is predicted to always occurs at the outer-most flat layer.

5.5 Summary of All Analyses

Much has been learned about the nature of laminates with wavy-type imperfections. Using critical buckling half-wavelengths as imperfection lengths cause the relative severity of the imperfection to increase as the off-axis angle increases. The AS4/3502 material system is less sensitive to wavy imperfections than the IM7/8551-7a material system because the laminate and matrix shear moduli of the AS4/3502 material system are higher than the corresponding shear moduli of the IM7/8551-7a material system. The higher shear moduli provide greater resistance to bending, hence the effect of a wavy imperfection is reduced. The analyses using the nonlinear theory indicates that both material systems have similar failure modes. The nonlinear theory supports the assumption that angle-ply laminates with off-axis angles of about 40° and greater are relatively insensitive to imperfections when subjected to compressive loads.

For laminates with less severe imperfections, $\lambda \geq 20t$ and $W_0 < 0.2t$, and off-axis angles less than approximately 35°, the predicted failure loads due to the fiber compression and inplane transverse tension failure modes using the nonlinear theory correlate well with experimental results. The more severe levels of imperfections in the laminates, $\lambda \leq 10t$, produce failure due to interlaminar shear, using $\gamma_{xz}^{max} = 0.05$ for IM7/8551-7a and using $\gamma_{xz}^{max} = 0.036$ for AS4/3502, and due to inplane shear that are comparable to experimental results at off-axis angles less than 45°.

The failure loads due to the fiber compression mode and the inplane transverse tension mode depend more heavily on the imperfection length than on the imperfection amplitude. The nonlinear analyses predicted that laminates with equivalent imperfection ratios show approximately equivalent failure loads for the interlaminar shear mode and the inplane shear mode. However, inplane shear and interlaminar shear might be affected slightly more by variations in imperfection amplitude than by imperfection length.

The most likely layer to fail first for a laminate with imperfections in every layer is layer 1, the outer-most concave layer. The location of laminate failure is a function of failure mode, degree of imperfection severity, and off-axis angle. The location did not appear to be a function of material system.

The discussion has shown that for laminates with the same level of imperfection in every layer (type 1 imperfection) the wavelength and wave amplitude influence the reduction in compression strength of a laminate compared to the strength predicted by the classical theory. Figures 5.27 through 5.30 graphically illustrate this concept. Figures 5.27 and 5.28 compare the relative retained strength for the IM7/8551-7a and AS4/3502 material systems where the imperfection lengths are the critical buckling half-wavelengths. The relative retained strength, at a specific off-axis angle, is defined as

$$\frac{\sigma^{nl}}{\sigma^{cl}}, \tag{5.2}$$

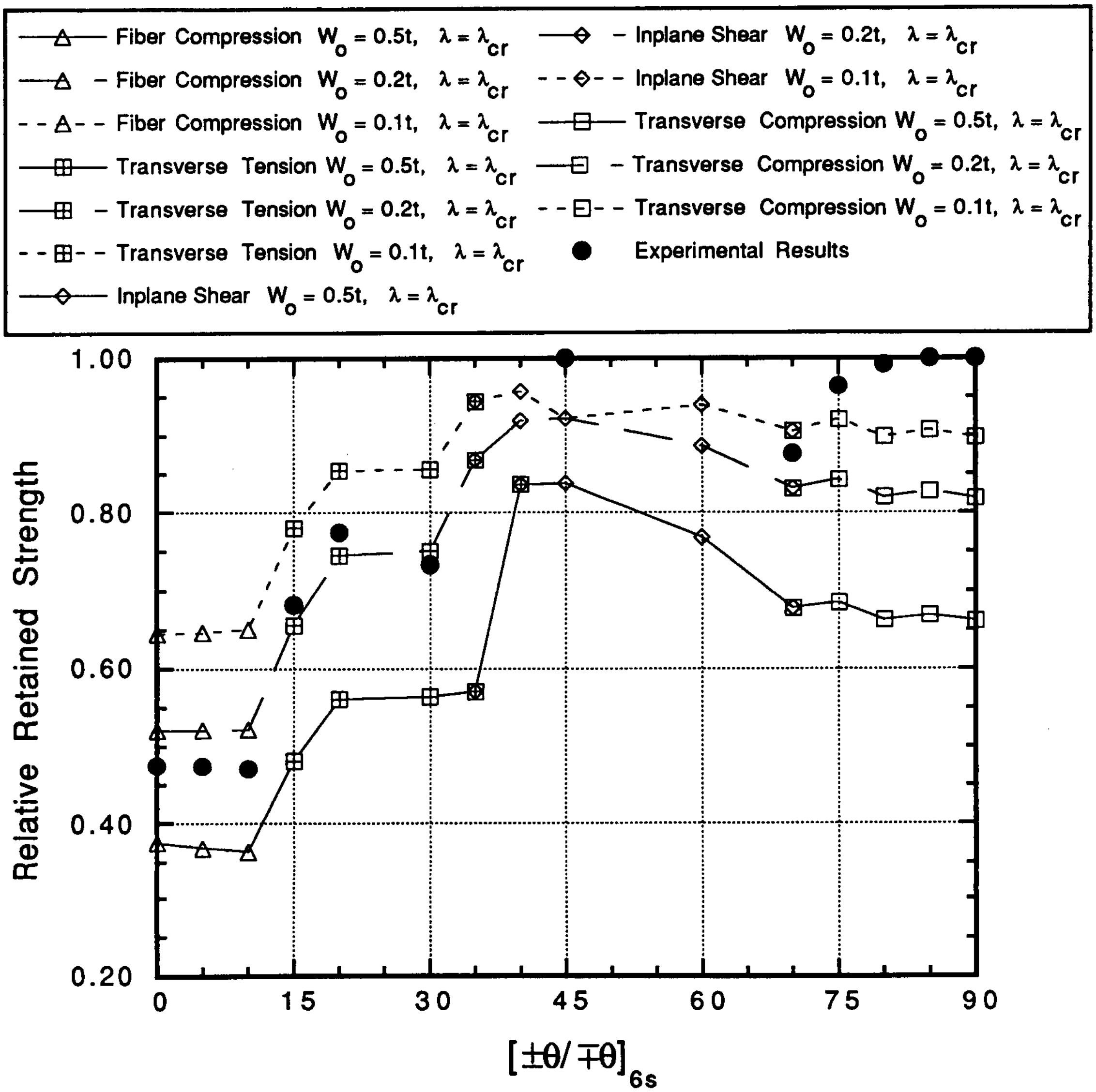

Figure 5.27 Relative retained strength of IM7/8551-7a using critical half-wavelengths as imperfection lengths, type 1 imperfection.

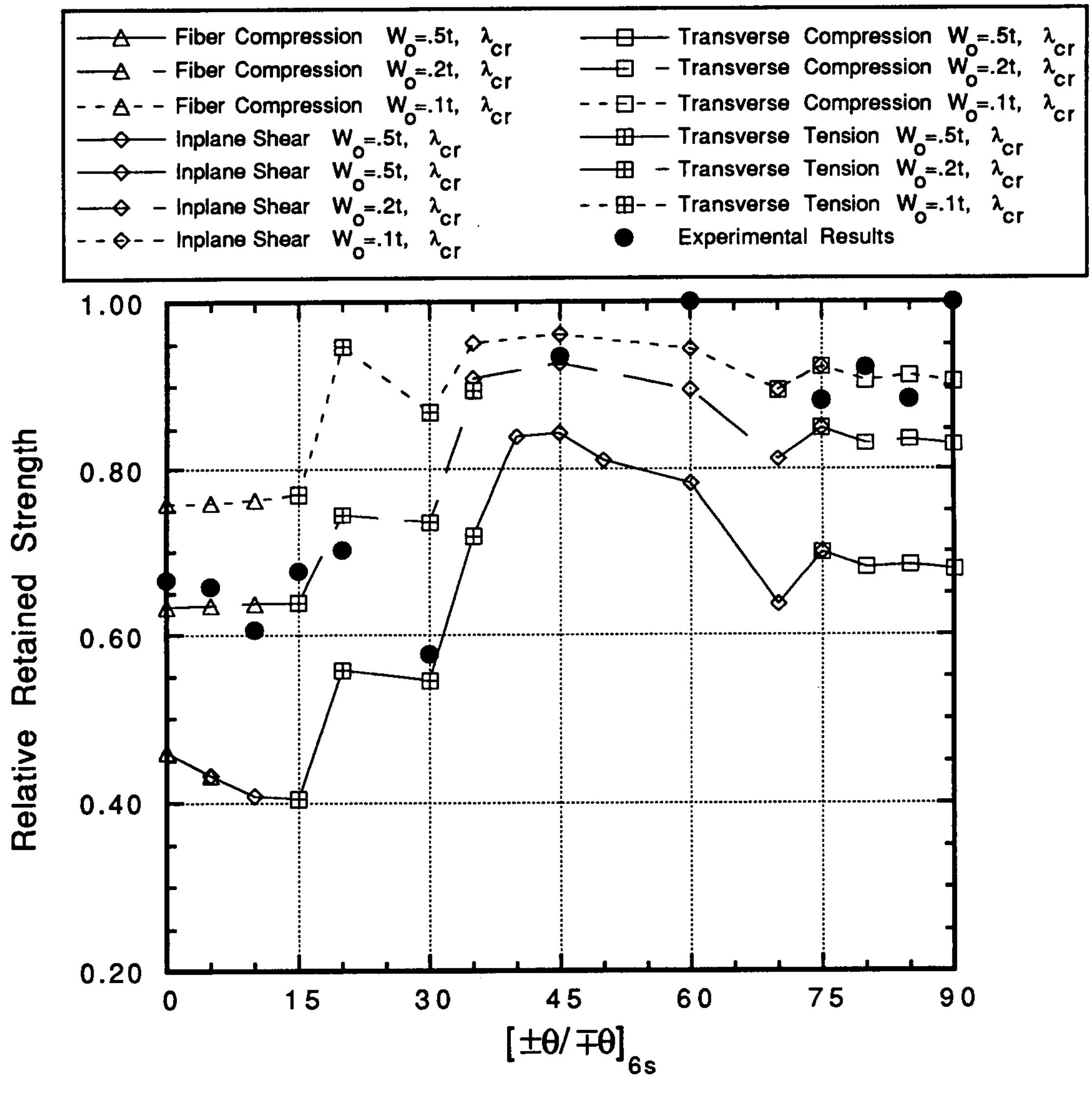

Figure 5.28 Relative retained strength of AS4/3502 using critical half-wavelengths as imperfection lengths, type 1 imperfection.

where σ^{nl} is the failure stress predicted using the nonlinear analysis with an imperfection. The quantity σ^{cl} is the failure stress predicted with classical analyses. It is very possible that the failure mode associated with σ^{nl} may not be the same as the failure mode associated with σ^{cl}. In the figures the open symbols have their usual meanings, the filled circles represent experimental results, and the different line types represent levels of imperfection severity. The symbols are the failure modes as predicted by the nonlinear analysis. Discontinuities or abrupt changes of the same line types indicate failure mode changes. Two symbols at the same point indicate two failure modes present at that angle. If on the same line the symbol changes, then the failure mode has changed also. The lowest retained strengths occurs at the lower off-axis angles. For figure 5.27 through figure 5.30 the experimental results show the highest retained strength after $\theta = 40^\circ$. Between 70° and 80° the lower retained strengths of the experimental results are due to changing failure modes, not actual decreases in strength. Note in figure 5.27 and 5.28 that relative retained strength of the laminate with an imperfection amplitude of 0.5t is always lower than the relative retained strength of the experimental result. This reinforces the conclusion that $W_0 = 0.5t$, for $\lambda = \lambda_{cr}$, is an unrealistically severe imperfection amplitude.

Figures 5.29 and 5.30 compare the relative retained strength that was predicted for the IM7/8551-7a and AS4/3502 material systems, also with a type 1 imperfection, where the imperfection lengths vary as well as imperfection amplitudes. For $\theta < 40^\circ$ the amount of retained strength varies considerably due to the different levels of imperfection. In figure 5.29 the relative retained strength increases quite uniformly for $\theta < 45^\circ$. A similar but more erratic pattern can be seen in figure 5.30. In both figures the analyses using the shorter imperfection lengths always resulted in the lowest retained strengths. The nonlinear predictions and the experimental results for IM7/8551-7a show lower retained strengths

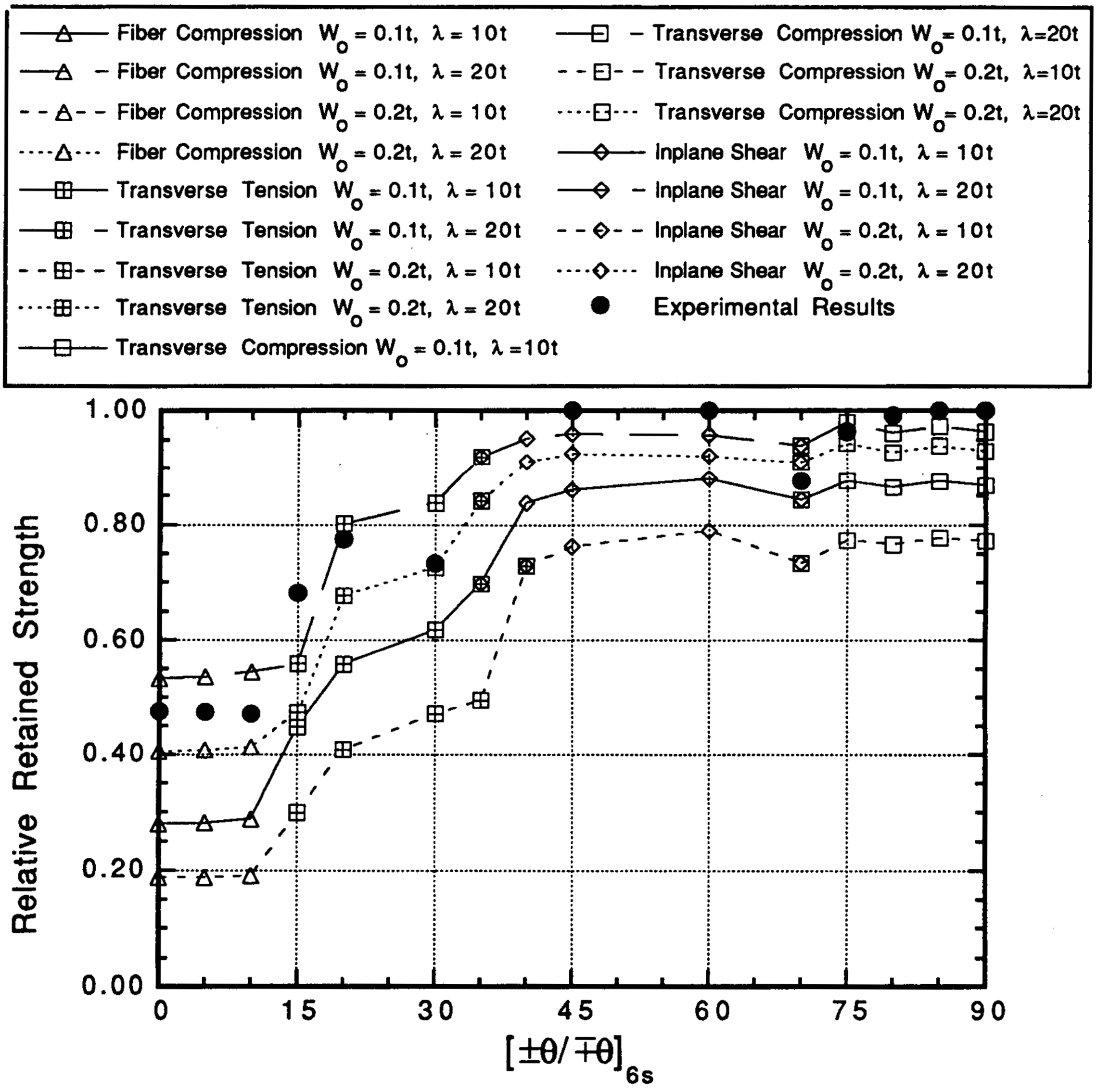

Figure 5.29 Relative retained strength of IM7/8551-7a using varying imperfection lengths, type 1 imperfection.

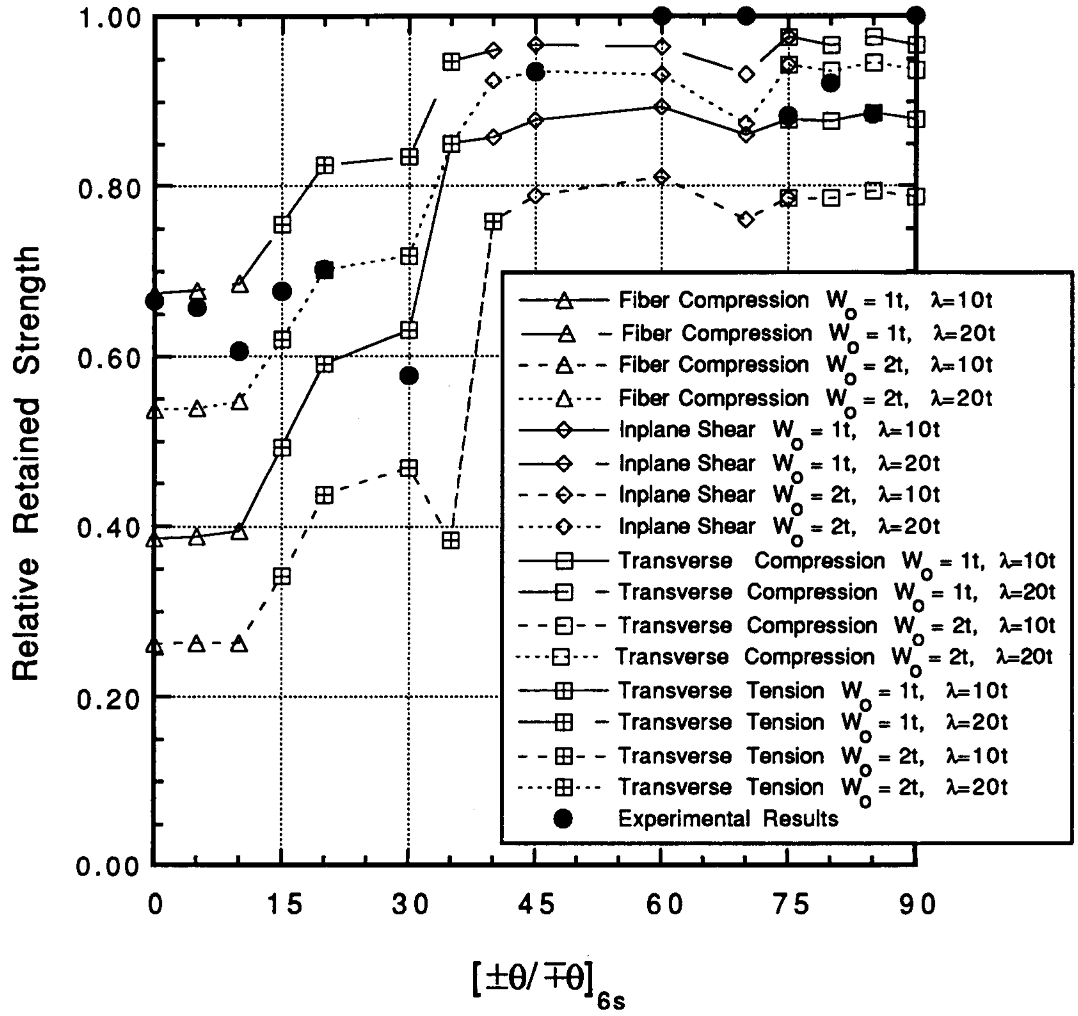

Figure 5.30 Relative retained strength of AS4/3502 using varying imperfection lengths, type 1 imperfection.

than the predictions and results for AS4/3502 do at low off-axis angles. This is just another way to show the higher sensitivity of IM7/8551-7a to wavy imperfections. At higher off-axis angles all experimental results show high retained strength, except for the variations discussed earlier.

These figures not only show the range of retained strength, where that range depends on the imperfection level, but they also show trends of imperfection sensitivity as a function of off-axis angle. Similar figures for a range of materials would be extremely useful in the design of composite structures. Since the stiffness of an angle-ply laminate is a function off-axis angle, the results shown in figures 5.27 through 5.30 could also be thought of as functions of stiffness.

Continuing to summarize the results, several types of imperfections were discussed where not every layer in the laminate was imperfect. It was found that if an imperfection introduced stiffness eccentricities into a laminate because the imperfection was not symmetric about the mid-plane of the laminate, bending, out-of-plane deflections, and shear deformation tended to reduce compression strengths due to fiber compression failure, inplane transverse tension failure, and inplane shear failure. The type 3 imperfection, one that is symmetric about the midplane of a laminate, does not significantly affect compression strength. The location of failure in a partially wavy laminate is heavily dependent on the failure mode and off-axis angle. The most likely location for failure of a laminate that does not have imperfections in every layer is in an outer flat layer.

6.0 CONCLUSIONS AND FUTURE WORK

As outlined and discussed in chapter 1, the primary objectives of the present work were to:

1. Study experimentally and analytically the compression failure of angle-ply IM7/8551-7a laminates;
2. Enlarge upon the linear and nonlinear theories of Shuart[21,22] to develop more comprehensive methods for predicting compressive strength;
3. Compare the results obtained for IM7/8551-7a with the results for AS4/3502 found in reference 22.

These objectives were accomplished in the manner set forth in chapter 1. The results and the conclusions obtained from the present work, as a result of these objectives, are grouped into three major areas:

a. ***Testing of Specimens***. Compression tests of 42 angle-ply specimens fabricated from IM7/8551-7a were carried out. The results were compared with previously obtained experimental results for AS4/3502. Similarities and differences were noted and discussed.

b. ***Modifications and Enhancements to Previously Developed Theory***. The previously developed linear and nonlinear theories and the associated computer programs were reviewed. Modifications, both strictly cosmetic to the codes and analytical as regards to the theory, were discussed. Sample problems were presented.

c. ***Analytical Results***. Parametric studies of IM7/8551-7a and AS4/3502 using the linear and nonlinear theories were conducted, and the two material systems were compared. These studies considered the effects of wavy imperfections in every layer of a laminate, and wavy imperfections in only part of the layers in a laminate.

6.1 Testing of Specimens

The present work included experimentally observed compression strengths for angle-ply laminates of IM7/8551-7a. These results were discussed in chapter 2. A short-block compression test fixture was used. This fixture had the advantages of being simple, easy to use, and did not seem to restrict specimens from failing due to the short-wavelength buckling mode. The test results and modes of failure fell into four major categories:

a. *Brooming, kink bands, and transverse splitting.* Because of the diverse mechanisms present in each failed specimen this is the most difficult category to characterize. This category can be described as having fiber or ply-level instabilities which aggravate several types of failure mechanisms. The angle-ply laminates in this category range from $\theta = 0^\circ$ to approximately 10°.

b. *Inplane transverse tension and/or inplane shear.* The failed specimens in this category show very distinct and reproducible failure characteristics. Each failed specimen fractured with failure surfaces parallel to the fiber direction. Failure due to either inplane shear or inplane transverse tension produce these types of failure surfaces. Angle-ply laminates in the range of 10° to 35° failed in this mode.

c. *Inplane shear with matrix softening.* The tests in this category produced high axial strains to failure with considerable nonlinearity in their stress-strain relations. Kink-bands through-the-thickness and delamination of the specimens are characteristic of this category. The angle-ply laminates in this category range from $\theta = 35^\circ$ to approximately 70°.

d. *Inplane transverse compression.* The failure mechanisms evident in this category are the most similar to typical compressive failure for isotropic materials. A failure surface across the width of the laminate and inclined at 45° to the thickness direction characterize the failure. The angle-ply laminates in this category are for $\theta > 70^\circ$.

Elastic properties and some laminate strengths were obtained from the data. Comparisons between experimentally observed values of IM7/8551-7a and AS4/3502 show similar failure characteristics. Using experimentally derived elastic properties and strengths, and published strengths to account for strengths that could not be obtained from the experiments, classical lamination theory and the maximum stress failure criterion were used to predict the failure strengths of the angle-ply specimens. Considerable differences between the strengths predicted using the classical theory and experimentally observed compression strengths were noted for $\theta < 40^\circ$. Hence it was decided to investigate imperfections as a source of strength reduction.

6.2 Modifications and Enhancements to Previously Developed Theory

Linear and nonlinear theories and associated computer programs were obtained from a previous work.[21,22] These theories were modified and enhanced in the present work. Modifications to the linear theory consisted mainly of cosmetic, portability, and performance enhancements to the associated computer program.

Modifications to the nonlinear theory included the ability to vary the amplitude of a wavy-type imperfection on a layer-by-layer basis. Post-processor computer programs were written to so results from the nonlinear theory could be quickly and accurately analyzed. The fiber compression and inplane transverse tension failure modes were included in the present analyses using the nonlinear theory. These modes were not included in the original theory.

6.3 Analytical Results

Analyses using the nonlinear theory were conducted and the resulting compressive failure strengths were compared with predicted compression strengths using the classical theory and experimental results. The analyses included laminates where every layer had the same wavy-type imperfection, and laminates where every layer in a laminate did not have the same imperfection. The wavy imperfection was described by an imperfection amplitude W_0 and an imperfection length λ. In the group of analyses where every layer was imperfect the critical buckling wavelengths as obtained from the linear analysis were used as imperfection lengths. The effects of several imperfection amplitudes with the critical buckling half-wavelengths were explored. Also in the group of analyses where every layer was imperfect, other values for the imperfection lengths were explored in conjunction with two imperfection amplitudes. Finally, several types of imperfection and several imperfection levels, were used in the group of analyses where not every layer had the same imperfection, and not every layer was imperfect. As a side note, it was found that when the critical buckling half-wavelengths are used as the imperfection length in a laminate, the relative severity of the imperfection increases as the off-axis angle of the laminate increases.

Both analytical predictions and experimental results indicate the AS4/3502 material system is less sensitive to imperfections than the IM7/8551-7a material system. This is thought to be a result of the laminate and matrix shear moduli of the AS4/3502 material system being higher than the corresponding shear moduli of the IM7/8551-7a material system.

For the group of analyses where every layer is imperfect, the nonlinear theory predicts compression failure loads that are a function of the off-axis angle, the relative severity of the imperfection amplitude and imperfection length, and the compressive failure mode that is dominant at that off-axis angle.

The use of an imperfection ratio I_r, where $I_r = W_0/\lambda$, as the sole descriptor of a wavy imperfection can be misleading. Failure loads due to the fiber compression and inplane transverse tension failure modes as predicted by the nonlinear theory depend more heavily on imperfection length than on imperfection amplitude. Therefore laminates with equivalent imperfection ratios, but with different imperfection lengths, will result in different predicted compression strengths due to the fiber compression and transverse tension failure modes. The imperfection ratio has no meaning for those failure modes. Failure loads due to the interlaminar shear and inplane shear modes as predicted using the nonlinear theory may be considered, with slight variations, functions of the imperfection ratio. The interlaminar shear and inplane shear modes are just slightly more dependent on imperfection amplitude than on imperfection length. Hence, laminates with equivalent imperfection ratios will result in roughly equivalent predicted failure loads if failure is due to the interlaminar or inplane shear modes.

Analysis using the nonlinear theory with laminates having less severe imperfections, $\lambda \geq 20t$ and $W_0 \leq 0.2t$, show that for off-axis angles less than approximately 35° compression strength predictions due to the fiber compression and inplane transverse tension modes compare well with experimental results. Conversely, analytical results from laminates having more severe levels of imperfection, $\lambda < 20t$, indicate that for $\theta \leq 35°$ compression strength predictions due to the interlaminar shear and the inplane shear failure modes are comparable to experimentally observed compression tests. The predicted location within a laminate for compression failure to begin is a function of failure mode, off-axis angle, and relative imperfection severity, with the most common location being the outermost concave layer of the laminate.

For the group of analyses where every layer is not imperfect and every layer does not have the same imperfection amplitude, the nonlinear theory predicts compression strengths that are a function of the off-axis angle, the type of imperfection, and the failure mode. In the case where an imperfection is symmetric about the mid-plane of a laminate and the outer layers of the laminate are flat or imperfection-free, the imperfection does not significantly reduce the compression strength of the angle-ply laminate. Flat or imperfection-free layers surrounding wavy-type imperfections can reduce the effects of the imperfect layers. Other types of partial imperfections may introduce stiffness eccentricities which can significantly reduce compression strength. The predicted location for compression failure to begin, within a laminate having partial imperfections is also a function of failure mode, off-axis angle, and type of imperfection.

The nonlinear analysis in its present form can be especially useful to the composite structures designer in providing information on imperfection sensitivities, such as that found in figures 5.27 through 5.30. These figures show retained compressive strength as a function of imperfection level, off-axis angle, and material system. This strength retention is relative to the imperfection-free laminate. The nonlinear theory is also useful in comparing analogous material systems with regard to their sensitivity to wavy-type imperfections. The modified nonlinear theory using the maximum stress failure criterion provides much closer correlation with experimental results than does the classical lamination theory.

6.4 Correlation Between Test Results and Analytical Predictions

The experimental results and the analytical predictions, using the nonlinear theory, further the understanding of compression failure of angle-ply laminates with imperfections. Even so, it was not possible to provide rigorous predictions of the failure strengths of the angle-ply laminates fabricated from IM7/8551-7a or AS4/3502 because exact types and levels of imperfections in the specimens that were tested were not known. It is possible through a parametric study, such as the present work, to obtain equivalent levels of imperfections in the laminates. The equivalent levels of imperfection could be used to predict the compressive strength of laminates with similar off-axis angles and similar material systems. The nonlinear theory as defined in the present work, then, could be considered a predictive tool for the analyst. It could use worst-case or statistical levels of imperfections in analysis.

It is the author's opinion that even though exacting comparisons between experimental results and predictions using the nonlinear theory could not be made, much was learned by comparing the results and the predictions. The modes and mechanisms of failure that were observed in the experimental results are very similar in character to the modes and mechanisms that caused failure at similar off-axis angles as predicted with the nonlinear analyses. The analyses indicated that the IM7/8551-7a material system is more sensitive to wavy imperfections than the AS4/3502 material system is. Without a great deal of experience to draw from, this conclusion probably could not be drawn from the experimental results alone, although the experimental results support the conclusion. The analyses were able to show which types of imperfections effect laminate compressive strength the most and the most likely location in the laminate for failure to begin, information that is difficult to determine experimentally without large numbers of tests.

6.5 Recommendations for Future Work

Though the analytical work and the experimental work provide significant insights into the compressive behavior of laminated composites, the limitations to the present work provide opportunity for future research. Suggestions for future experimental work include: Fabrication of laminates with clearly defined wavy layers such that rigorous comparisons between experimental results and the nonlinear theory can be made. Compression tests of IM7/8551-7a and AS4/3502 with the off-axis angles of 25°, 35°, 40°, 50°, 55°, and 65° should be conducted in order to fill in the gaps of the present experimental results. Compression tests using material systems with widely varying elastic properties and lamination sequences should be conducted in order to better understand the relative effects these parameters have on compression strength. Characterization of the effects that small layer variations have on compressive strength should be made.

Future modifications to the present nonlinear theory could include modifying the theory such that the thickness of a matrix-foundation varies according the relative imperfection amplitude in adjoining fiber-plates. The number of layers that can be analyzed in the program should be increased. Also, modifications that could improve the efficiency of the linear and nonlinear computer programs should be investigated.

Suggestions for future analysis, using the nonlinear theory, include: analyzing wavy laminates such as the first suggestion; i.e., exploring the capabilities of the theory with regards to laminates that do not have the same imperfection amplitude in every layer, and every layer is not imperfect. Also, the effects of combined compressive failure modes should be characterized. The relative effects that other values of imperfection amplitude, imperfection length, and imperfection ratio have on all compressive failure modes should also be investigated in detail.

Finally, another mechanism, which could be important experimentally and which is difficult to model analytically, might be considered. That is the mechanism of the specimen brooming, either on the ends or in the middle of the specimen, as seen in figure 2.25. In the range of $0° \leq \theta \leq 10°$ it is possible that brooming controls the compression response. The brooming would most likely be a function of material properties. In particular, considering brooming to be due to the fibers displacing sideways when fiber ends are borne down upon, fiber diameter and matrix stiffness and strength would most certainly control the load levels at which brooming occurs. Materials with smaller diameters and softer matrix properties could broom more easily than materials with larger diameter fibers and stiffer matrix properties. If brooming dominates, then compression strength could be independent of off-axis angle, as it is for IM7/8551-7a for $0° \leq \theta \leq 10°$. As a side note, the IM7 fibers are 5 microns[28] in diameter compared to 7 microns[28] for AS4, and the 8551-7a matrix properties are softer than 3502 matrix properties. The modeling of brooming would be difficult to add to the present analytical model. However, brooming could well control the observed compression strength and not including it could result in erroneously assuming failure is due to another mode.

REFERENCES

1 Dow, N.F., and Gruntfest, I.J., "Determination of Most-Needed Potentially Possible Improvements in Materials for Ballistic and Space Vehicles," General Electric Co., Philadelphia, P.A., A.F. Contract AF 04(647)-269, T.I.S. R60sd389, June 1960.

2 Rosen, B.W., "Mechanics of Composite Strengthening," *Fiber Composite Materials*, American Society for Metals, Metals Park OH, pp. 37-75, 1965.

3 Greszczuk, L.B., "Microbuckling of Unidirectional Composites," U.S. Air Force, Wright-Patterson AFB, OH, AFML-TR-71-231, January 1972.

4 Greszczuk, L.B., "Failure Mechanisms of Composites Subjected to Compressive Loading," U.S. Air Force, Wright-Patterson AFB, OH, AFML-TR-72-107, August 1972.

5 Evans, A.G., and Adler, W.F., "Kinking as a Mode of Structural Degradation in Carbon Fiber Composites," *Acta Metallurgica*, Vol. 26, pp. 725-738, May 1978.

6 Maewal, A., "Postbuckling Behavior of Periodically Laminated Medium in Compression," *International Journal of Solids and Structures*, Vol. 17, No. 3, pp. 335-344, March 1981.

7 Hahn, H.T. and Williams, J.G., "Compression Failure Mechanisms in Unidirectional Composites," NASA TM 85834, August 1984. Also offered in: *Composite Materials: Testing and Design (Seventh Conf.)*, ASTM STP 893, American Society for Testing and Materials, Philadelphia, PA, pp. 115-139, 1986.

8 Suarez, J.A., Whiteside, J.B., and Hadcock, R.N., "The Influence of Local Failure Modes in the Compressive Strength of Boron/Epoxy Composites," *Composite Materials: Testing and Design (Second Conference)*, ASTM STP 497, American Society for Testing and Materials, Philadelphia, PA, pp. 237-256, 1972.

9 Hawthorne, H.M., Teghtsoonian, E. "Axial Compression Fracture in Carbon Fibres," *Journal of Materials Science* Vol. 10, pp. 41-51, 1975.

10 Piggott, M.R., "A Theoretical Framework for the Compressive Properties of Aligned Fibre Composites," *Journal of Materials Science* Vol. 16, pp. 2837-2845, 1981.

11 Sinclair, J.H. and Chamis, C.C., "Compressive Behavior of Unidirectional Fibrous Composites," *Compression Testing of Homogeneous Materials and Composites*, ASTM STP 808, Richard Chait and Ralph Papirno, Eds., American Society for Testing and Materials, pp. 155-174, 1983.

12 Yeh, J.R. and Teply, J.L., "Compressive Response of Kevlar/Epoxy Composites," *Journal of Composite Materials*, Vol. 22, pp. 245-257, March 1988.

13 Gurdal, Z. and Haftka, R.T., "Compressive Failure Model for Anisotropic Plates with a Cutout," *AIAA Journal* Vol. 25, No. 11, pp. 1476-1481, December 1987.

14 Reifsnider, K.L. and Mirzadeh, F., "Compressive Strength and Mode of Failure of 8H Celion 3000/PMR15 Woven Composite Material," *Journal of Composites Technology & Research*, Vol. 10, No. 4, pp. 156-164, Winter 1988.

15 Gurdal, Z. and Starbuck, J.M., "Compressive Characterization of Unidirectional Composite Materials," *Analytical and Testing Methodologies for Design with Advanced Materials*, Eds., G.C. Sih, J.T. Pindera, and S.V. Hoa, 1988.

16 Odom, E.M. and Adams, D.F., "Failure Modes of Unidirectional Carbon/Epoxy Composite Compression Specimens," submitted for publication in *Composites*, 1990.

17 Highsmith, A.L., Davis, J.J. and Helms, K.L.E., "The Influence of Fiber Waviness on the Compressive Behavior of Continuous Fiber Composites," Aerospace Engineering Department, Texas A&M University and General Dynamics/FortWorth Division unpublished report, 1990.

18 Kumar, S. and Helminiak, T.E., "Compressive Strength of High Performance Fibers," *SAMPE Journal*, Vol. 26, No. 2, pp. 51-61, March/April 1990.

19 Schoeppner, G.A. and Sierakowski, R.L., "A Review of Compression Test Methods for Organic Matrix Composites," *Journal of Composites Technology & Research*, JCTRER, Vol. 12, No. 1, pp. 3-12, Spring 1990.

20 Adams, D.F., Odom, E. M., "Influence of Test Fixture Configuration on the Measured Compressive Strength of a Composite Material," *Journal of Composites Technology & Research*, JCTRER, Vol. 13, No. 1, pp. 36-40, Spring 1991.

21 Shuart, M. J., "Short-Wavelength Buckling and Shear Failures for Compression-loaded Composite Laminates," Ph.D. Dissertation, University of Delaware, Newark, December 1985; also available as NASA TM 87640, November 1985.

22 Shuart, M. J., "Failure of Compression-Loaded Multidirectional Composite Laminates," *AIAA Journal*, pp. 1274-1279, September 1989.

23 *1986 Annual Book of ASTM Standards*, ASTM D 3410-87 and ASTM D 695-85, Philadelphia PA, 1986

24 Shuart, M. J., "An Evaluation of the Sandwich Beam Compression Test Method for

Composites," *Test Methods and Design Allowables for Fibrous Composites*, ASTM STP 734, C.C. Chamis, Ed., American Society for Testing and Materials, pp.152-165, 1981.

25 Tsai, S.W. and Hahn, H.T., *Introduction to Composite Materials*, Technomic Publishing Company, Lancaster, PA, 1980

26 Jones, R.M., *Mechanics of Composite Materials*, Hemisphere Publishing Corporation, New York, NY, 1975

27 Rosen, B.W., "A Simple Procedure for Experimental Determination of the Longitudinal Shear Modulus of Unidirectional Composites," *Journal of Composite Materials*, Vol. 6, pp. 552-554, October 1972.

28 "Hercules Prepreg Tape Materials Characterization Data Package," Hercules Internal Report # H050-347, pp. 8,9, Feb. 1989.

29 Lentini, M. and Pereyra, V., "An Adaptive Finite Difference Solver for Nonlinear Two-Point Boundary Problems with Mild Boundary Layers," *SIAM Journal on Numerical Analysis*, Vol 14, No. 1, pp. 91-111, March 1977.

30 Coguill, S.L., Adams, D. F., "Mechanical Properties of Several Neat Polymer Matrix Materials and Unidirectional Carbon Fiber-Reinforced Composites," Composite Materials Research Group, Mechanical Engineering Department, University of Wyoming, Report UW-CMRG-R-88-114, December 1988.

31 "Magnamite AS4/3502 Graphite Prepreg Tape and Fabric Module," Hercules Aerospace Products Group, properties data report for marketing, p. 9, July 1985.

APPENDIX A: Sample Input and Output for THESLD - Linear Buckling Analysis

Sample input

```
LINEAR RUN FOR TEST SPECIMENS, BY L.PEEL JUNE 17,1991
CASE D  IM7/8551-7A [+-THETA/-+THETA]S, TEST PROPS
4,8,0.00573,.550,1.750,1.500,.100,0000
30.0,-30.0,-30.0,30.0,30.0,-30.0,-30.0,30.0
21.030E+06,1.283E+06,0.7067E+06,0.360,0.506E+06,0.1852E+06,0.366
0.138E+05
0,.0020,0.000,100
```

The input variables for THESLD are as follows:

line 1: comment line
line 2: comment line
line 3: ICASE, NL,TK,VF,XA,XB,XLAM,W0
line 4: THETA(1),THETA(2),....,THETA(NL)
line 5: FP(1),FP(2),FP(3),FP(4),XMP(1),XMP(2),XMP(3)
line 6: TAUMAX
line 7: IG,XINC,XINIT,NPT

The input variables are defined as
ICASE: Options for analysis as outline in section 4.1.2 where A=1, B=2, C=3, and D=4. (integer)
NL: Number of layers. (integer)
TK: Layer thickness. (floating point)
VF: Fiber volume fraction. (floating point)
XA, XB: Length (x direction) and width (y direction) of specimen. (floating point)
XLAM: Initial guess of half-wavelength for THESLD, actual half-wavelength for THESNS. (floating)
W0: Not used in THESLD, amplitude of initial imperfection. (floating point)
THETA(i): Ply orientation of the ith layer, degrees. (floating point)
FP(1-4): Fiber-plate lamina properties; E11, E22, G12, ν12. (floating point)
XMP(1-3): Matrix-foundation properties; E, G, ν. (floating point)
TAUMAX: Shear strength of composite material system. (floating point)
IG: Plotting flag; =0, no plotting; =1, results stored in file as columns of x and y data. (integer)
XINC: Increments for half-wavelength. (floating point)
XINIT: Initial value when plotting half-wavelength versus buckling strain. (floating point)
NPT: Number of points plotted. (integer)

Sample output

```
LINEAR RUN FOR TEST SPECIMENS, BY L. PEEL JUNE 17, 1991
CASE D  IM7/8551-7A [+-THETA/-+THETA]S, TEST PROPS

** INPUT DATA **
 NUMBER OF PLIES =  8
 PLY THICKNESS = 0.00573
 FIBER VOLUME FRACTION = 0.550
 PLATE LENGTH, A =  1.7500    PLATE WIDTH, B =  1.5000

 STACKING SEQUENCE:
   30.0  -30.0  -30.0   30.0   30.0  -30.0  -30.0   30.0

 CONSTITUENT MATERIAL PROPERTIES:

  FIBER-PLATE             MATRIX-FOUNDATION
   E11  = 0.2103E+08      E  = 0.5060E+06
   E22  = 0.1283E+07      G  = 0.1852E+06
   G12  = 0.7067E+06      NU = 0.3660E+00
   NU12 =  0.360

 CASE D:
  ALL LAYERS ANISOTROPIC
  DIFFERENT LAYERS
  PERFECT PLATE

 INPUT BUCKLING WAVELENGTH = 0.10000
 AMPLITUDE OF INITIAL IMPERFECTION = 0.00000
 MATRIX SHEAR STRENGTH, TAU-MAX =  0.1380E+05

** OUTPUT DATA **

 REDUCED STIFFNESSES:
  Q11 =  0.2120E+08    Q12 =  0.4656E+06
  Q22 =  0.1293E+07    Q66 =  0.7067E+06

   A-MATRIX:
    0.583E+06  0.182E+06  0.000E+00
    0.182E+06  0.126E+06  0.000E+00
    0.000E+00  0.000E+00  0.193E+06

 *AVERAGE LAMINATE MATERIAL PROPERTIES*

 LONGITUDINAL YOUNGS MODULUS =  0.6969187E+07
 TRANSVERSE YOUNGS MODULUS   =  0.1511780E+07
 SHEAR MODULUS               =  0.4219120E+07
 POISSONS RATIO, XY          =  1.443

   LAMINA STRESSES AT TAU-MAX
```

APPENDIX B: Sample Input and Output for THESNS - Nonlinear Analysis

Sample Input

```
VERIFICATION OF EXPERIMENTAL RESULTS W/ NONLINEAR PROGRAM 1/3/91  L. PEEL
IM7/8551-7A  [+-30/-+30]S  w0=.000573(.1t) lambda=.11460 (20t)
 4  8 0.00573 0.55 1.7540  1.505 0.11460
0.000573 0.000573 0.000573 0.000573 0.000573 0.000573 0.000573 0.000573
 30.0 -30.0 -30.0  30.0  30.0 -30.0 -30.0  30.0
21.030E+06  1.283E+06  0.707E+06 0.360  0.506E+06  0.185E+06 0.366
0.172E+05
0.02500  4
0.36 0.0032 0.38 0.0025 0.40 0.0027 0.42 0.0029
```

The input variables for THESNS are as follows:

line 1: comment line
line 2: comment line
line 3: ICASE NL TK VF XA XB XLAM
line 4: W0(1) W0(2) .... W0(NL)
line 5: THETA(1) THETA(2) .... THETA(NL)
line 6: FP(1) FP(2) FP(3) FP(4) XMP(1) XMP(2) XMP(3)
line 7: TAUMAX
line 8: U0ACR NLC
line 9: PCT(i) AMP(i), i=1, NLC

The input variables are defined as
ICASE: Options for analysis as outlined in section 4.1.2, for example, to use option D, use D=4. (integer)
NL: Number of layers. (integer)
TK: Layer thickness. (floating point)
VF: Fiber volume fraction. (floating point)
XA, XB: Length (x dir.) and width (y dir.) of specimen. (floating point)
XLAM: Initial guess of half-wavelength for THESLD, actual half-wavelength for THESNS. (floating)
W0(i): Amplitude of initial imperfection of each layer. (floating point)
THETA(i): Ply orientation of the ith layer, degrees. (floating point)
FP(1-4): Fiber-plate lamina properties; E11, E22, G12, ν12. (floating point)
XMP(1-3): Matrix-foundation properties; E, G, ν. (floating point)
TAUMAX: Shear strength of composite material system. (floating point)
U0ACR: Critical strain when short-wavelength buckling occurs, obtained from THESLD. (floating point)
NLC: Number of load steps to be solved. (integer)

```
  PLY =  1     THETA =  30.
   SIG, X  = -0.6433E+05     SIG, 1  = -0.7259E+05
   SIG, Y  =  0.0000E+00     SIG, 2  =  0.8261E+04
   TAU, XY = -0.2811E+05     TAU, 12 =  0.1380E+05

   APPLIED AXIAL STRAIN = -0.9230E-02
  *
  *
  *
  NUMBER OF ITERATIONS =  5

    *
    *
    *

   ** LAMINATE FAILURE **
      CRITICAL WAVELENGTH     =  0.13600D+00

  MODE =  1
  EIGENVALUE  = -0.52529D-01   AVERAGE LAMINATE STRESS = -0.36609D+06

  EIGENVECTOR (COMPLEX*16 FORM):
0.1000000D+01   I 0.0000000D+00        -0.2067975D-02   I 0.0000000D+00
  *
  *
  *
0.2108868D-04   I 0.0000000D+00        -0.3704000D-04   I 0.0000000D+00

 NO PLOTTING ATTEMPTED
```

PCT(i): Percentage of critical strain for ith load step. (floating point)
AMP(i): Initial guess at maximum w defection for ith load step.

**** Please note that input for THESNS is formatted, look at the READ statements in THESNS for proper format.

Selected numbers from sample output

Table B.1 Maximum Stresses and Strains from Sample Test Case

Load Step	Fiber Stress (ksi)	Shear Stress (ksi)	γ_{xz} Shear Strain
1	-110.9	-15.09	0.00722
2	-117.5	-15.95	0.00771
3	-124.2	-16.82	0.00821
4	-131.0	-17.68	0.00873

BIBLIOGRAPHIC DATA SHEET	**1. Report No.** VPI-E-91-19; CCMS-91-19	**2.**	**3. Recipient's Accession No.**

4. Title and Subtitle
Compression Failure of Angle-Ply Laminates

5. Report Date
September 1991

6.

7. Author(s)
Larry D. Peel, Michael W. Hyer, and Mark J. Shuart

8. Performing Organization Rep No.
VPI-E-91-19

9. Performing Organization Name and Address
Virginia Polytechnic Institute and State University
Department of Engineering Science and Mechanics
Blacksburg, VA 24061-0219

10. Project/Task/Work Unit No.

11. Contract/Grant No.
NAG-1-343 NASA-V
Tech Composites Prog.

12. Sponsoring Organization Name and Address
Aircraft Structures Branch
National Aeronautics and Space Administration
Langley Research Center
Hampton, VA 23665-5225

13. Type of Report & Period Covered
Interim Report 87
9/89-9/91

14.

15. Supplementary Notes
This report constitutes the thesis of the first author for an M.S. degree in Engineering Mechanics at Virgi
Polytechnic Institute and State University.

16. Abstract

The present work deals with modes and mechanisms of failure in compression of angle-ply laminates. Exp
imental results were obtained from 42 angle-ply IM7/8551-7a specimens with a lay-up of $[(\pm\theta)/(\mp\theta)]_{6S}$ where
the off-axis angle, ranged from 0° to 90°. The results showed four failure modes, these modes being a functior
off-axis angle. Failure modes include fiber compression, inplane transverse tension, inplane shear, and inpla
transverse compression. Excessive interlaminar shear strain was also considered as an important mode of failu
At low off-axis angles, experimentally observed values were considerably lower than published strengths. It v
determined that laminate imperfections in the form of layer waviness could be a major factor in reducing cc
pression strength. Previously developed linear buckling and geometrically nonlinear theories were used, v
modifications and enhancements, to examine the influence of layer waviness on compression response. The wa
layer is described by a wave amplitude and a wave length. Linear elastic stress-strain response is assumed. 1
geometrically nonlinear theory, in conjunction with the maximum stress failure criterion, was used to pre
compression failure loads and failure modes for the angle-ply laminates. A range of wave lengths and amplitu
were used. It was found that for $0^\circ \leq \theta \leq 15^\circ$ failure was most likely due to fiber compression.
$15^\circ < \theta \leq 35^\circ$ failure was most likely due to inplane transverse tension. For $35^\circ < \theta \leq 70^\circ$ failure was m
likely due to inplane transverse compression. The fiber compression and transverse tension failure modes
pended more heavily on wave length than on wave amplitude. Thus using a single parameter, such as a ratic
wave amplitude to wave length, to describe waviness in a laminate would be inaccurate. Throughout, results
AS4/3502, studied previously, are included for comparison. At low off-axis angles, the AS4/3502 material syst
was found to be less sensitive to layer waviness than IM7/8551-7a. Analytical predictions were also obtained
laminates with waviness in only some of the layers. For this type of waviness, laminate compressive stren
could also be considered a function of which layers in the laminate were wavy, and where those wavy layers we
Overall, the geometrically non-linear model correlates well with experimental results.

17. Key Words and Document Analysis. 17a. Descriptors
compression testing, compression failure, compressive modulus, layer waviness, nonlinear laminate model, buckling, failure criterion

17b. Identifiers/Open-Ended Terms

17c. COSATI Field/Group

18. Availability Statement	**19. Security Class (This Report)** UNCLASSIFIED	**21. No. of Pages** 174
	20. Security Class (This Page UNCLASSIFIED	**22. Price**